STUDY OF HOTSPOT COOLING FOR INTEGRATED CIRCUITS USING ELECTROWETTING ON

DIELECTRIC DIGITAL MICROFLUIDIC SYSTEM

by

GOVINDRAJ SHREYAS BINDIGANAVALE

Presented to the Faculty of the Graduate School of

The University of Texas at Arlington in Partial Fulfillment

of the Requirements

for the Degree of

DOCTOR OF PHILOSOPHY

THE UNIVERSITY OF TEXAS AT ARLINGTON

May 2015

ACKNOWLEDGEMENTS

April 9, 2015

ABSTRACT

STUDY OF HOTSPOT COOLING FOR INTEGRATED CIRCUITS USING ELECTROWETTING ON

DIELECTRIC DIGITAL MICROFLUIDIC SYSTEM

Govindraj Shreyas Bindiganavale, PhD

The University of Texas at Arlington, 2015

Supervising Professor: Hyejin Moon

Thermal management in electronics is an ever-growing challenge which needs constant innovations to regulate hotspots in integrated circuits for safe operation within its Thermal Design Power (TDP) envelope. As the number of transistors increase due to advancements in photolithography to enable die shrink, portable electronics are on the rise and so is the demand for microscale cooling systems because conventional cooling components like heat sinks, heat pipes and fans are not capable of meeting design requirements for cooling solutions. In addition to the benefits enjoyed by microscale cooling systems like compact and lightweight design along with simple operation, electrowetting on dielectric (EWOD) based digital microfluidic (DMF) hotspot cooling promises an innovative and novel cooling based on valveless and pumpless motion of coolant droplets directly on hotspots. Along with reduction in thermal resistance, this technology is also useful for site specific cooling by moving droplets to multiple hotspots on chip.

In this research, Indium Tin Oxide (ITO), a transparent conducting material, was patterned on glass substrates to emulate hotspots and also provide the electric field for EWOD pumping of droplets. Two cooling systems were designed, fabricated and tested for demonstrating temperature drop, namely Ionic Liquids (ILs) and De-Ionized (DI) water, using Liquid Crystals and ITO Resistance Temperature Detectors (RTDs) as the temperature sensing techniques. ILs were initially used as coolants to suppress evaporation but turned out to have poor cooling capability than DI water from LCT results. Apart from conduction and

convection heat transfer from the hotspot to the droplet, phase-change was also responsible in achieving cooling for DI water.

To facilitate detailed study of hotspot cooling, an innovative approach to regulate hotspot temperature was demonstrated by creating a hydrophilic spot (H-spot) on the heater which retains a small droplet while the main coolant droplet passes over the hotspot. High-speed video was taken and synchronized with RTD data to identify different phases of droplet motion and observations were made to explain the heat transfer modes in each phase of motion. Transient heat transfer simulations in COMSOL Multiphysics including emulation of phase-change effects were performed for varying thermal diffusivity values of the droplet to understand its effect on the heater temperature. Finally, an analytical model was proposed based on literature which related droplet evaporation on the H-spot to the overall heat transfer coefficient. The evaporation rate was also calculated experimentally and compared with the ideal values used in the COMSOL simulations which resulted in the evaporation rates being in good agreement with each other.

TABLE OF CONTENTS

LIST OF ILLUSTRATIONS

LIST OF TABLES

CHAPTER 1

INTRODUCTION

1.1 Electronics Cooling

In accordance to Moore's law, with an increase in heat generation for decreasing real estate on a die, thermal management in electronics has become more challenging [1]. Conventional cooling systems like heat sinks [2], heat pipes [3], [4], fans and vents assemblies were used in majority of the electronic devices until two important factors, namely size/weight & thermal resistance started testing its mettle. In spite of advancements in these systems [5], their sheer size and weight in comparison with available space for thermal management and high thermal resistance due to the unavailability of direct cooling of hotspots in 3D Integrated Circuits (ICs) ignited research in micro scale cooling systems.

1.2 Hotspot Cooling in ICs

ICs typically have a non-uniform spatial power distribution (hotspots). At hotspots, large temperature gradients are expected and may cause unacceptably high mechanical stress resulting in component failure. To tackle hotspot cooling, a number of novel techniques have been proposed using microfluidic platforms which reduces size & weight complexities and provides a direct access to the coolant to maintain hotspot temperatures thereby minimizing thermal resistance. Researchers in the field of electronics cooling have developed and demonstrated cooling systems which are smaller, lighter and more efficient for hotspot cooling on chip than the traditional heat pipe/heat sink mechanism. Such technologies include, but are not limited to, Synthetic Air Microjet cooling [6], Micro Capillary Pumped Loop [7], Silicon Microchannel Cooler [8], etc. Thermoelectric coolers [9] have also been used as means of demonstrating hotspot cooling. Most of these innovative cooling solutions require far less operating power, fewer or no mechanical parts, and smaller components. These cooling devices are governed by basic principles of heat transfer using phase change, conduction and convection. Jiang et al. [10] presented a closed-loop two-phase cooling system for electronic circuits using an integrated electroosmotic pumping technique to transfer liquids to and from a heat exchanger. Heffington et al. [11] have developed a cooling module based

on piezoelectric generation of droplets, where secondary droplets are formed from a primary droplet and then impinged on the hot surface upon which they immediately vaporized. Many other researchers have reported microfluidic cooling platforms, however, most of the platforms use microchannel based flow [12], [13] which is less efficient for cooling unevenly distributed power.

To meet the increasing demand of efficient cooling performance in small scale, this research presents an innovative cooling system capable of mitigating the above problems using digital microfluidics (DMF) microscale liquid cooling concept which works on the principle of electrowetting on dielectric (EWOD).

1.3 Electrowetting on Dielectric (EWOD) based Digital Microfluidics (DMF)

With reference to the way in which the cooling medium is handled for cooling, Electrowetting on dielectric (EWOD) [14] is one concept which has been recently developed and holds promising capabilities amongst all the above technologies for the future of electronics cooling. Electrowetting involves changing the wetting ability of a drop by using electric field, especially on hydrophobic surfaces, hence making droplet manipulation easy. The reason we use hydrophobic surfaces as the platform for EWOD is obvious due to the fact that the wetting enhancement by using electric field is unidirectional, i.e., we can only decrease the surface tension (or improve the wetting ability) by the application of electric field and not vice versa.

(a)   (b)
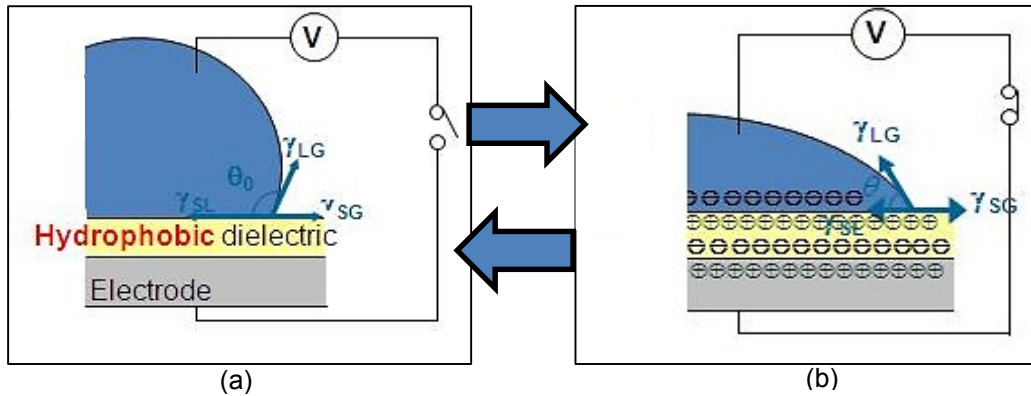
Figure 1-1 EWOD effect on a hydrophobic surface with droplet before (a), after (b) applying electric field.

Referring to Figure 1-1 (a), a droplet (electrolyte) placed on a hydrophobic surface takes the shape as shown. γ_{LG}, γ_{SL} and γ_{SG} is the surface tension between the liquid-gas, solid-liquid and solid-gas interface

respectively. The angle between γ_{LG} and γ_{SL} is defined as the contact angle, θ_0, and is the parameter of focus in this section. The EWOD phenomenon occurs when an electric potential is applied as shown in Figure 1-1 (b). Due to this electric field, the charges within the liquid drop and the solid dielectric are re-distributed into opposite charges, thus modifying the surface energy at the solid, liquid and gas interface. This develops repulsive forces between the like charges within the drop and decreases the net surface tension by reducing work done in expanding the surface area of contact. This in turn, decreases the contact angle, θ_0. Another observation to make is that due to the re-distribution of charges between the interfaces, an electrostatic force between opposite charges facilitates the drop to move radially outward. This is the driving force to facilitate easy manipulation of the drop as explained in section 1.4. The theoretical analysis of electrowetting is discussed in detail in various papers [15], [16], [17].

The basic theory is governed by the Lipmann equation [18] which gives us the relation between the surface tension γ and the voltage V applied

$$\gamma = \gamma_o - \frac{1}{2}cV^2 \tag{1-1}$$

where γ_o is the surface tension at the solid and liquid interface when the circuit is open i.e., when no charge is present, and c is the capacitance of the dielectric layer. The above equation can be expressed in terms of the contact angle, θ_0, by using the Young's equation

$$\gamma_{SL} = \gamma_{SG} - \gamma_{LG} \cos \theta \tag{1-2}$$

then we have

$$\cos \theta = \cos \theta_o + \frac{1}{\gamma_{LG}} \frac{1}{2}cV^2 \tag{1-3}$$

where θ_o is the contact angle when no voltage is applied. This is the basic principle which has been used to transport a drop or coolant from one spot to the other on the microfluidic device for hotspot cooling.

1.4 Microfluidic Hotspot Cooling Device using EWOD Principle

There have been many successful attempts by various research groups to build and operate microfluidic devices for electronic hotspot cooling. Pamula et al [19], Oprins et al [20], Baird and Mohseni [21] were some of the researchers who have worked on these devices which involved moving the coolant drops using EWOD principle across artificially created hotspots on patterned circuits. Figure 1-2 shows the phenomena of droplet transportation using EWOD with the drop sandwiched between two devices with the patterned circuits (shaded dark) while the top circuit controlling the motion of the drop and the bottom serving as the hotspot with the help of a small heater.
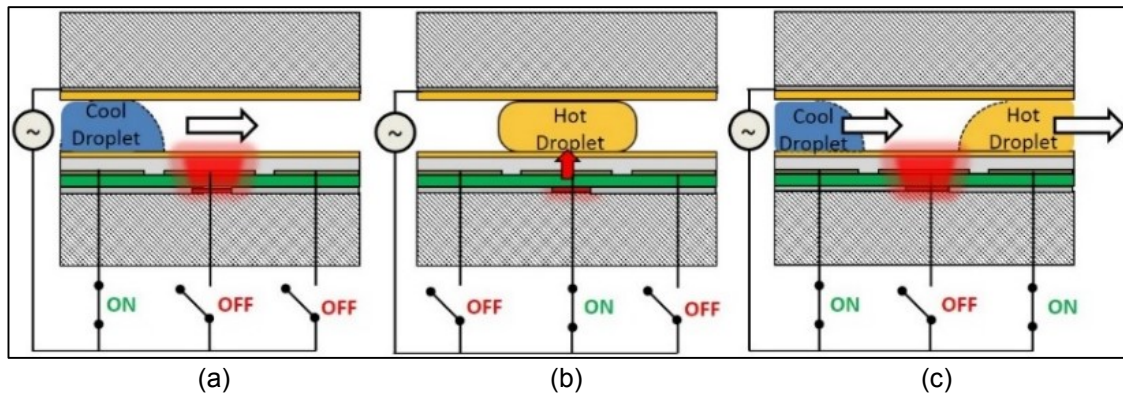
Figure 1-2 Concept of hotspot cooling by EWOD ((a) through (c)) showing heat removal by the cool drop.

Figure 1-2 (a) through 1-2 (c) shows a cool drop moving over the hotspot with the help of EWOD, the heat being transferred to the drop through heat transfer, the hot drop moved away from the hotspot leaving behind a cooled spot. This process can be repeated by using multiple drops, one behind the other, to achieve continuous cooling effect.

CHAPTER 2

PROOF-OF-CONCEPT COOLING SYSTEM[1]

In order to demonstrate EWOD DMF hotspot cooling, a proof-of-concept cooling system using Liquid Crystal Thermography (LCT) was fabricated and tested. Indium Tin Oxide (ITO) was used as the material of choice for the EWOD and heater which was fabricated and setup using clean-room semiconductor fabrication methods. Ionic liquids (ILs) [22], [23] and De-Ionized (DI) water coolants were used to demonstrate hotspot cooling using LCT.

2.1 Introduction to LCT

As explained in the device setup in section 2.2, it was difficult to incorporate a thermocouple directly in the path of the liquid drop to measure the temperature change on the hotspot due to the space and design limitations. Hence, a need arose to visually determine the temperature change on the hotspot by the use of Liquid Crystals (LC's) sensitive to temperature, also known as Thermochromic Liquid Crystals [24] (TLC's). In LCT, a color image in RGB color space was converted to HSL (Hue/Saturation/Lighting) color space and the hue image was extracted. This hue image contained only the information pertaining to the true color of the pixel and not the saturation or the lighting. This helped us to better visualize a LC image and demarcate the color bands to identify the temperature on the hotspot. When TLC's are subjected to temperature change, they emit colors within the visible spectrum. They have twisted molecular structures and are generally used in three forms, one in the unsealed form, second in the microencapsulated form and thirdly, in the form of printed sheets. TLC's in unsealed form are more susceptible to degradation as they can be easily attacked by dust, atmospheric gases and grease. They generally have a lifetime of few hours to days and are mainly used for applications involving shear stress analysis and are not suitable for temperature measurements. Sealed TLC's are microencapsulated in polymers which protect them from the environment. They are sealed in tiny spheres of microencapsulation and are applied on surfaces by brush

---

[1] This chapter is a direct excerpt from the Master's thesis written by the same author cited in [23].

or spray paints. For the hotspot cooling device, this type of TLC was painted behind the heater of the bottom chip for hotspot cooling as temperature indicators.

2.2 LCT Experimental Setup
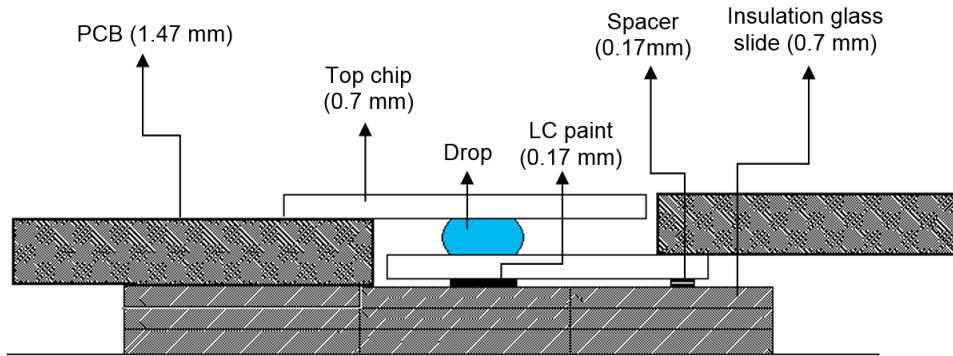
Figure 2-1 Cross-section view of the proof-of-concept cooling device with LC paint below the bottom chip.

The microfluidic device for hotspot cooling used EWOD to pump coolant drops across hotspot created on the device. Figure 2-1 shows the cross section view of the device which consisted of two glass devices or chips with patterned circuits on each of them. The circuits on the glass chips were connected to a copper clad Printed Circuit Boards (PCB) with the help of an electrically conductive adhesive transfer tape (3M, www.3m.com). The PCB's were further connected to Data Acquisition (DAQ) hardware, which was in turn connected to a computer which controlled the EWOD motion automatically, with the help of LabVIEW software. The top chip consisted of the EWOD circuits required to move the drop while the bottom chip had the ground and the heater electrode, between which the drop was sandwiched. In order to measure the temperature of the hot spot, it was difficult to incorporate a thermocouple, given the space and dimensions constraints. Therefore, TLC paint was used to visualize the temperature change by interpreting the change in color to temperature. When the LC's were painted below the hotspot, different color bands were observed and the temperature could be determined using LCT. In the above setup, the heater was between the drop and the LC paint.
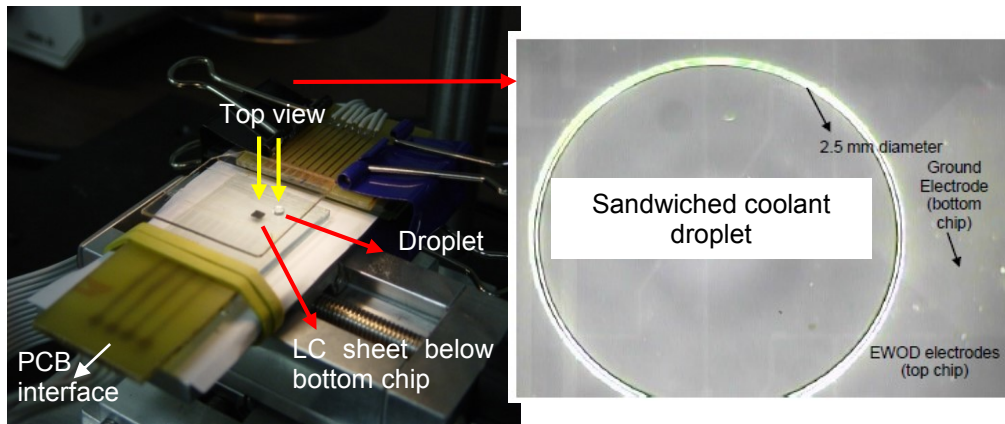
Figure 2-2 Figure showing the isometric view of the hotspot cooling device.

In Figure 2-2, a setup of the device has been shown. The top and bottom chips were manufactured on standard 1016 mm (4 inch) diameter and 0.7 mm thick Indium Tin Oxide (ITO) coated glass wafers (TechGophers Corp., CA). ITO is a new material used in the field of electronics which is transparent in appearance and is sometimes used in place of standard copper conductors, especially for applications which require better visibility of devices placed under each other. In the present case, ITO not only served as a good electrical conductor but enabled us to see the chips placed below. The ITO circuits were fabricated using standard microfabrication techniques as explained in section 2.2.1.
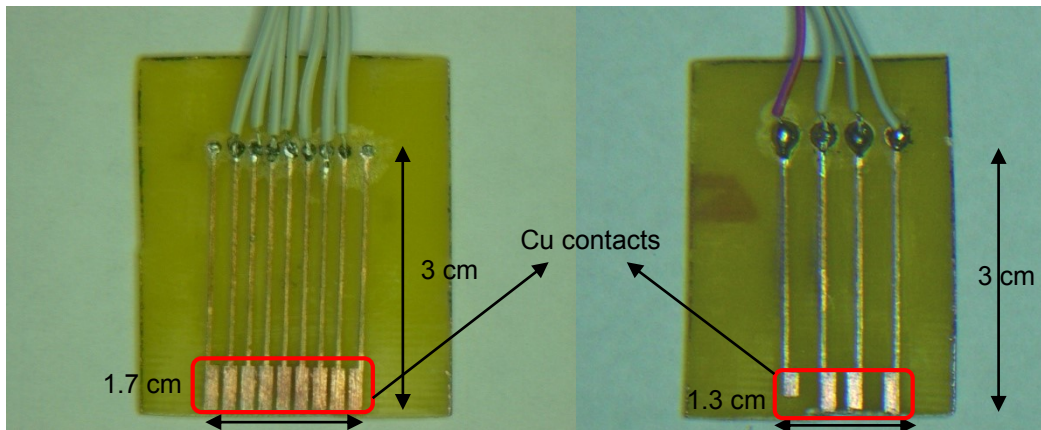
Figure 2-3 Top chip PCB showing the etched copper electrodes.

The PCB interfaced the connections from the DAQ system to the top and bottom chips. Unlike copper, it is very difficult to solder any conducting material onto ITO terminals directly. Therefore, conductive

adhesive tapes were used to attach the ITO terminals on the chip to the copper terminals on the PCB. As shown in Figure 2-3, the circuit on the PCB was fabricated by printing the design on a photographic paper and then pressing it firmly on the copper clad PCB while applying heat. The paper was slowly peeled off from the PCB with the help of soap solution to reveal the mask of the design, which was then dipped in a copper etchant (Ferric Chloride solution, MG Chemicals, Canada) to etch the area surrounding the mask, leaving behind the desired pattern. In the next section, a detailed note on the chip circuit and PCB circuit, right from design to development, is given. It has to be noted, that throughout the development of the device for hotspot cooling, many designs were considered, fabricated and used on the ITO chips and changes were made constantly to improve the performance of the device. The next section deals with the final design which was found to give the best performance in terms of the speed of the drop and in turn, the heat removal from the hotspot.
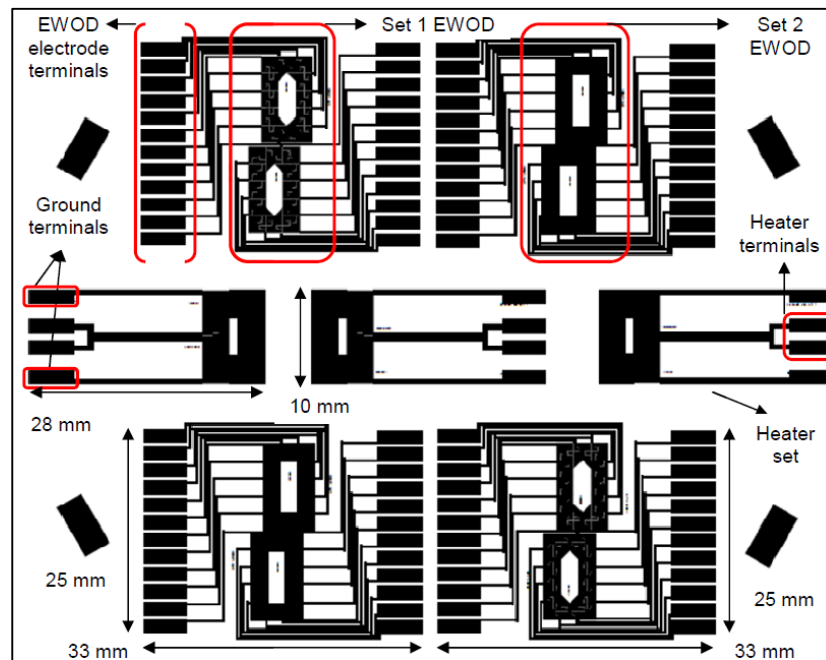
Figure 2-4 Mask showing two EWOD and one heater set used in photo lithography for device fabrication.

The circuit designs that were used for the hotspot cooling device were created using Tanner EDA's (www.tanner.com) L-Edit software. The finished circuit designs were exported to GDS (Graphic Data

System) file type and were then converted to PostScript (PS) format using LinkCAD software. The PostScript format allows us to view the final design of the circuit which is similar to PDF format. The PS file was sent to a mask printing company, CAD/Art Services Inc., OR, for use in photo lithography. Photo lithography is a microfabrication process which is explained in detail in section that follows. The mask which was printed and used for patterning the circuits on the top and bottom chips is shown in Figure 2-4. This mask shows three sets of patterns, two sets for the EWOD chip and one set for the bottom or heater chip. Another copy of the EWOD chip designs were printed on the other side of the heater designs so that maximum real estate on one ITO glass wafer was used. For efficient fabrication, each EWOD design had two chips within it, enabling us to use both sides of the chip for two different liquids.
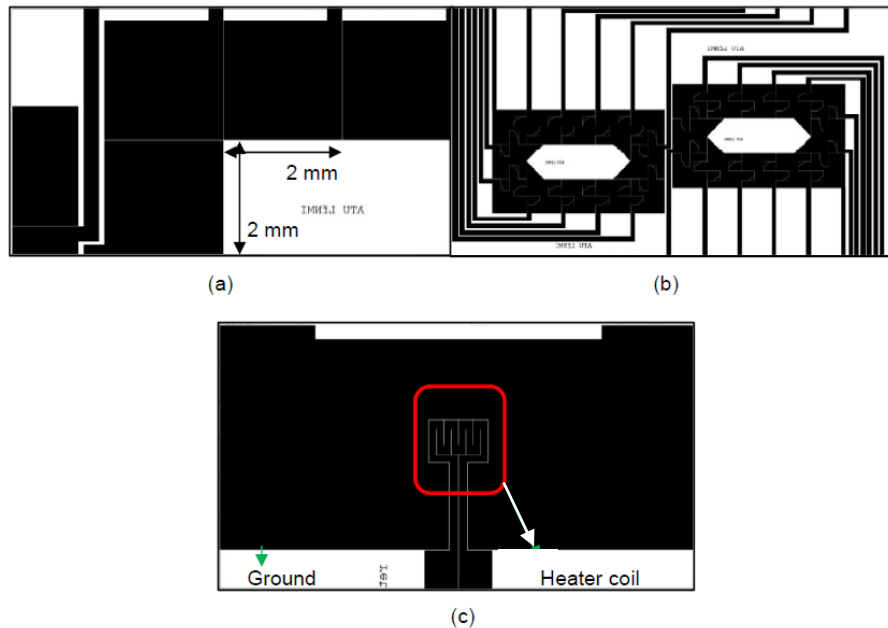
Figure 2-5 Set 1 (a) and set 2 (b) EWOD designs with heater (c) set.

Figure 2-5 (a) through Figure 2-5 (c) shows the above mask with the set 1 EWOD chip design, set 2 EWOD chip design with inter-digitating finger like electrodes and the seven-coiled heater design. These EWOD chip designs were built after multiple changes of the design parameters. These changes included the electrode pad size, spacing between the top and bottom chips and the drop size. Drop properties like

9

heat removing capacity, viscosity and the electrowetting characteristics also fuelled the need to change designs. As shown in Figure 2-5 (a), the size of the EWOD pad was set at 2 mm with a gap of 0.01 mm between the pads, which was found to be ideal for the size of the hot spot generated by the heater. In Figure 2-5 (b), the finger like structures protruding into adjacent pads was meant to enhance the motion of highly viscous liquids like IL1 and IL2. As the viscosities of IL1 and IL2 are high, it was observed that the drop lost contact with the next electrode pad and thus, the motion was broken. To counter this problem, these protrusions were made so that the drop always remains in contact with the next electrode. Smooth motion of the drop was also observed when the gap between the top and bottom devices was set at 0.6 mm. The seven-coiled, 1.5 KΩ heater was designed in such a way that it lied directly in the path of drop. The area surrounding the heater, the ground electrode, was not connected to the heater electrode and maintained a constant gap of 0.01 mm. This meant there were two separate connections on the bottom chip, one which operated the heater and the other providing the grounding for the EWOD circuit.

2.2.1 Device Fabrication

The fabrication steps involved basic clean room MEMS fabrication processes like spin casting, photo lithography, developing, etching and baking. Prior to any fabrication process, a detailed cleaning process was done which involved washing the wafer with Acetone, Methanol and then rinsing it with de-ionized water. The wafer was baked at 150°C on a hotplate (Isotemp, Fisher Scientific) to dehydrate it completely. As the name suggests, spin casting involves depositing thin films of uniform thickness on substrates by spinning them. Thin film deposition included two materials, Hexamethyldisilazane (HMDS), a colorless solution used to enhance the adhesion of photoresist (PR) to the wafer, and the PR itself, a material sensitive to light. Referring to Figure 2-6, HMDS was poured and spun on a vacuum chuck at a custom recipe. The recipe involved spinning the wafer to 500 RPM for the first 5 seconds and then ramping it up to a speed of 4000 RPM at a rate of 900 RPM/sec. The wafer was spun for the next 30 seconds at this constant speed. After depositing HMDS, the wafer was baked at 150°C for 1.5 minute. The same spinning

recipe was used for depositing PR on the HMDS layer, after which, the wafer was baked again at 115°C for a minute. After spin casting process, photo lithography was done.
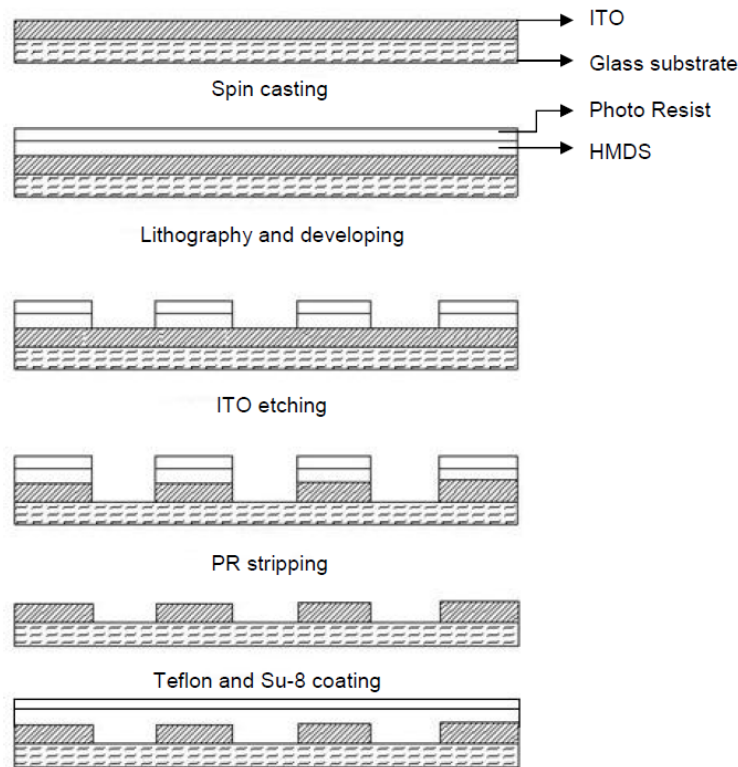
Figure 2-6 Steps showing the fabrication process.

Photo lithography is used to selectively remove parts of the PR. This is possible with the help of a lithography mask. Referring back to Figure 2-4, the mask contained a dark pattern of the circuit to be printed on the wafer. When the wafer was subjected to high energy ultraviolet (UV) rays, the light passed through the blank portions on the mask and did not pass through the printed portions. This changed the chemical properties of the PR (sensitive to light) in only those regions on the wafer which were subjected to UV rays. After lithography, the wafer was baked at 115°C for a minute to harden the PR untouched by light. The next step involved developing the processed PR. A Developer solution (MF-391, ROHM and HAAS) was used to dissolve and remove parts of the PR which was exposed to UV rays, leaving behind the unexposed PR which formed the pattern and exposing the ITO layer. In order to make the unexposed regions on the wafer

impervious to the effects of etching, baking was done to harden them. Post developing and baking, etching was done to remove the ITO layer unprotected by the PR. The etchant used was a mixture of HNO₃, HCl and DI Water in the ratio of 1:8:15 respectively. The duration of etching was 5 minutes. To catalyze the etching, a constant temperature of 55°C was provided to the etching solution. Finally, a PR stripper solution was used to remove the baked PR to reveal the chip with the ITO patterned circuitry.
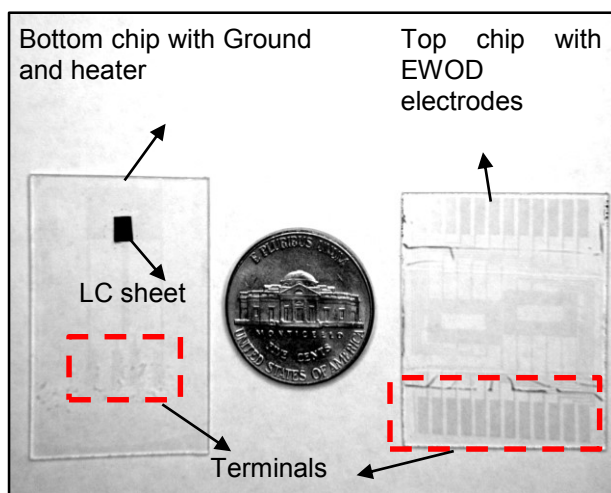
Figure 2-7 ITO patterned bottom and top chips compared to a 5 cent coin for scale.

The wafer with the ITO patterns was diced into smaller chips along the sets of EWOD and heater designs. Figure 2-7 shows the diced chips with the ITO circuits. The diced chips were then ready for the next step in fabrication process – to deposit the dielectric layer. SU-8 20, a photoresist used for high aspect ratio lithography, was used as the dielectric layer. In order to spin cast a 5μ thickness SU-8 layer, the wafer was initially ramped up to 500 RPM at 100 RPM rate and spun for the next 5 seconds. Next, it was spun to a speed of 3000 RPM at 300 RPM ramp rate for 30 seconds. After spinning the SU-8 onto the wafer, it was baked on the hotplate at 65°C for one minute and then at 95°C for 3 minutes. The wafer underwent lithography, with the entire surface exposed to UV rays which polymerized the SU-8 layer.

The wafer was again heated at 65°C and 95°C each for one minute and then at 150°C for 15 minutes, concluding the SU-8 deposition process. In order to achieve hydrophobic surfaces on the active sides of the top and bottom chips, amorphous flouropolymer solution (Teflon) was spin casted. The solution

was prepared by mixing amorphous flouropolymer crystals (DuPont) in a per-flouro compound FC-75 solvent (Acros Organics) with a 2.5 w/v ratio. The recipe involved ramp up spin speed of 500 RPM at 100 RPM rate for 5 seconds and then 1000 RPM at 100 RPM spin rate for 30 seconds. This process was performed twice to yield a thicker Teflon layer. The chips were baked in an oven (Thermolyne Inc.) at 115°C, 150°C and 180°C for 10, 15 and 30 minutes respectively. Once the final device with the top and bottom chips was fabricated, it was ready for the hotspot cooling experiments.

Figure 2-8 Flowchart showing the hardware and software components of the entire setup. Dark arrows represent digital and electrical signals while dotted arrows represent visual data.

Figure 2-9 Custom built switch board showing the connector sockets and switches.

2.2.2 Experimental Procedure

The setup for hotspot cooling device comprised various hardware and software components which initiated, controlled and recorded the motion of the drop. Figure 2-8 shows a flow chart of the various chart, the waveform generator and the DC sourcemeter were directly controlled by the user. This was a onetime operation to set the AC voltage and DC current for the hotspot cooling device. The voltage and the hardware At the top of the flow current outputs were connected to a custom built switch board with switches, an input and an output connector socket. The input connector socket was connected to a DAQ system which comprised a digital I/O device (NI USB-6509), a connector block (NI SCB 100) and a cable (NI SH100-100-F) connecting the two. The connector block was connected to the input connector socket on the switch board with spare 40 pin IDE/ATA hard drive cables. The connections from the socket, AC and DC source were wired to the input side of the corresponding switch. As shown in Figure 2-9, the switch board with the input and output connector sockets along with the EWOD and the heater switches is shown. Seven AC

14

EWOD switches corresponded to seven distinct EWOD pads on the top chip and two DC heater switches corresponded to the heater terminals on the bottom chip of the hotspot cooling device. Separate AC voltage and DC current lines were taken from the output side of the corresponding switch and wired to the common output connector socket. A 50 pin IDE/ATA cable connects the output connector socket to the hotspot cooling device. Directly above and normal to the device, a ring light, connected to a halogen lamp source (StockerYale IMAGELITE Model 20), a lens arrangement (Edmund Optics, VZM 1000 Video Lens) and a color CCD camera (HITACHI, KP-D20BU) are fixed with the help of a stand and stage arrangement. In order to capture the images off the CCD camera, a PCI interface frame grabber card (NI PCI-1411) was installed in the PC. The camera and the frame grabber were connected by an S-Video cable. The data from the hard drive was sent to another PC with MATLAB installed for LCT. In order to control the DAQ system, it was connected from the PC to the digital I/O device by a USB cable. This completes the hardware setup.
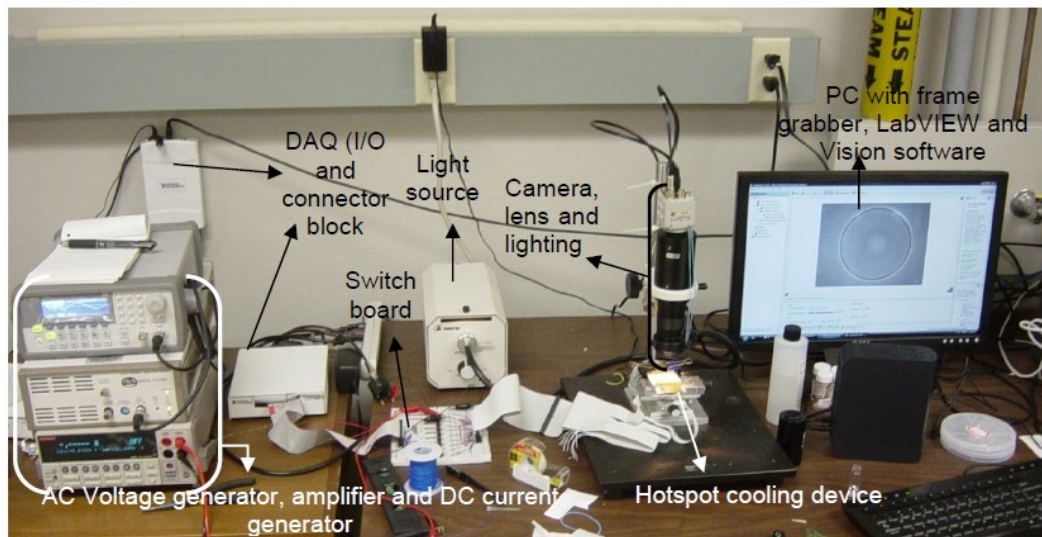
Figure 2-10 Experimental setup of the LCT system.

Figure 2-10, shows an overview of the setup used for the hotspot cooling device. To the left of the figure, an AC waveform generator (Agilent, Model 33220A), voltage amplifier (Trek, Model PZD 350) and a DC sourcemeter (Keithley 2400 series) were arranged in a rack. For the EWOD circuit, the AC voltage (in mV) from the waveform generator is sent to the amplifier, from which the voltage range is amplified to 100

times (V). The terminals are connected to the switch board with the help of clip-on wires. For the heater circuit, two wires connect the DC sourcemeter to the switch board. A single IDE cable connects the output connector socket to the top and bottom chip on the hotspot cooling device, which is fixed on a stage with XY movement (Velmex, Inc.). Finally, the CCD camera is connected to the frame grabber card installed in the PC. The softwares used in the experiments mainly included LabVIEW 8.5 to control the experiment and gather visual data for LCT simultaneously. LabVIEW used NI-DAQmx 8.7.1 drivers for controlling the DAQ system in conjunction with NI-IMAQ 4.1 drivers for initializing the frame grabber card and capturing data (images and videos) via CCD camera. For image processing functions, NI-IMAQ used NI Vision Assistant software and MATLAB was used to perform LCT.

To start with, the AC and the DC machines were switched on and the voltage and current values were set to the desired values respectively. In case of the AC generator, the voltage was set at 1.5 V (RMS) which was amplified to 150 V (RMS) in the amplifier. Similarly, the DC sourcemeter current was set to a constant 0.011 A. With a heater resistance of 1.5 KΩ, the voltage in the heater circuit was 16.5 V. The PC was switched on and LabVIEW software was started. Two different programs, one for DAQ control and the other for image acquisition, was opened. The light source for the device was switched on and set at the correct intensity.

Once the above operations were done, the next step was to sandwich the drop between the top and bottom chips. Using a dispenser (Eppendorf AG), a certain volume of the fluid was taken into the dispenser tip and dispensed on the bottom chip in such a way that the drop lied in the path of the EWOD ground electrode. The drop was then sandwiched by the top chip and its size was kept to a constant diameter of 2.5 mm, as shown in Figure 2-11. If the size fell long or short of 2.5 mm, the volume of the drop was adjusted using the dispenser. Care was taken to align the top and bottom devices by observing the live image on the PC monitor.
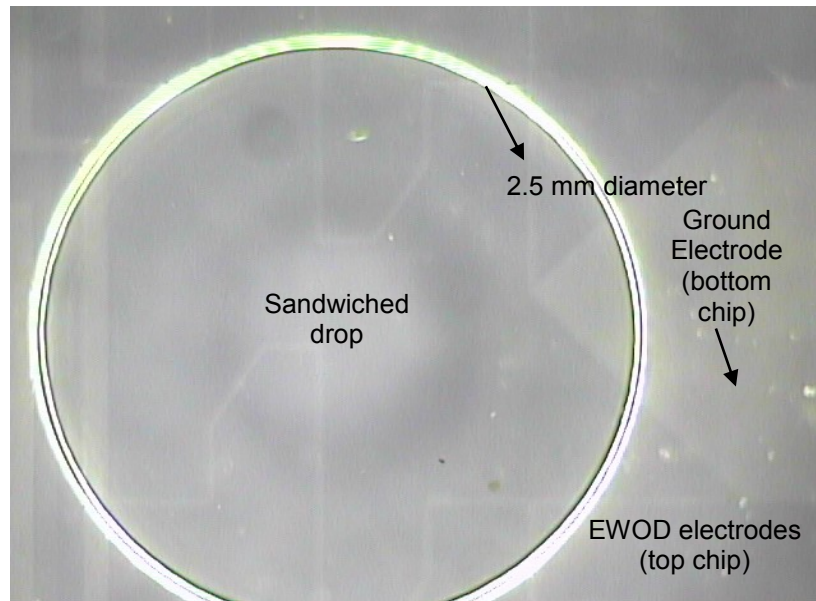
Figure 2-11 An RTIL1 drop sandwiched between the top and bottom chip, ready for the experiment. The ground electrode is slightly visible as it is out of focus.

Once the drop was dispensed and sandwiched properly in the device, all attention was turned to the PC controlling the DAQ and the visual data acquisition. As mentioned before, two different VI's were used in LabVIEW, one to control the EWOD motion and the other to acquire the visuals. The VI which controlled the EWOD consisted of a switch on the front panel, which when turned on, sent signals to the digital I/O device through USB. The I/O device converted the signals into analog voltage signals not exceeding 5 V and sent it to the connector block. The connector block had terminals which could be wired up to the switch board. In this case, only seven such terminals were needed to control seven individual EWOD electrode pads on the top chip and two electrode pads on the heater switch, totaling to nine terminal connections from the connector block. Figure 2-12 shows the channels assigned in LabVIEW corresponding to the ports in the digital I/O hardware connected to the connector block. Similarly, every
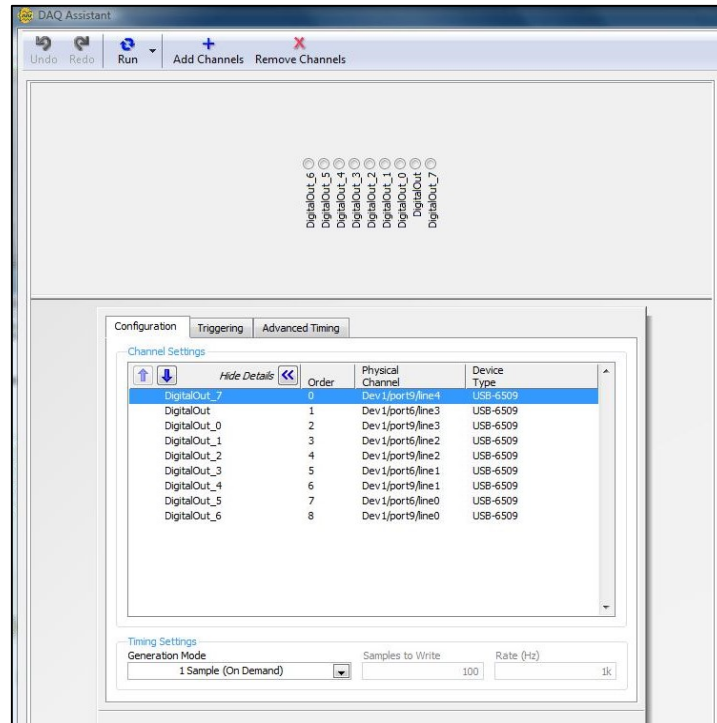
Figure 2-12 DAQ Assistant interface in LabVIEW showing nine ports assigned to the digital I/O device.

terminal in the connector block was wired to the corresponding switch on the switch board. Hence, by turning on the switch in the front panel, the signals were switched from one electrode to the next in the DAQ hardware and subsequently, on the switch board, hence moving the drop with the application of the external AC voltage. The EWOD VI also had a switching time input which controlled the time gap between the switching of two consecutive electrodes. Considering the viscosities of the different liquid drops used, and after many trials, the switching time was set at 5 second.

The final step in the testing flowchart was to capture the RGB data and convert it to HSL space. LabVIEW was used to do this and eventually the LCT image processing was performed in MATLAB. A more comprehensive procedure can be found in [23].

2.3 Hotspot cooling with ILs and DI water using LCs - Results

The motive of the experiments was to use Ionic Liquid and validate its choice as a coolant to take advantage of its low vapor pressure property. The drops were moved over the hotspot and kept static for 5

seconds after which they were moved onto the next EWOD electrode pad. From LCT, the temperature change was estimated and was compared to a numerically simulated result performed in COMSOL.

Room Temperature Ionic Liquids are thermally stable thanks to their low vapor pressure. In addition to thermal stability, RTIL can be tailored task specifically by altering cations and anions. Different experiments were conducted to study the capacity of IL's to change the surface temperature of the hotspot generated and this was compared with that of DI water. The latter showed higher capacity to remove heat, while evaporation problem was predominant in the sandwiched setup. Three different ionic liquids, 1-butyl-3- methylimidazolium chloride or [BMIM] Cl, 1-butyl-3-methylimidazolium bis (trifluoromethylsulfonyl) - imide or [BMIM] Ntf$_2$, and [CMIM] FeCl$_4$ showed less effect on changing the surface temperature compared to water. It is due to generally lower thermal conductivity, lower heat capacity and higher viscosity than water.
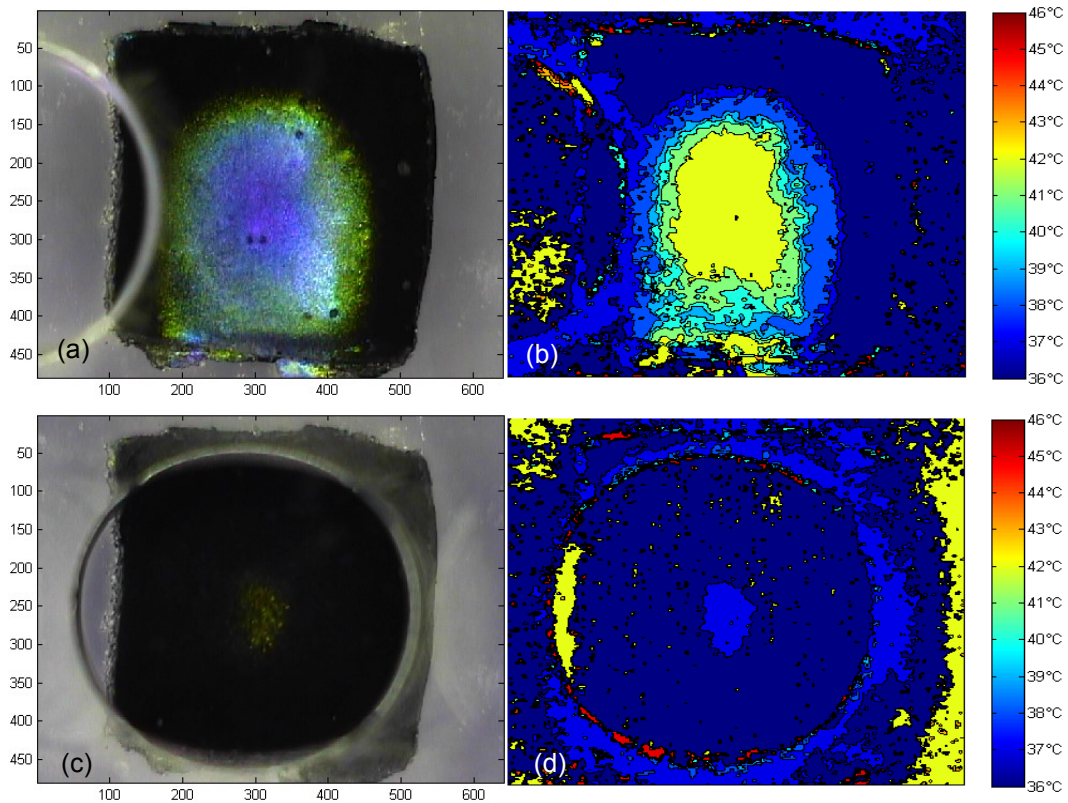
Figure 2-13 Shifted RGB and actual LCT images of pure DI water just before moving on the hotspot [(a), (b)] and after moving onto the hotspot [(c), (d)].

However, RTILs showed high thermal stability by resulting in no evaporation during cooling process while water had vigorous evaporation.

2.3.1 Experimental Results

When pure DI water was moved over the hotspot, considerable temperature change was observed on the hotspot surface. Most of this change was assumed to be dominated by the phase change phenomena of water. An attempt was made to subdue the evaporation effects by surrounding the drop in a shell of pure silicone oil (Clearco Products Co., Inc, PA) of 1cSt viscosity, to prevent the water from evaporating. This however proved futile as phase change was still observed. The LCT results with the silicone oil core shell was worth noting as the temperature of the hotspot was found to be slightly higher than that of pure DI water. This confirmed the fact that phase change of water drop was less severe as the
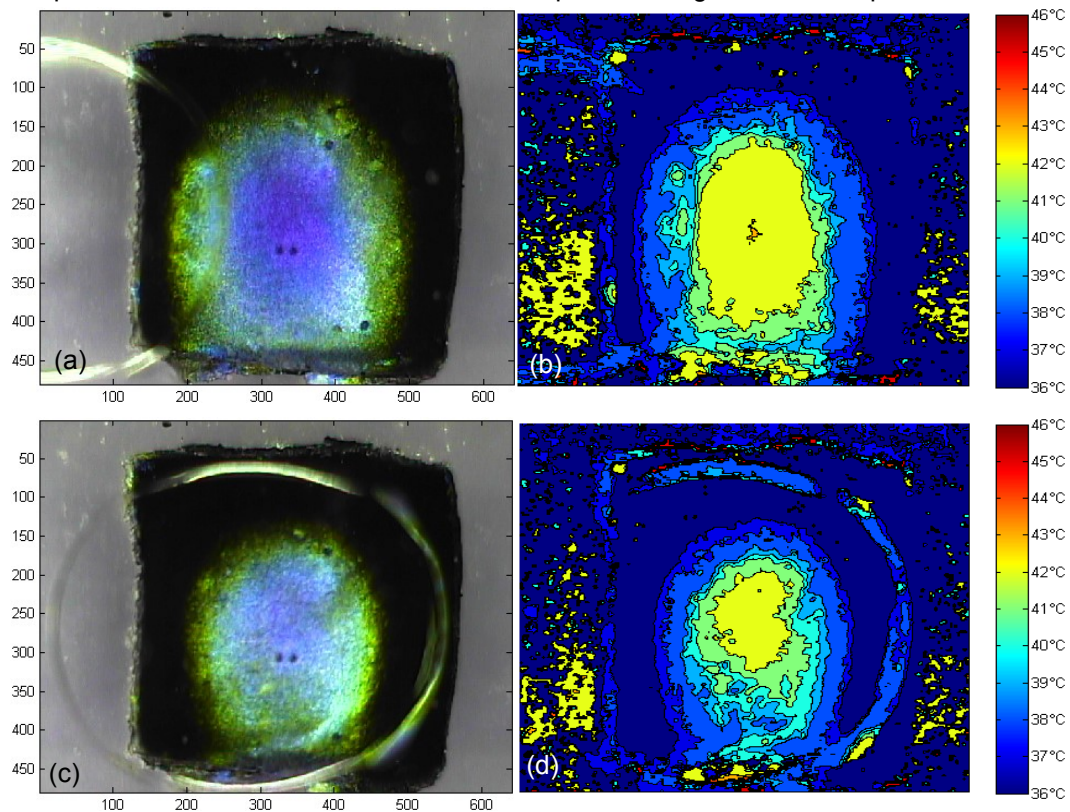
Figure 2-14 Shifted RGB and actual LCT images of IL1 just before cooling [(a), (b)] and after moving onto the hotspot [(c), (d)].

20

silicone oil was trying to contain the water droplet within it. Figure 2-13 show the LCT results of pure DI water. Substantial phase change was observed as the drop was surrounded with satellite drops of water. It was observed that the boundary of the drop and areas around the LC paint in Figure 2-13 (d) showed signs
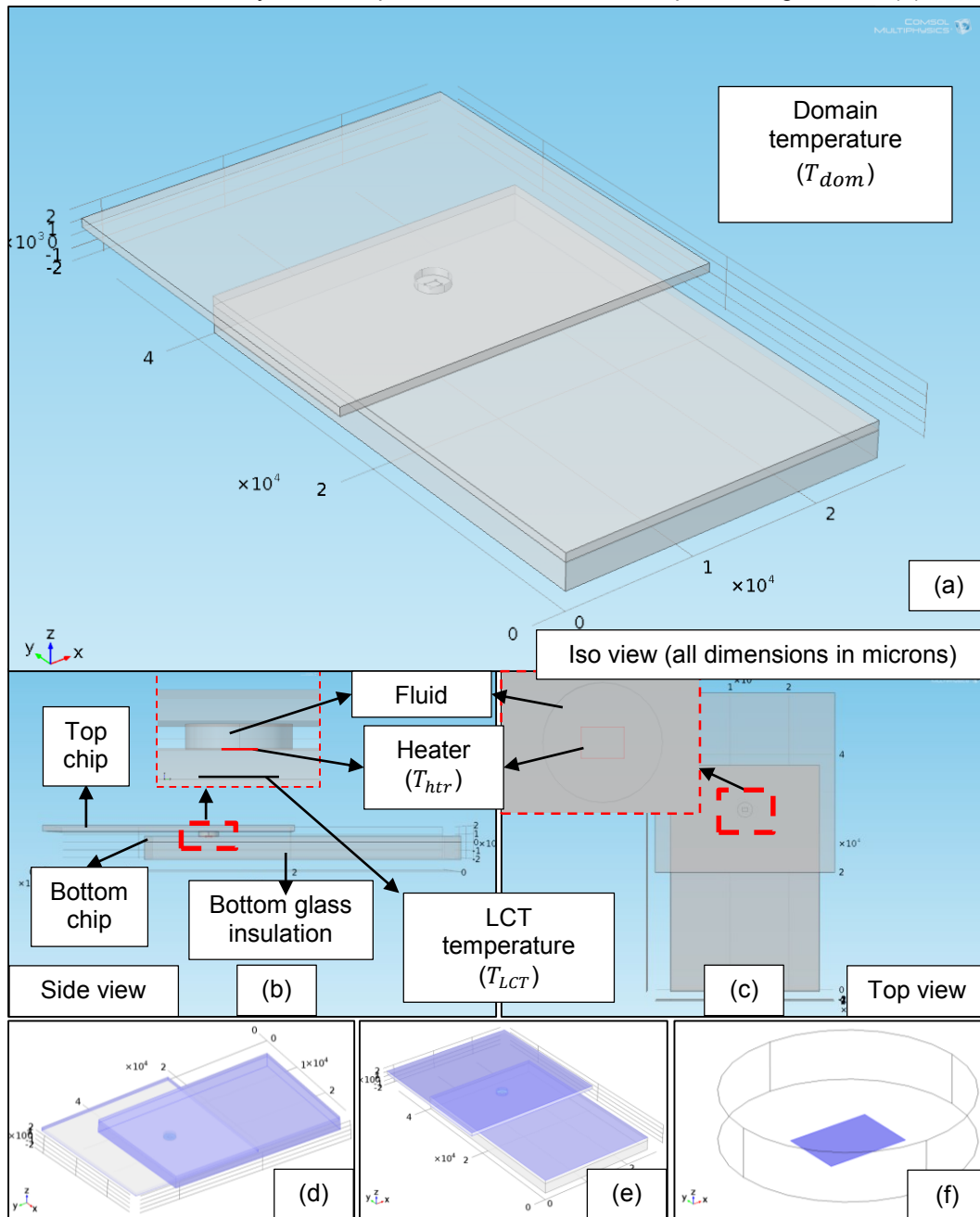
Figure 2-15 3-D model in COMSOL showing the domains considered.

of high temperature. This was purely due to noise and refraction effects of the light passing through the edges of the drop, and must not be mistaken for the temperature. The same holds good for all the LCT contours. For quantitative analysis, only the contour profile within the boundary of the drop was considered. As with the Ionic Liquid in Figure 2-14, albeit the temperature change of the hotspot was not as good as that of pure DI water with and without the silicone oil shell, no phase change phenomena was observed.

2.3.2 Numerical Modeling

The results in section 2.3.1 was analyzed by performing thermal modeling using 3-D transient heat transfer module in COMSOL multiphysics. The goal of the simulation was to compare the spatial LCT temperature profile to that of the experiment. A 3D model setup to scale as shown in Figure 2-15 represents the one in the experiment with the respective boundary conditions (B.C.). The initial condition of all domains was set to room temperature (R.T.). The three glass insulation is combined to one insulation for simplicity (bottom glass insulation). For all the sides and bottom side of the bottom chip, insulation B.C. was set (Figure 2-15 (d)). Natural convection B.C. was set for the top, bottom face of the top chip and the top face
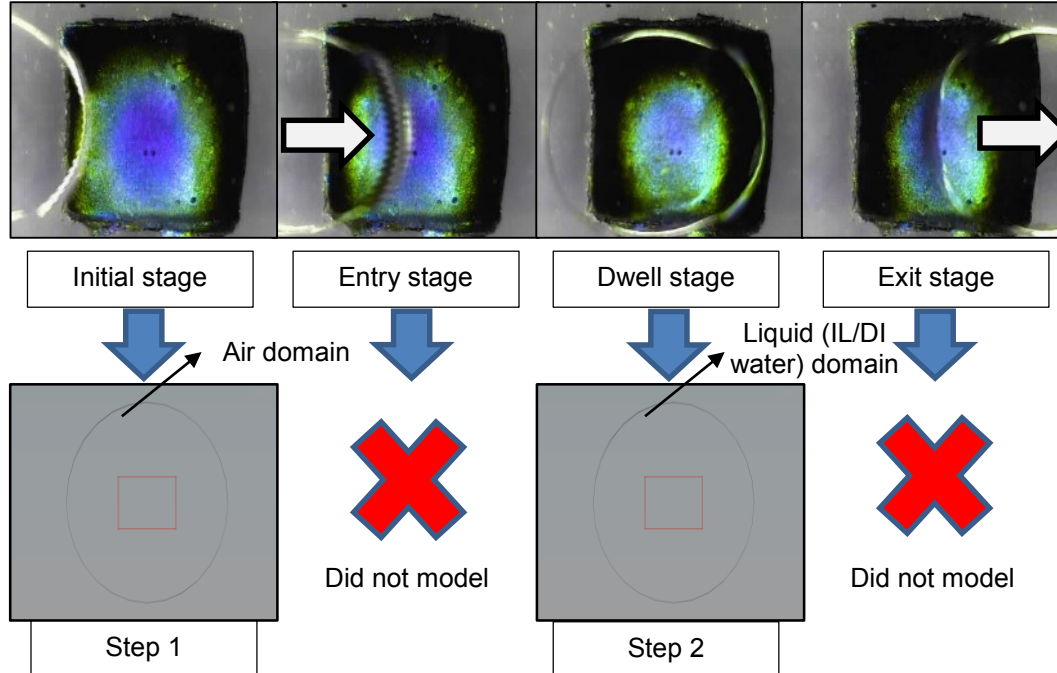
Figure 2-16 Stages modelled in COMSOL without considering droplet motion.

22

of the bottom chip including the droplet meniscus faces (Figure 2-15 (e)). Finally, a heat flux B.C. was applied to the heater boundary as shown in Figure 2-15 (f).
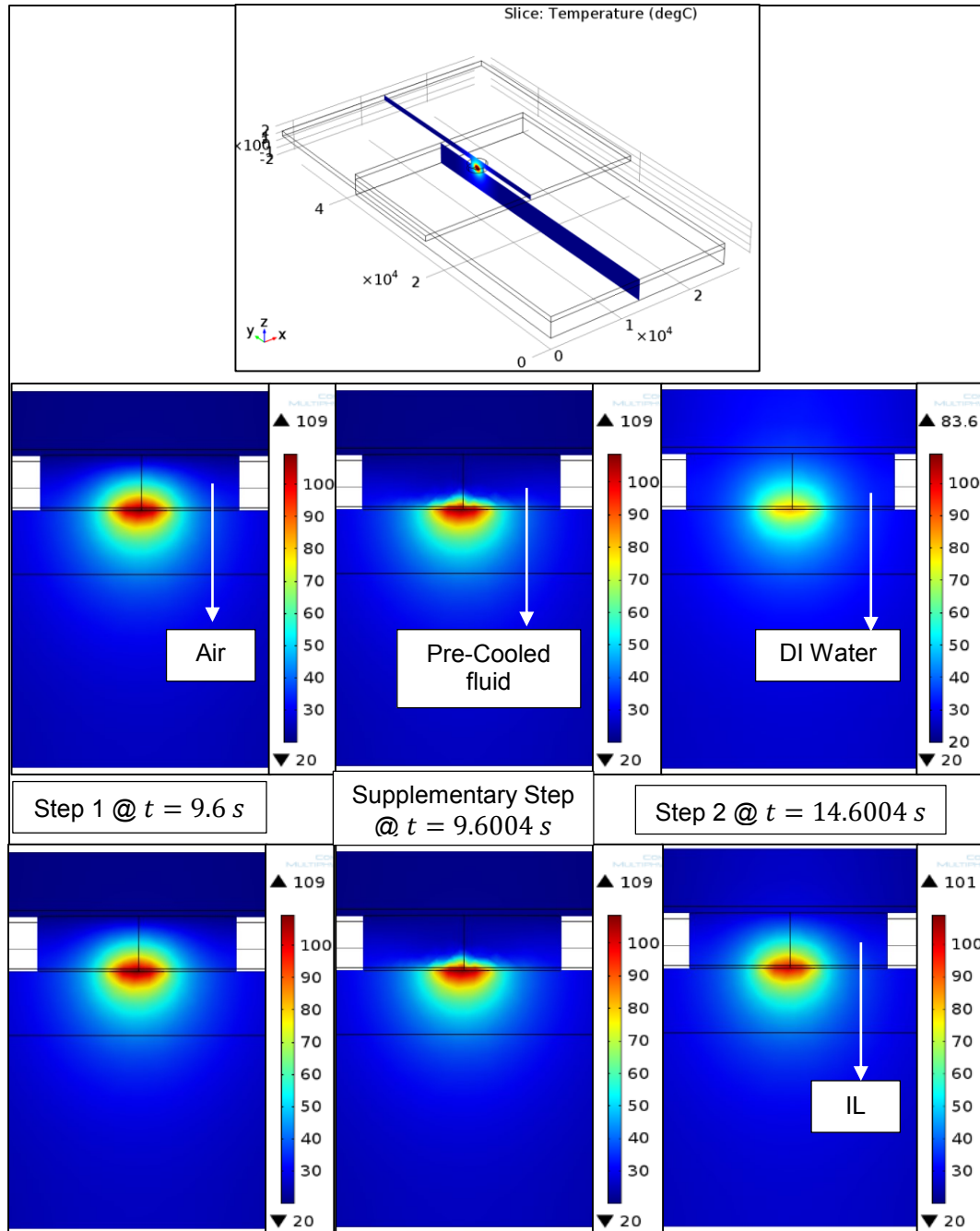
Figure 2-17 Cross-section view of the model showing modelling steps in COMSOL

The drop (fluid domain) is approximated to a cylinder and is sandwiched between the top and bottom chip. The heater is modeled as a surface with its corresponding dimensions. As the computer system resources available for the simulation was generous, a fine mesh size was chosen with sub-modeling for domains of interest for maximum accuracy. As shown in Figure 2-16, the EWOD hotspot cooling involved four stages, namely the initial, entry, dwell and exit. The entry and exit regions correspond to droplet motion which was analyzed to exhibit a complex rolling motion [25] resembling a parabolic velocity profile. Due to the complexity of emulating this droplet motion in COMSOL, this flow physics was not considered in the simulation. In other words, the simulation was performed only using the initial and the dwell stage with conduction heat transfer as the only boundary condition between the drop and chip interface. As illustrated in the previous Figure 2-16, step 1 involved assigning the fluid domain as air and running a transient heating of the fluid for 100 s. The spatial LCT temperature profile at a time interval (Figure 2-17) which matches with that of the experimental result in the initial stage was selected (at t=9.6 s) as the initial condition of step two. In order to reduce the initial temperature of the air domain to meet the assumption of the fluid domain to be at room temperature for step 2, a supplementary step involved running a simulation for 1 ms at 0.1 ms (from t=9.6 s to t=9.601 s) interval with the air domain having a high velocity of 5 m/s. This reduced the fluid domain temperature momentarily (at t=9.6004 s) without changing the substrate temperature (bottom or top chip). With this new information of the spatial temperature profile, the initial condition was chosen for step 2 and the material properties for air domain was replaced with the Liquid (IL & water) respectively and the simulation was run for the dwell stage lasting 5 s (from t=9.6004 s to t=14.6004 s).

2.3.3 Simulation Results - Comparison with LCT

The simulation results corresponding to the temperature at the base of the bottom chip were plotted and compared with the LCT results. A zoom window was selected based on the size of the droplet which closely matched that in the experiment. Figure 2-18 compares the results for DI Water. It was observed that the spatial distribution of LCT temperature in the simulation appeared to be smaller than the experimental
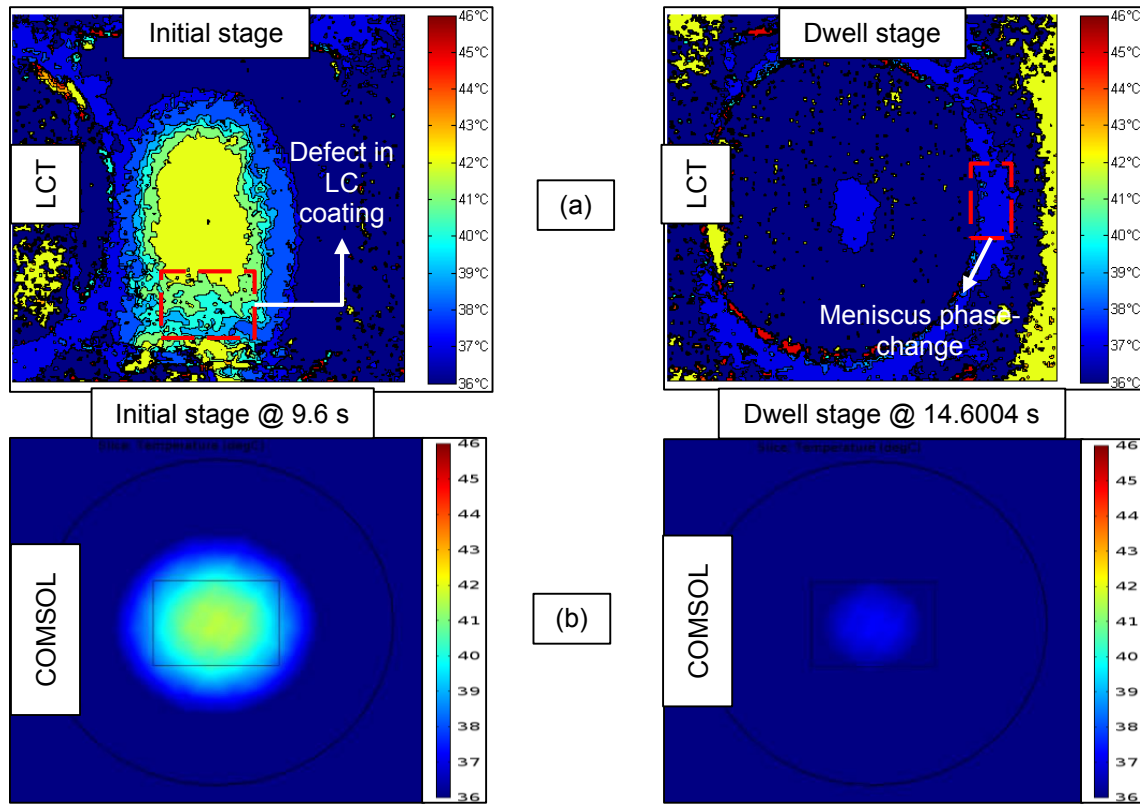
Figure 2-18 DI water results comparing COMSOL simulation with experimental result (a) before drop cooling & (b) after drop cooling.

result (oval appearance of hotspot). This can be attributed to the fact that the LCT analysis used in the experiment was a crude temperature measurement with low spatial resolution resulting in a larger area having same temperature. The large size also indicated that the LCT sheet might have some defects (for example, at the very base of the sheet as marked). In addition to the observations made about the hotspot, the LCT result also showed a ring shaped temperature profile around the droplet. This was not observed in the simulation due to the fact that the meniscus thickness also contributed to the image analysis although it did not represent any temperature profile.

Similarly with IL (Figure 2-19), the temperature profiles looked different with the LCT results appearing bigger than the simulation results. The same reasons as explained before can be outlined here. The following plot shows the corresponding temperatures in step 1 and the drop temperature included in

25
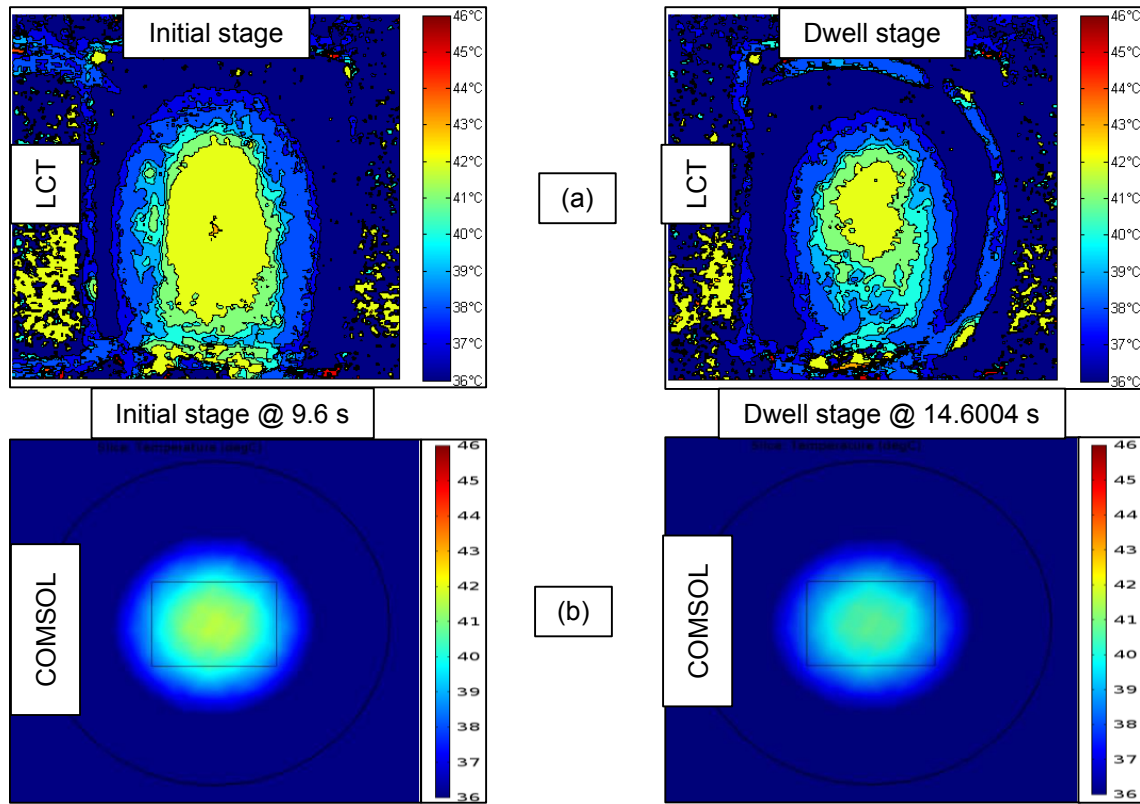
Figure 2-19 IL results comparing COMSOL simulation with experimental result (a) before drop

cooling & (b) after drop cooling.

step 2. It was observed that the final hotspot temperature was higher than that of DI Water due to better

thermal properties (thermal conductivity and heat capacity).

A plot was made (Figure 2-20) between the maximum hotspot temperature and the maximum LCT

temperature (at the backside of bottom chip) for step 1 and step 2 respectively. Step 1, as explained before,

involved transient heating in the air domain from 0 to 9.6 s. Step 2 involved cooling of the temperature

profiles in the water domain from 9.6004 s to 14.6004 s and shows the average fluid temperature plotted

along with the hotspot and the LCT temperature.
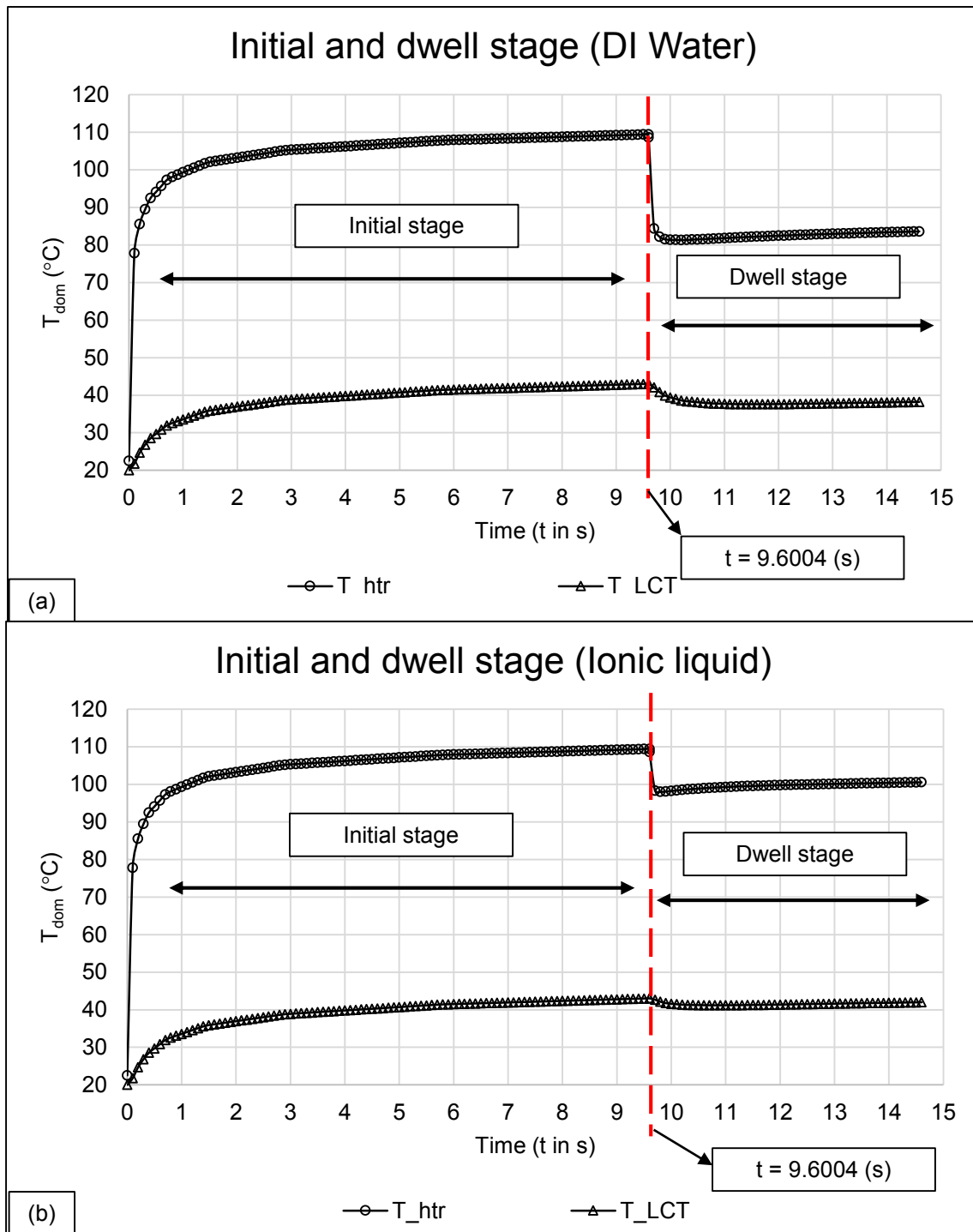
Figure 2-20 DI water (a) and IL (b) results for temperature in COMSOL.

2.3.4 Simulation Results - Meniscus Evaporation
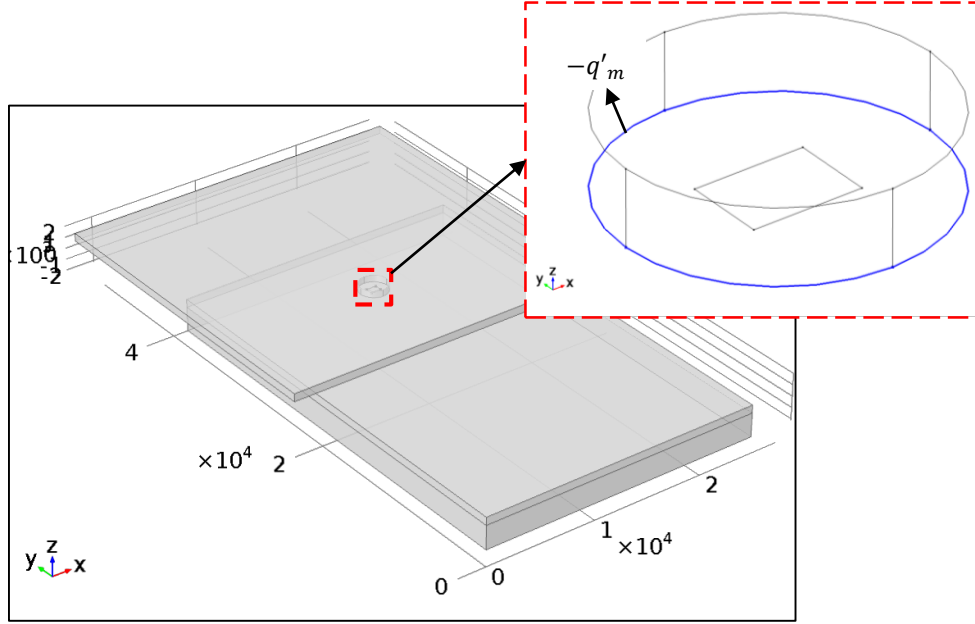
Figure 2-21 Meniscus evaporation B.C. applied at edge of meniscus.

From the LCT experimental results with DI water (Figure 2-13), we saw significant condensation around the drop meniscus at the entry and dwell stages due to the evaporation of the meniscus as the temperature of the drop rises. In the previous sections, the COMSOL simulation results with DI water did not account for evaporation as we did not model phase-change heat transfer from the drop meniscus. In the present section, we emulated evaporation by modifying our simulation with an addition of an edge boundary condition, q'_m as shown in Figure 2-21. A '−' sign was prefixed to the boundary condition to denote heat removed as latent heat of vaporization. A parametric analysis was performed for a range of values until the temperatures at end of dwell stages seemed acceptable. Figure 2-22 shows the heater temperature for the range of evaporation boundary conditions imposed. For q'_m = 0 W/cm (no evaporation) to q'_m = 3x10^{-2} W/cm, T_{htr} at the end of the dwell region dropped by 1 °C. A similar drop in temperature was seen in case of the LCT temperature except that the transient behavior in the dwell region is different

28
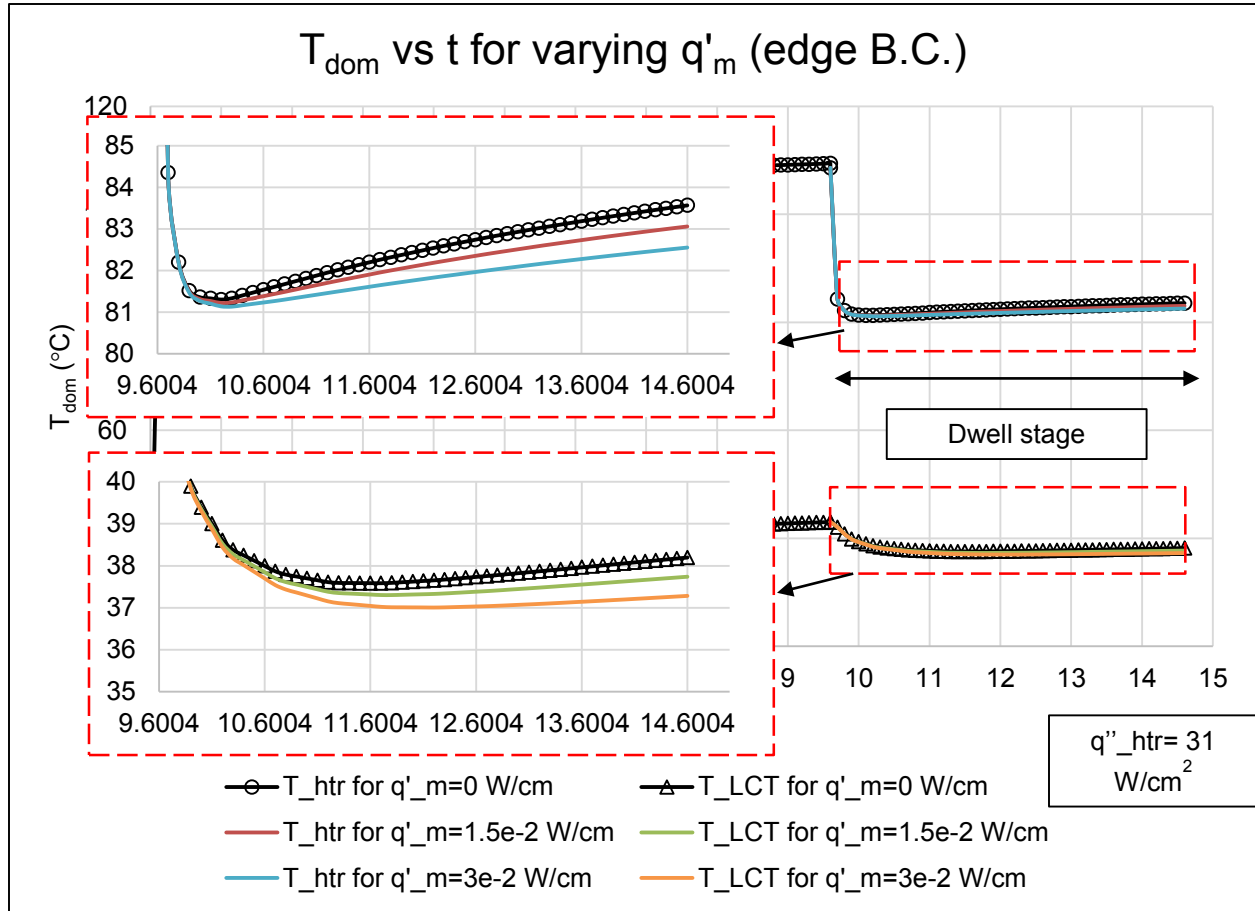
Figure 2-22 Simulation results showing effect of meniscus evaporation B.C. on T_{htr} and T_{LCT}.

as the boundary under consideration does not see the drop directly and the conduction through the substrate delays thermal gradient to remain constant. The results of experiments and the simulations are summarized in Table 2-1.

Table 2-1 Summary of results with LCT and comparison with simulations for DI water and IL.

Type of results	LCT	COMSOL simulation		
Temperature drop	ΔT_{LCT} (°C)	ΔT_{LCT} (°C)	ΔT_{htr} (°C)	q'_m (W/cm)
DI water	4	6	28	3×10^{-2}
IL	1	2	11	-
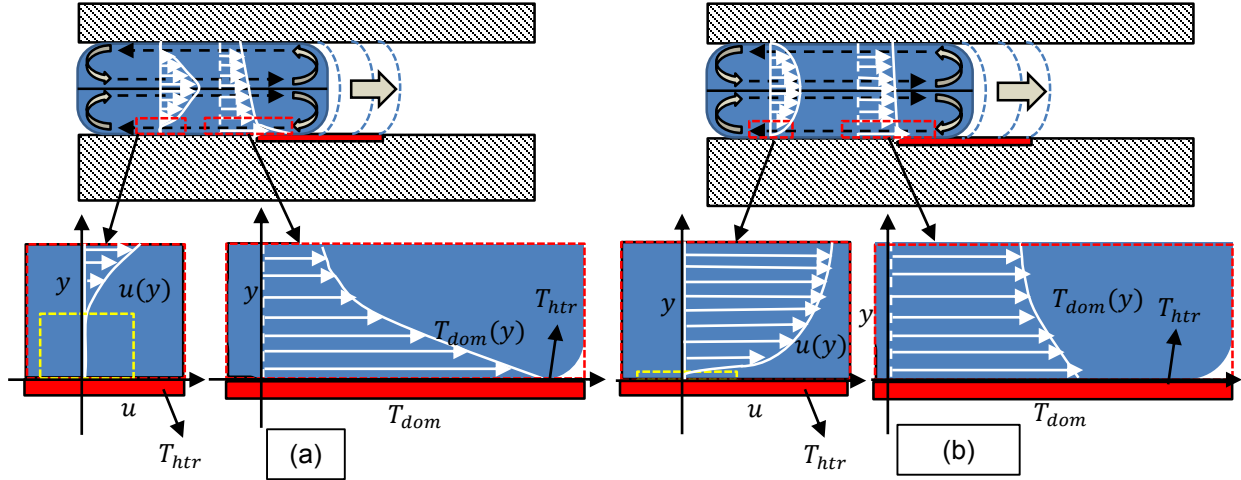
Figure 2-23 Velocity and thermal boundary layer for IL (a) and DI water (b).

The results with IL and DI water showed that IL had poor cooling capacity than the other coolant. This was attributed to poor thermal properties such as low thermal conductivity and heat capacity. Moreover, evaporation, which was initially suppressed, limited heat transfer to only single-phase from the hotspot to the droplet. In addition to these causes, efforts were made to look into the viscosity of the droplet as IL had a higher viscosity (1701 cSt @ 30 °C [26]) than that of DI water (0.8 cSt @ 30 °C). Upon closer observation of the velocity boundary layer in Figure 2-23, there existed a thicker no-slip boundary due to high shear forces in the case of IL. This also resulted in a flatter domain temperature gradient $\frac{dT_{dom}}{dy}$ therefore affecting the heater temperature, T_{htr}. In case of DI water, due to low viscosity, the no-slip boundary is less thick hence resulting in a steeper $\frac{dT_{dom}}{dy}$ resulting in lower T_{htr}.

2.5 Conclusions

In this chapter, a proof-of-concept cooling device was fabricated and setup to demonstrate droplet motion over hotspot using EWOD. LCT was performed in order to measure the temperature drop at the bottom of the device. Numerical simulations in COMSOL were done to estimate transient heater temperature and also validate the LCT results. DI water turned out to be the coolant of choice for future tests due to better cooling capacity.

CHAPTER 3

INTEGRATED EWOD DMF COOLING SYSTEM

3.1 Motivation

In the previous chapter, an innovative temperature measurement technique using LCT was presented. Albeit its innovation, it was a crude temperature measurement technique as the LC material was not directly at the hotspot. Moreover, the coating itself was not perfect and resulted in some defects in the material causing a considerable mismatch in the spatial temperature distribution with that of the simulation results. This chapter is based on work performed in [27], which deals with an improved hotspot temperature sensing with Indium Tin Oxide (ITO) based Resistance Temperature Detectors (RTDs). These RTDs were fabricated close to the droplet contact surface as shown in Figure 3-1.
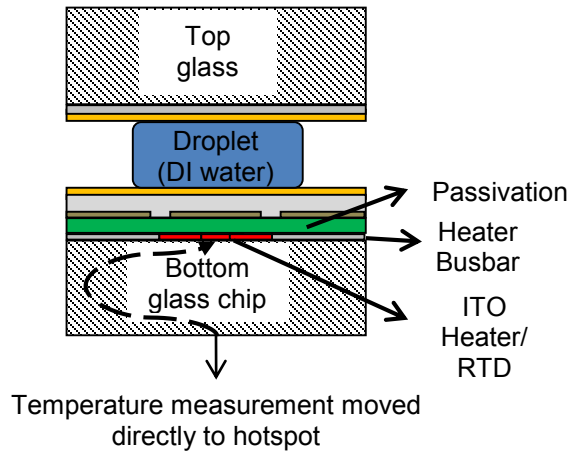
Figure 3-1 Direct hotspot temperature measurement was made possible using ITO RTD.

In addition to improving the temperature sensing, a Plexiglas EWOD setup was also designed and assembled to improve integration of the electrical and fluidic connections to the top and bottom chips as shown in Figure 3-2. The setup enabled better control of experimental parameters like thermal insulation, ambient convection around the hotspot, spacer gap and ensured robust connections to the RTD busbars and EWOD voltage terminals. As ITO remained the material of choice for the EWOD grounding (top chip) in the co-planar configuration, usage of the Plexiglas setup did not compromise the video data acquisition

31

of the droplet cooling around the hotspot. Moreover, as the RTD temperature data was recorded real time along with the video capture, more efforts were made on analyzing the visual data and relating it with the RTD temperature. The end goal was to make measurements with DI water and record phase-change effects.
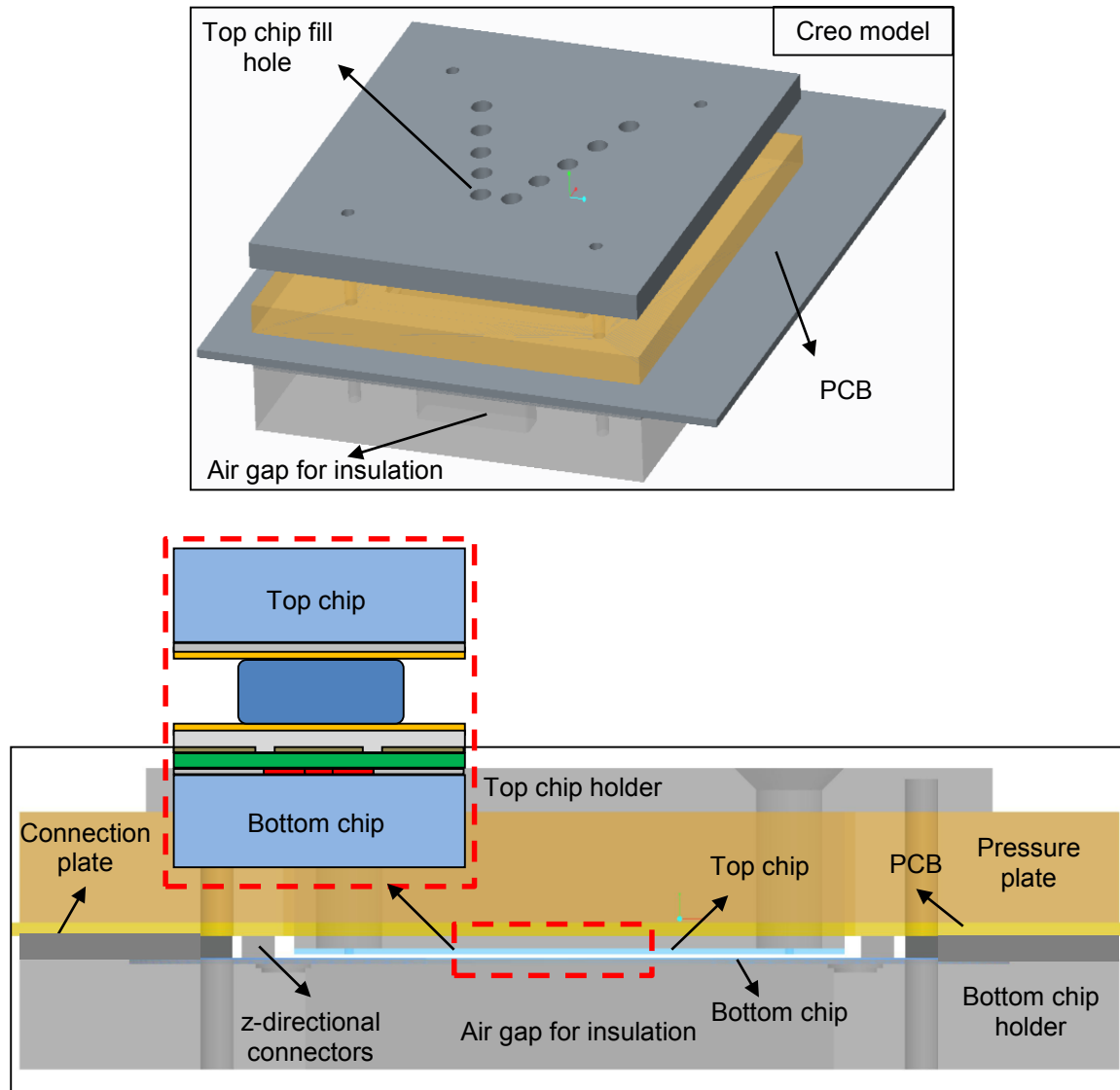
Figure 3-2 CAD models showing integrated setup of the revised EWOD DMF design with ITO RTD.

3.2 ITO RTD Hotspot Cooling Setup

Referring to Figure 3-3, the original hotspot device consists of a top chip and a bottom chip, which were placed in a parallel – plate configuration. These chips were fabricated in a clean room using conventional thin film semiconductor fabrication techniques which will be explained later. The bottom chip comprises an ITO heater which emulates the hotspot and also doubles as an RTD (Resistance temperature detector). Chromium was used for patterning the EWOD electrodes which were aligned with the heater and defined the pathway for the droplet motion. Su-8 (5 μm thick) was used as the dielectric for EWOD and a thin layer of Teflon was coated on the dielectric for hydrophobicity. Similarly, the top chip was completely coated with ITO for EWOD grounding purpose and was also coated with Teflon. After the top and bottom chips were fabricated, the EWOD device was assembled by placing the top chip on top of the bottom chip separated by spacers.
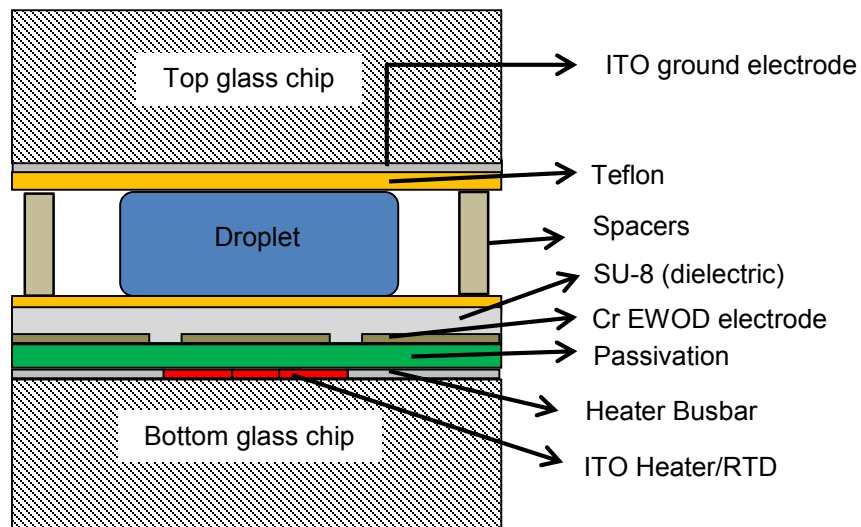
Figure 3-3 Cross-section of the EWOD device with corresponding layers.

3.2.1 EWOD Electrodes using Chromium (Cr)

The EWOD electrodes were fabricated using clean room semiconductor fabrication techniques as discussed in the previous section. Figure 3-4 shows the design which included multiple rows of varying
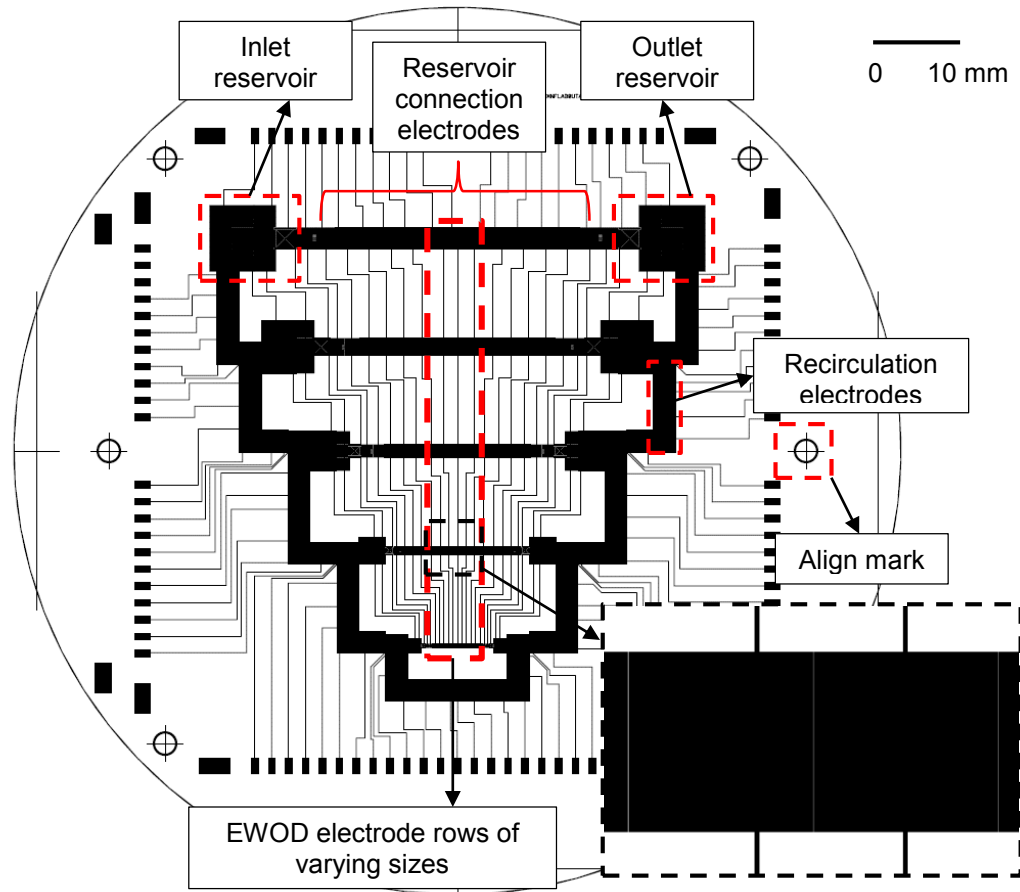
Figure 3-4 Cross-section of the EWOD device with corresponding layers.

EWOD electrode sizes (2.5 mm^2 to 0.5 mm^2) with each row connected to an inlet and an outlet reservoir sections. The reason for choosing varying sizes of electrodes was in order to experimentally test the effect of mass flow rate of coolant on the temperature of the hotspot. Each of these rows were further connected to each other by electrode pathways which facilitate drop to be recirculated from the exit reservoir to the inlet reservoir. The connections to the connection electrodes was provided by a set of common terminals towards the top of the design while the reservoir and the recirculation pathways were branched out to the left and the right of the design. Six align marks around the edge of the design ensured that the EWOD electrode layer perfectly aligned with the rest of the layers, especially the ITO heater/RTD design.
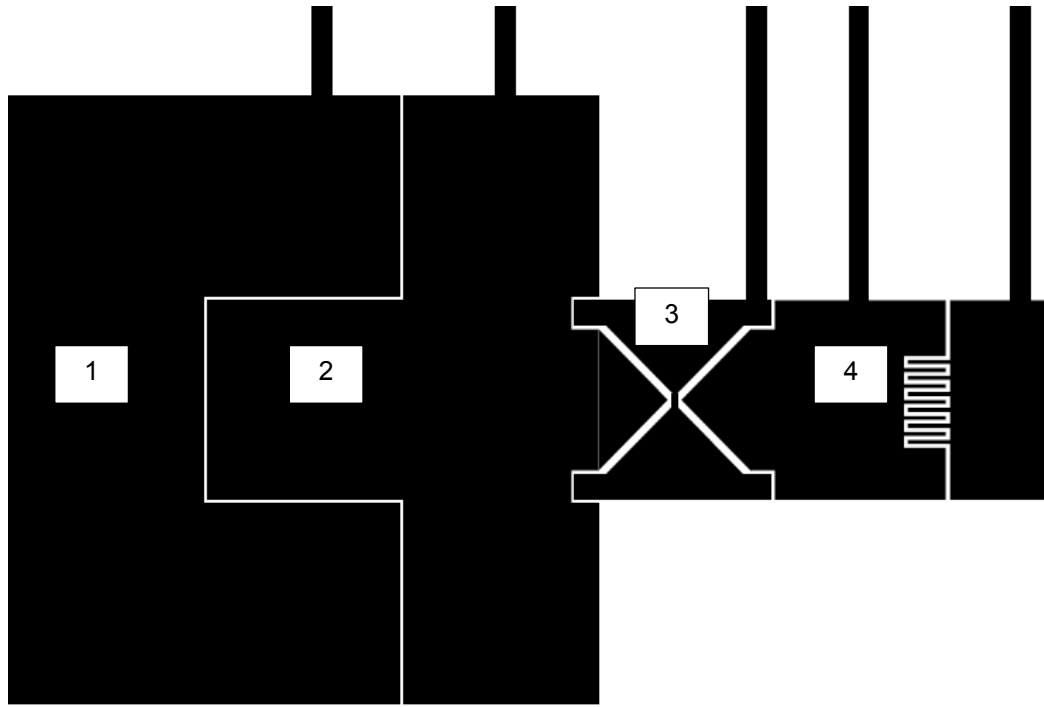
Figure 3-5 Reservoir design with droplet pinch-off taking place at electrode # 3.

The reservoir design (Figure 3-5) had the aim of filling liquid from an external syringe pump onto electrode 1 & 2 (backing electrodes) and forming a liquid column on electrodes 3 & 4. Electrode 3 was used as a pinch off site to generate a droplet from the reservoir pool. The droplet, after forming on electrode 4, traversed across the connection electrodes and reached the exit reservoir for collection and recirculation.

3.2.2 Temperature Measurement with ITO heater/RTD

Indium Tin Oxide was used as the material of choice for the heater/RTD due to its ease of integration with the EWOD device fabrication, optical transparency and good linear PTC (Positive Temperature Coefficient) characteristics. The heater/RTD was fabricated on a 4 inch glass substrate with a sputtered film of ITO pre-deposited on it. As shown in Figure 3-6, the heating element comprised serpentine shaped patterns of 25 µm width and 1200 Å thick. With a sheet resistance of 7 Ohm/square, the resistivity of the film was 0.84×10^{-6} Ω.m. The length and width of the RTD was 5060 µm and 25 µm respectively. With these parameters, the resistance of the heater was around 1400 Ω. Several sections of

bus bars were also connected to the heater element so as to provide electrical contact to the outer perimeter of the substrate. Wires were directly soldered onto Ni coated busbars to establish zero contact resistance. The solder was covered with epoxy paste and cured to form a robust connection. In order to provide power to the heater, a sourcemeter (Keithley 2400 DC) was used and power was supplied to the heater to emulate hotspot of heat fluxes 8.7 W/cm^2, 20 W/cm^2 and 36 W/cm^2. The entire chip design spanned heater/RTDs across all the rows of the EWOD electrodes connecting the reservoirs in such a way that the RTDs were directly aligned below the middle electrode in every row as shown in Figure 3-6. Each of these sensors had
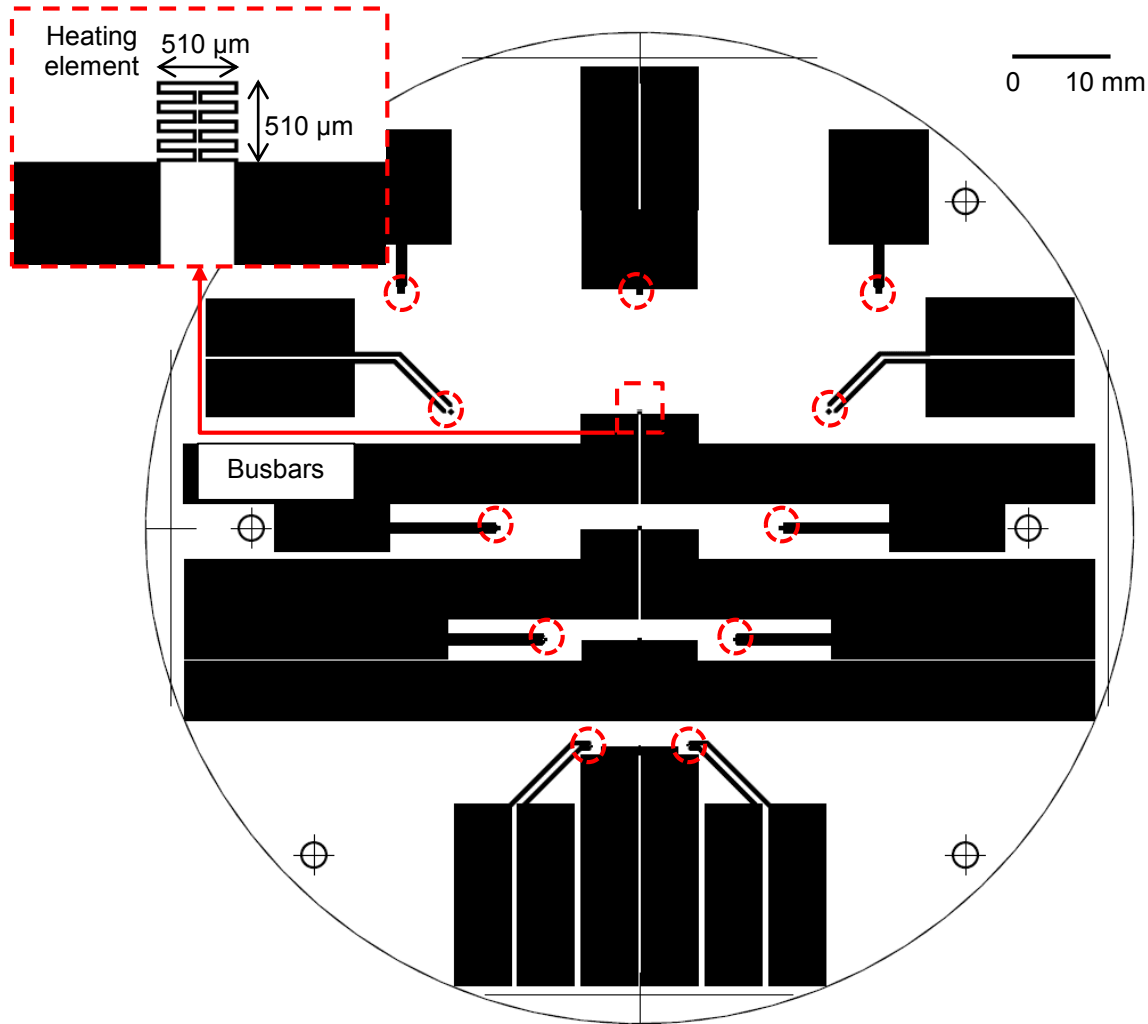
Figure 3-6 Heater/RTD photolithography mask showing the reservoir RTDs (dashed circle) with busbars.

busbars which fanned out to the outer perimeter of the substrate. In addition to the heater/RTDs, the design also incorporated RTDs at the reservoir sites to measure the inlet and exit temperatures of the liquid in each row. The RTDs also had a similar design to the heater, the only difference being that the operation of the RTD was limited to a sensor.

3.2.3 Top and Bottom Chip Fabrication

The top and bottom chips which constitute the EWOD hotspot cooling device was fabricated using thin film semiconductor fabrication techniques at Shimadzu Institute of Research Technologies, UTA. As shown in Figure 3-7, an ITO coated substrate was first spin coated with HMDS at 3000 RPM for 30 seconds followed by a soft bake on a hotplate at 150 °C for 90 seconds. Next, a layer of Photo Resist (PR) was spin coated at 4000 RPM for 30 seconds. The wafer was soft baked at 115 °C and then exposed using an I-line photolithography machine for 7 seconds. A post exposure bake was performed on the hotplate at 110 °C for 1 minute and then the substrate was immersed in a developer solution until the exposed PR dissolved completely leaving behind hard baked PR patterns representing the layout mask used during exposure. Next, the wafer was immersed in an ITO etchant solution constituting a 1:8:15 volume ratio of HNO3, HCL and DI water heated at 55 °C on the hotplate in order to complete the ITO heaters and RTDs patterning. After the etching was performed for 2 – 3 minutes, a PR stripper solution was used to remove the hard baked PR which remained unaffected by the ITO etchant. The wafer was cleaned and dehydrated before processing it in PECVD in order to deposit a 1 um thick layer of SiO2 on it. The wafer was then processed in an e-beam evaporator to deposit a 100 nm thick layer of Cr for EWOD patterning steps that followed. PR was once again used to spin, expose, bake and etch the Cr EWOD electrodes on the wafer using the same steps as done for patterning the ITO heaters and RTDs. Once the PR was stripped, a 5 um thick SU-8 layer was spin coated, exposed and developed to form the di-electric layer. A thin layer of Teflon was spin coated in the end to form a hydrophobic layer on the active sides of the wafer and the top chip.
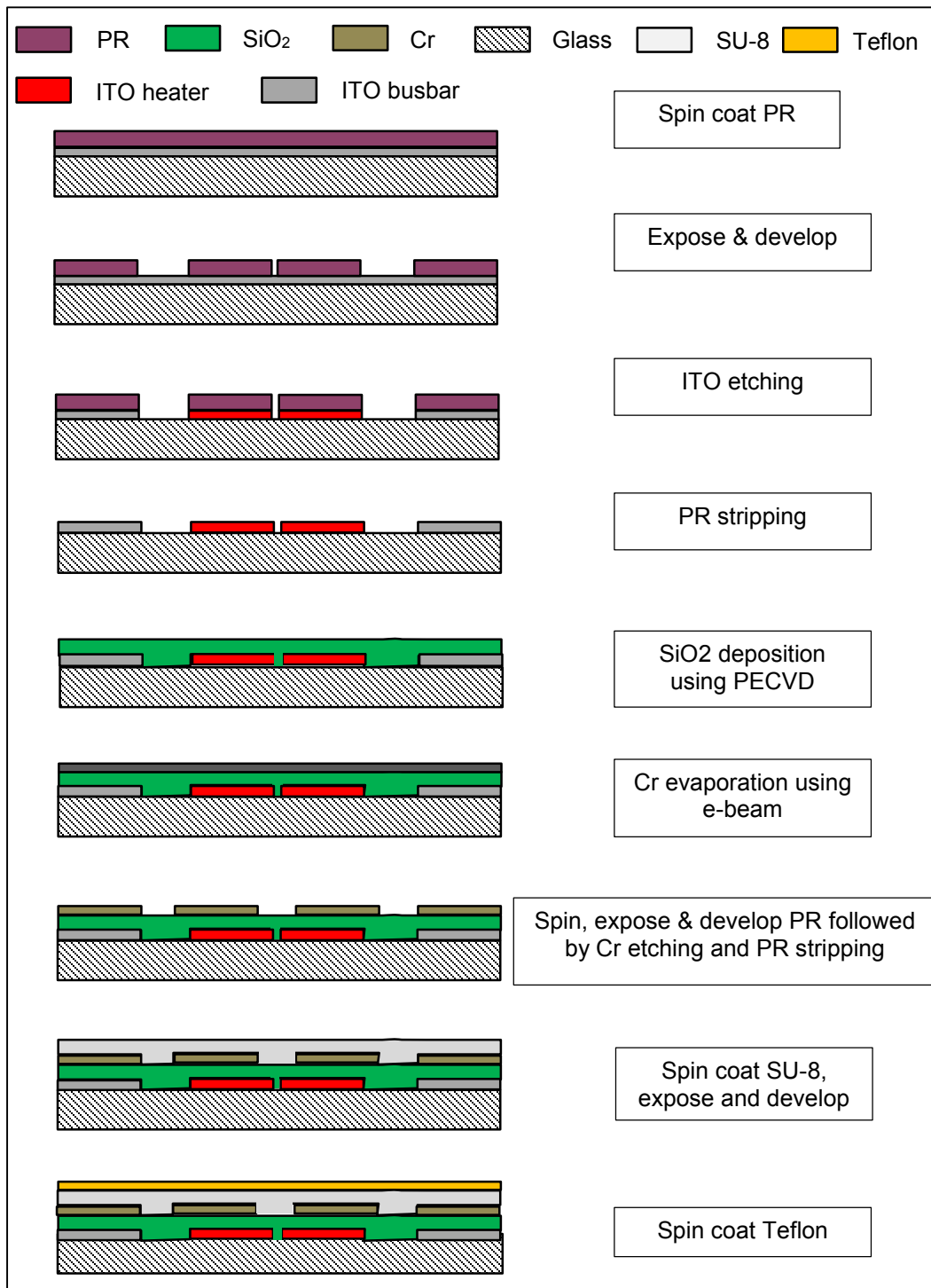
Figure 3-7 Device fabrication process for bottom chip.
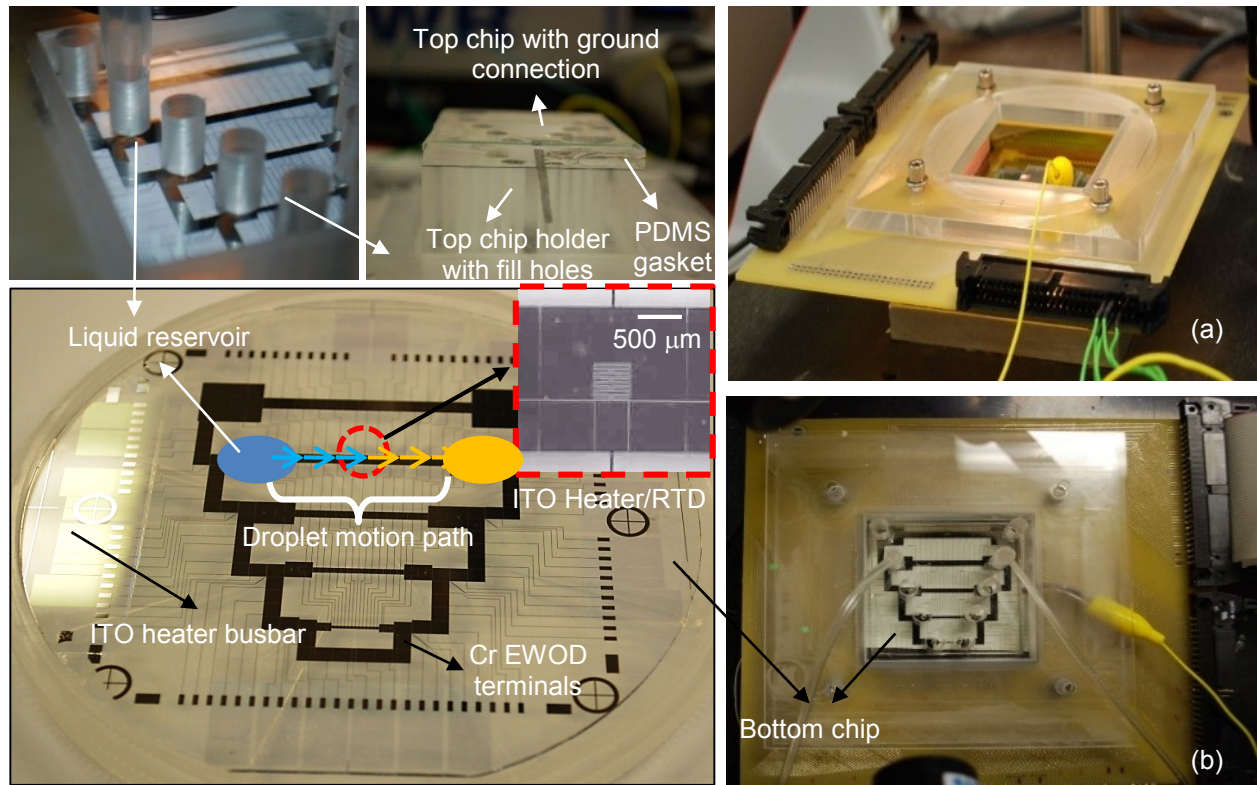
Figure 3-8 Final assembled device (a), (b) with fabricated bottom chip showing provisions for liquid filling on inlet and exit reservoirs. PCB for integrating EWOD DAQ is also seen.

3.2.4 Integrated EWOD and heater/RTD Setup

Figure 3-8 shows the final bottom and top chips with the inlet and exit liquid reservoirs. In order to integrate the EWOD and the RTD connections on chip, a multiple piece Plexiglas setup was designed and manufactured to accommodate the top and bottom EWOD chips. A PCB connection board was interfaced within the Plexiglas setup to provide electrical connections to the chip. The bottom chip holder had a slot for inserting the bottom chip (wafer) to hold it in place. Below every heater/RTD, there were empty pockets which acted as insulation for the hotspots. A set of z-directional connectors interfaced the PCB to the bottom chip and provided electrical connections for EWOD actuation through a switch board and DAQ system. A pressure plate kept the PCB and the connection plate together and prevented the PCB from bending to pressure and losing contact with the connectors. The top chip holder held the top chip by means of a PDMS

(company) gasket. The ratio of the curing agent to the PDMS was chosen as 10:1 for optimum stiffness. Holes were drilled on the top chip directly at the corresponding inlet reservoir sites that aligned with the bottom chip. Holes were correspondingly punched in the PDMS gasket using a bio punch tool of about 1 mm diameter. The top chip was plasma bonded to the gasket and the bonded duo was pressed against the flat and un-machined base surface of the holder. The suction created by the force applied was enough to keep the top chip attached to the holder. To complete the fluidic circuit, a tube was inserted into a pipette tip (Eppendorf Inc.) and the tip was inserted through holes in the holder and pushed into the hole in the gasket. The other end of the tube was connected to a syringe which was placed in the syringe pump (KDS 100) with its plunger in contact with the active head of the pump as shown in Figure 3-9.
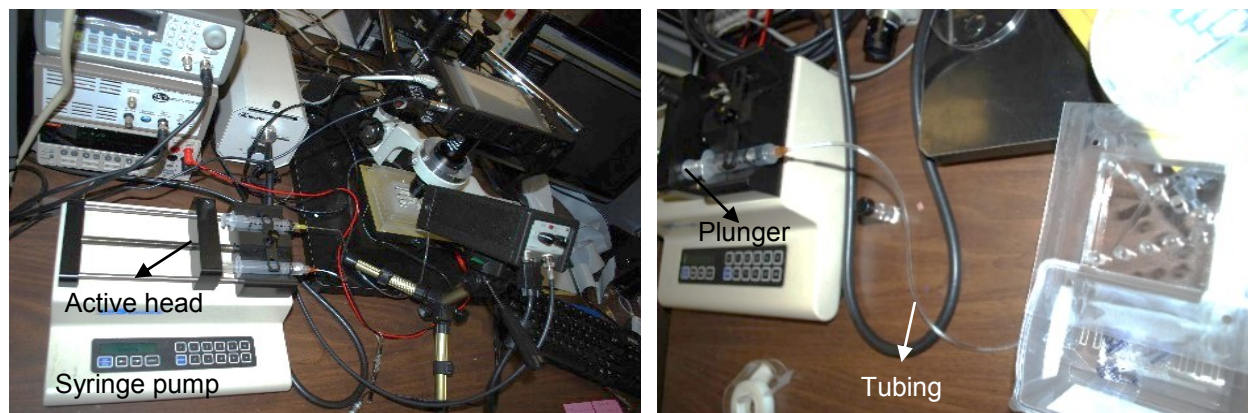
Figure 3-9 Setup showing the syringe pump and tubing into the top chip holder.

3.2.5 Calibration of ITO Heater/RTD

As mentioned before, Indium Tin Oxide was used as the material of choice for the heater/RTD due to its ease of integration with the EWOD device fabrication, optical transparency and good (linearity) Positive Temperature Coefficient (PTC) characteristics (Figure 3-10). The heater/RTD was calibrated using an oil bath in a well-insulated jar on a hotplate. Three trials were conducted and the error bars were plotted to show good repeatability.
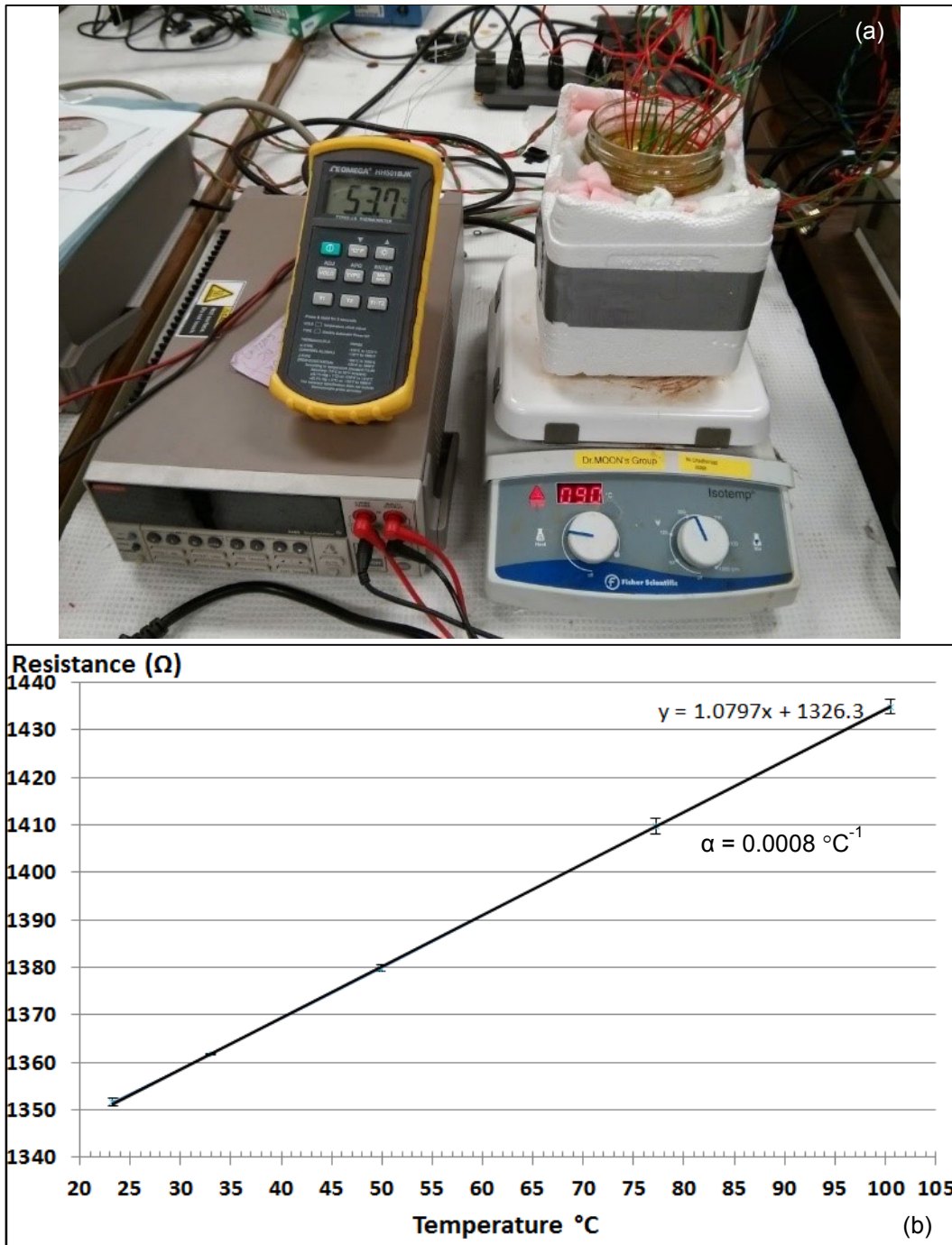
Figure 3-10 Calibration in a constant temperature oil bath (a) with data (b).

3.2.6 Experimental setup and procedure

As shown in Figure 3-11, the experimental setup used primarily included the DAQ and power supply

for the heater/RTD (Keithley 2400 Sourcemeter), voltage supply for EWOD (Agilent 33220A 20 MHz

Figure 3-11 Experimental setup showing various hardware.
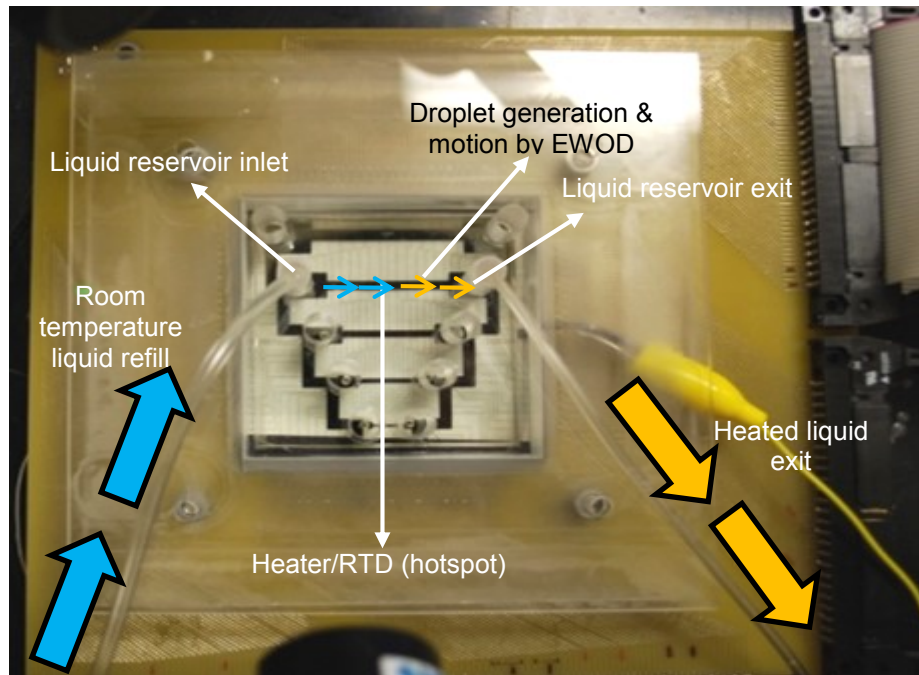
Figure 3-12 ITO RTD EWOD DMF cooling device showing process of filling liquid at inlet, generating drops over hotspot and collection and disposal of liquid at exit.

Function/Arbitrary Waveform Generator in conjunction with Trek Model PZD350 voltage amplifier) electrodes and a computer controlled DAQ system as shown in Figure. The DAQ system included a switch board and interface cards (NI PCIe 6509 card and custom switchboard using PCB Express software) for controlling signals to the EWOD electrodes on chip and to power and acquire the RTD data simultaneously (Keithley KPCI-488A). This interface card was connected to a digital multimeter data acquisition and datalogging system (Keithley Model 2700) with a 20-channel, differential multiplexer module (Keithley model 7700) installed in one of the multimeter's module bays. The channels could conveniently connect upto 20 RTD connections in 2-wire mode or upto 10 connections in 4-wire mode. In order to visualize the droplet motion and record video, a high speed camera system (Fastec TS3) was used. An LED lighting system with wavelength outside of the IR spectrum was used (Metaphase Technologies Inc., MP-LED-150) in conjunction with a ring fiber optic cable attached to a high magnification lens (Edmund Optics). After the top and bottom chips are fabricated, the EWOD device was assembled by placing the top chip on top of

the bottom chip separated by spacers. Figure 3-12 shows the EWOD DMF cooling device with inlet and exit liquid reservoir. After the EWOD device was interfaced to the electronics using PCB, coolant liquid was filled through the inlet using a syringe pump and drops were generated by EWOD which moved from the inlet to the exit over the hotspot. The heater was connected to the DAQ (Digital Acquisition) instrument for measuring the RTD resistance readings.

Table 3-1 Properties of IL and DI water coolants.

Coolant Liquid	Thermal conductivity, k (W/m.K)	Density, ρ (kg/m³)	Heat capacity, Cp (J/kg.K)	Dynamic viscosity, μ (cSt) @ 30 °C
IL	0.19	1571	1100	1701
DI water	0.56	1000	4000	0.8
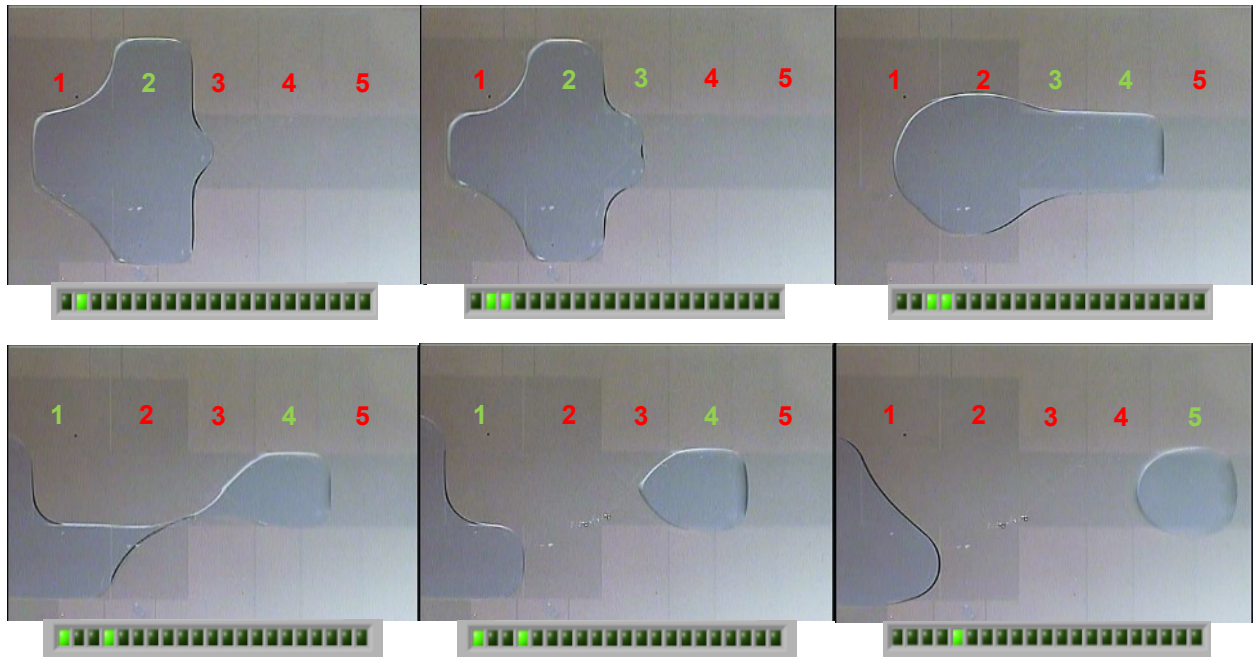
Figure 3-13 Single droplet generation from reservoir electrodes (1, 2) onto the EWOD electrodes (4, 5) with droplet pinch-off at 3. Electrode actuation sequence is shown below the corresponding snapshot.

Table 3-1 compares relevant properties of DI water to that of IL. DI water was chosen as the coolant over IL due to its better thermal conductivity, high heat capacity and latent heat of vaporization. The

performance of EWOD motion is also good as the viscosity was low and the surface tension was high, hence providing better EWOD pumping pressure. The experimental procedure started with turning ON the heater and dispensing liquid in the inlet reservoir electrodes. By using a specific switching pattern, liquid droplets of 600 nL volume was generated from the reservoir and transported over the hotspot to the exit reservoir. As shown in Figure 3-13, a DI water droplet was generated from the reservoir electrodes to be moved over the hotspot electrode.. Electrodes 2, 2 & 3 and 3 & 4 were first actuated consecutively to form a neck of the droplet. Following this, electrodes 1 & 4 were actuated to form a neck and attain pinch-off. . As the droplet moved over the hotspot, the temperature of the hotspot decreased thus decreasing the resistance. Once a droplet left the hotspot, it made way for another droplet to pass over it. By repeating this process for multiple droplets, the resistance data of the heater over time was collected, analyzed with the calibration data and a temperature plot was made for further analysis.

The syringe pump was optimized to deliver the liquid into the inlet at a flowrate of 16 μL/min. However, this flowrate was not an accurate value as only 14 to 16 droplets were successfully generated after which the reservoir either had too much or too less liquid where droplets started to merge forming a long liquid column or did not pinch-off respectively. This also made droplet volume consistency hard to achieve beyond 14 to 16 droplets. This was because the flow rate depended on the diameter of the fill hole on the top cover chip and the spacer gap, parameters which were hard to estimate and control during the start of every test. Future tests can incorporate better control of these parameters to enable higher droplet generation for multiple droplet cooling as proposed in CHAPTER 6.
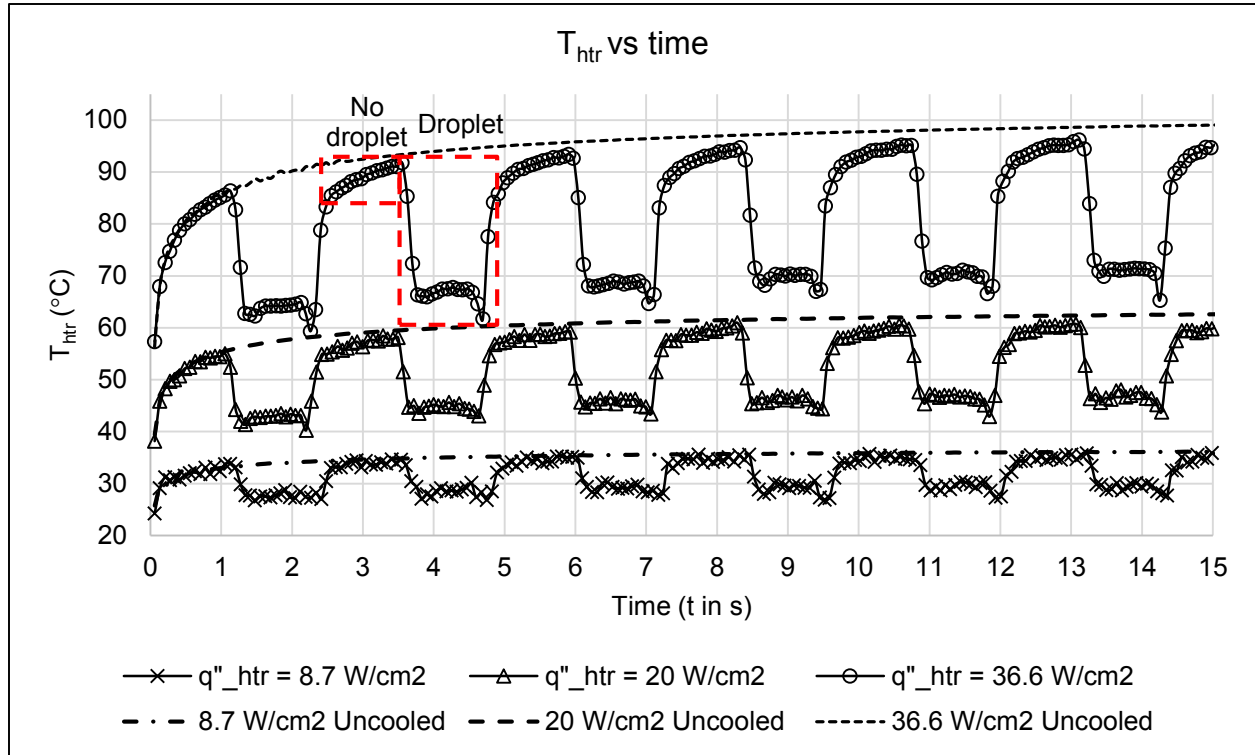
Figure 3-14 Results of T_{htr} vs time for 6 droplets of DI water moved over hotspot.

3.3 Results – Hotspot Cooling with DI Water using ITO RTD

3.3.1 Experimental Results

Figure 3-14 shows cooling curves of six droplets for three levels of heat flux provided to the heater. As each droplet moved across, a fall and a subsequent rise in temperature was observed. Each fall and rise corresponds to one cycle of a single liquid droplet cooling. Phase-change was also strong as apparent from the condensate formation and enhanced heat transfer from the hotspot to the droplet, thereby lowering the temperature. Upon closer inspection, as shown in Figure 3-14, we saw some interesting dips when the droplet entered the hotspot. When the meniscus enters the hotspot, the temperature reduces little more than that when it dwells on the hotspot. Upon exit, this effect is magnified as the temperature drops further. This was attributed to a repeated effect in all cooling cycles to the enhanced heat transfer due to enhanced phase-change at the menisci. Thermocapillary induced Marangoni convection was also observed to be responsible for the enhanced T_{htr} drop at the menisci of the droplet and has been studied in section 4.4.4.

3.4 Observations

The droplet motion over the hotspot was divided into three phases - the entry, dwell and the exit phase. During the entry phase, T_{htr} value fell and appeared to have a dip before rising up to a steady value signifying the end of the entry phase after 250 ms. During the dwell phase, the droplet remained on the hotspot for 1.25 s and T_{htr} was maintained at a steady value. At the exit, the value of T_{htr} dropped again to a larger dip and then rose back to the initial value before entry of the droplet. The heat transfer during the entry phase was credited to conduction, convection and phase-change within the advancing meniscus of the drop.
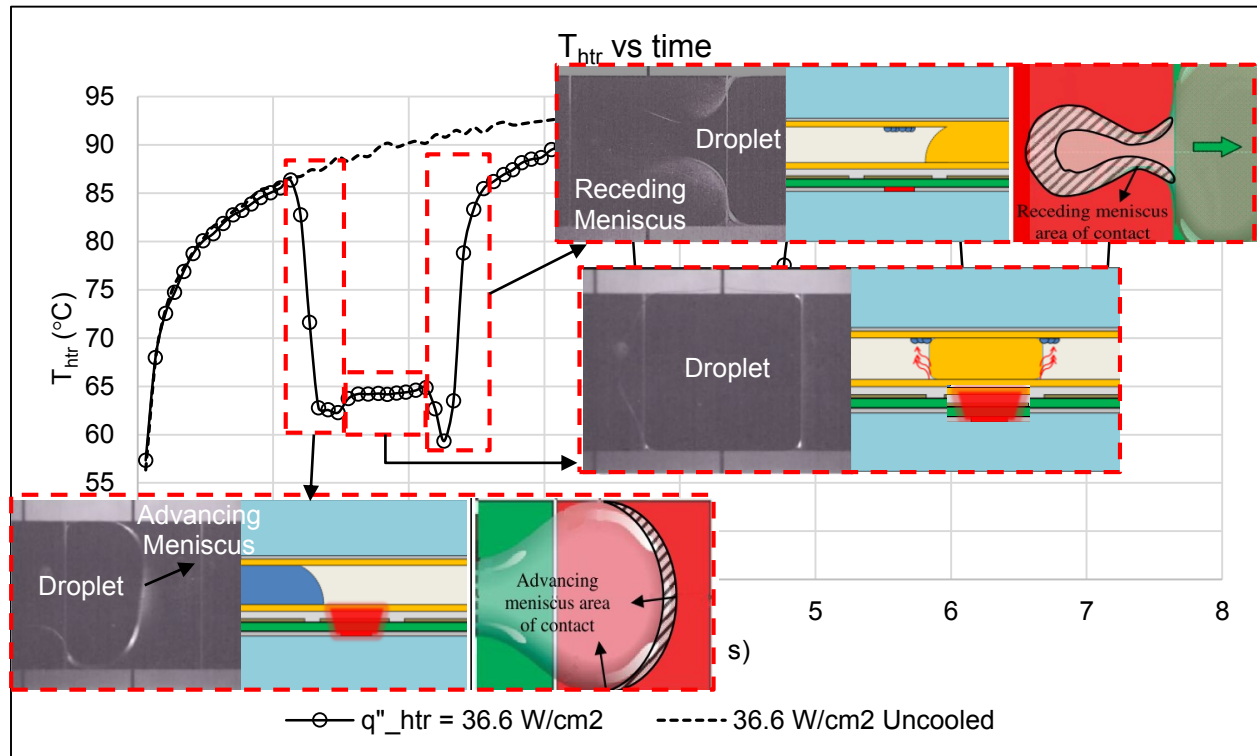
Figure 3-15 View of the EWOD device with pictorial demonstration of phase-change at the meniscus. The vapor then condenses on the under-side of the top-chip.

During the entry and exit phases, referring to Figure 3-15, condensation was seen in the top view of the experiment snapshot. This was due to the evaporation of the advancing meniscus causing latent heat to be removed from the heater causing its temperature to drop. As the drop starts to dwell, it coalesces

47

with the condensate and covers the entire hotspot in which the heat transfer is primarily due to conduction. At the exit, the receding meniscus over the heater contributed to phase-change enhanced cooling and caused T_{htr} to drop again. The drop was larger than the one at the entry due to the fact that the receding meniscus tail was larger in length and had more contact area with the hotspot which facilitated more evaporation (Figure 3-15). Table 3-2 summarizes the results of temperature drop for three different heat flux levels including the phase-change effects. The heat transfer enhancement with phase-change was identified and studied in detail in CHAPTER 4.

Table 3-2 Summary of temperature drop observed for three heat flux levels.

Temperature drop	$q"_{htr} = 8.7$ W/cm²	$q"_{htr} = 20$ W/cm²	$q"_{htr} = 36.6$ W/cm²
ΔT_{htr} (°C)	7	15	25
ΔT_{htr} (°C) at entry/exit (max.)	9/10	17/19	28/32

3.5 Conclusions

In this chapter, RTDs were used to achieve hotspot cooling by droplet motion with EWOD DMF. ITO was used as a material of choice to emulate the hotspots at three levels of heat flux and sense the temperature using calibration data. Experiments were conducted for multiple droplets using DI water which showed phase-change for the entry, dwell and exit phases of drop motion. This effect lowered the temperature of the heater by 3 °C at the entry and 7 °C at exit for the highest heat flux level.

CHAPTER 4

STUDY OF EWOD DMF COOLING

4.1 <u>Motivations</u>

In the previous chapters, the experimental results with hotspot cooling using IL and DI water were presented. Of them all, DI water showed enhanced heat transfer due to better conduction, convection and an additional phase-change modes which helped in lowering heater temperature for three heat flux levels. In order to study these effects in detail, a hydrophilic-spot (H-spot) was patterned just over the heater area (Figure 4-1) and droplet motion was observed in detail in this region to achieve the following objectives:

1.   To achieve steady-state heating. The chip design was revised by reducing dimensions and lowering the thermal mass seen by the heater and incorporating additional RTDs.
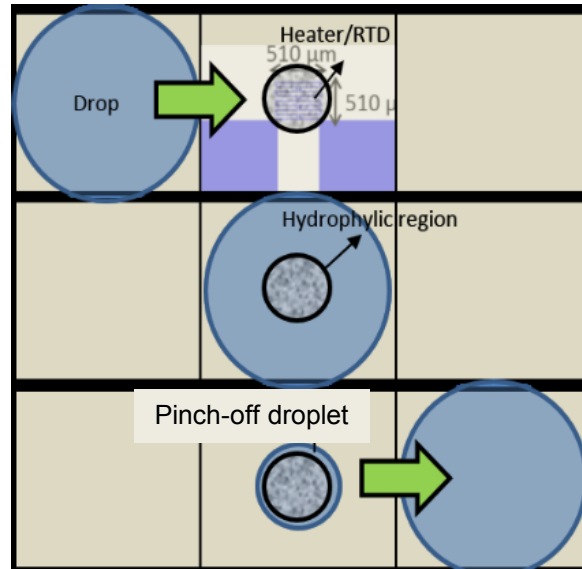
Figure 4-1 Concept of hotspot cooling study using hydrophilic spot (H-spot) on heater.

2.   To pinch-off a droplet on the H-spot (Figure 4-1) during exit phase to maintain T_{htr} and delay dry-out. Teflon lift-off process was characterized to achieve the H-spot fabrication on heater.

3.   To observe and analyze the combined conduction, convection and phase-change heat transfer modes until dry-out. High-speed motion of the advancing and receding meniscus

in the entry and dwell phases of the droplet was analyzed along with RTD data. Alumina (Al_2O_3) μ-particles were also used to observe Marangoni convection flow in the menisci.

4. To estimate the overall heat transfer coefficient, $h_{ov,meas}$ for the three heat transfer modes using synchronized data analysis of high-speed video and RTD data.

5. Perform numerical analysis using COMSOL by parameterizing thermal diffusivity of coolant droplet, α_{fluid}. The effect of varying droplets on T_{htr} was seen including phase-change emulation using meniscus edge B.C. This provided a roadmap for choosing coolants with specific tailored properties for high heat flux cooling applications.

6. To validate the evaporation rate in the experiments, $Q_{evap,meas}$ to the values used in COMSOL simulations, $Q_{evap,sim}$.

7. To propose droplet pinch-off concept to multiple drops cooling by continuously pinching-off droplets on H-spot followed by the incoming droplet merging with the pinched-off one – this delays dry-out even further and allows consistent temperature regulation of the hotspot.

4.2 Revised ITO RTD Hotspot Cooling setup

Although the previous ITO RTD (section 3.2) setup was used to demonstrate hotspot cooling, the design was later scrapped and a new chip holder was fabricated which addressed thermal and practical issues. As shown in Figure 4-2 (a), by reducing the real estate of the device from a 4 inch wafer to a square substrate of 40 mm x 40 mm dimensions, the thermal mass was reduced and steady-state heating was easy to reach. This also improved insulation to certain boundaries of chip and facilitated better experimental control. The design of the EWOD electrodes moved from a multiple size layout to a fixed size one to accommodate the change in real estate. By doing this, the yield per wafer improved from one device to two devices with additional room at top and bottom halves of the wafer. As we had a fixed electrode layout, the number of reservoirs was fixed at two, one for inlet and the other for exit. For the heater/RTD design in Figure 4-2 (b), the total number of RTDs used was limited to two for the reservoirs and one at the heater with two additional RTDs, one before the heater electrode and the after.
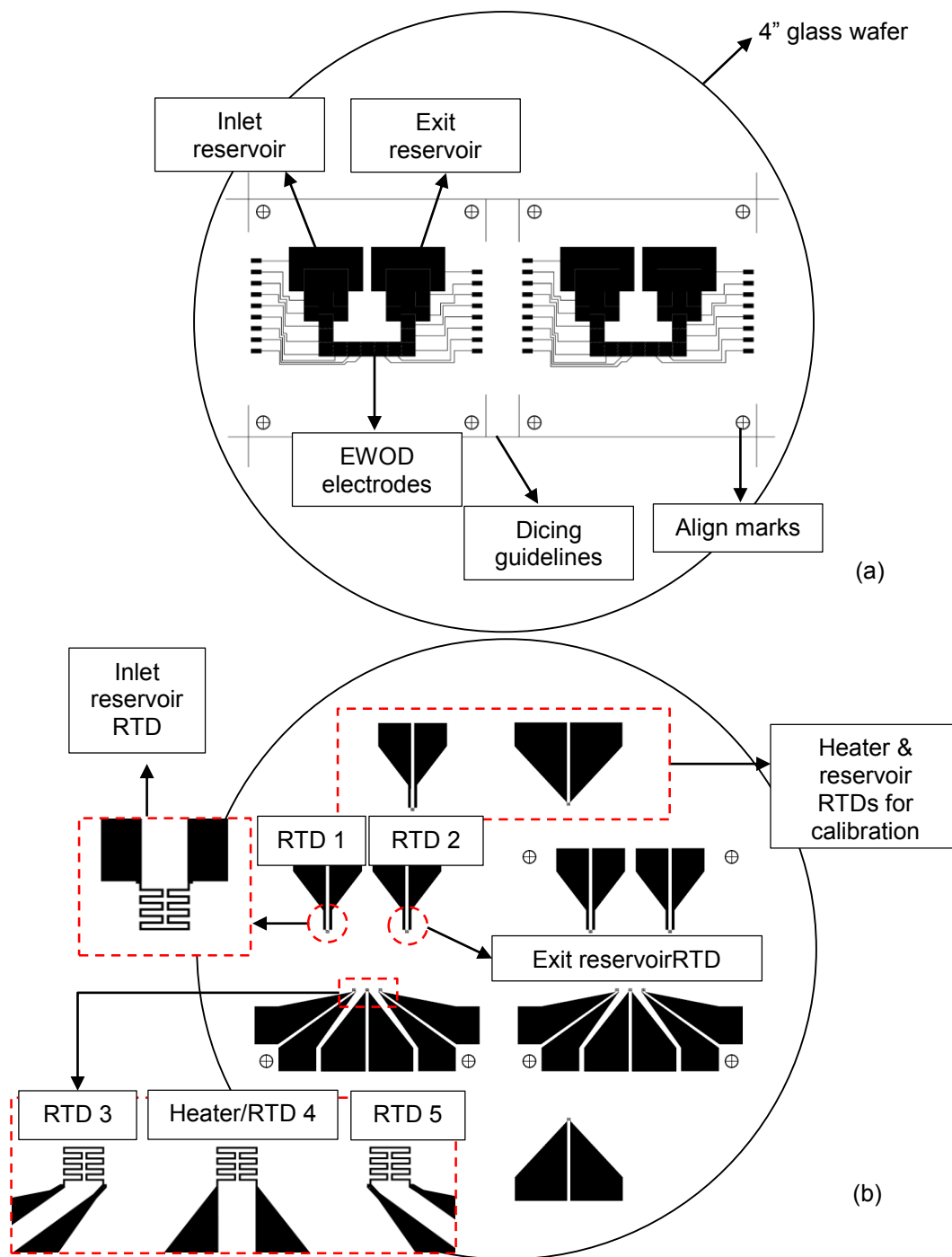
Figure 4-2 Photolithography mask with two sets of EWOD electrodes patterned for a 4 inch wafer.
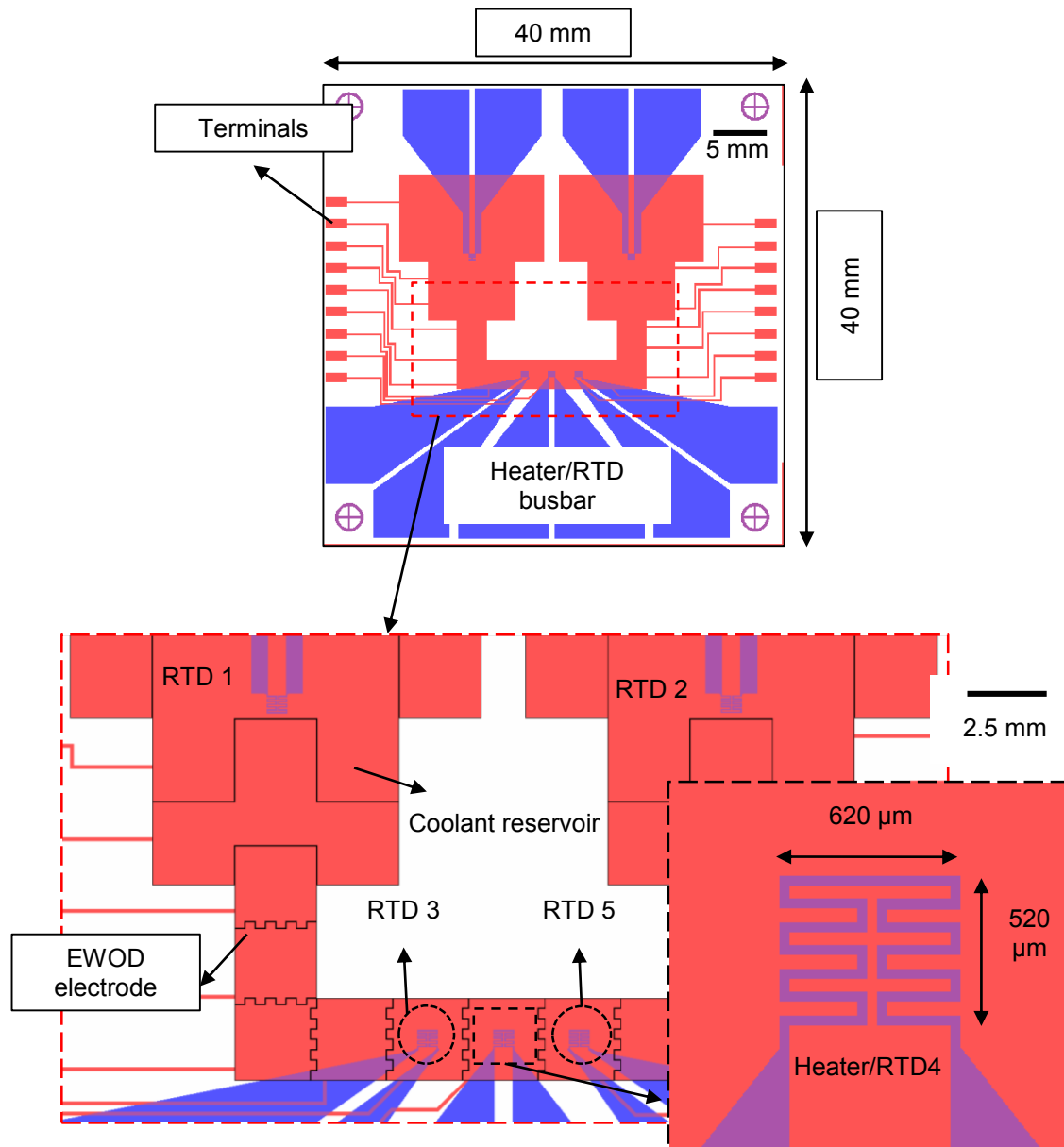
Figure 4-3 Figure showing the heater/RTD and EWOD photolithography masks aligned.

The superimposed masks in Figure 4-3 shows the final layout of the device. The calibration curve for the RTDs as shown in Figure 4-4 was conducted using the same calibration system as before. One advantage of using multiple duplicates of RTDs on a wafer is so that one can check for consistency of the calibration of the RTDs across ITO coated substrates as the resistivity of the film may not be the same due

to little knowledge of the similarities between the parameters involved in ITO film deposition on every wafer. As shown, the RTDs exhibited consistent linearity amongst two trials for the ITO coated substrate chosen
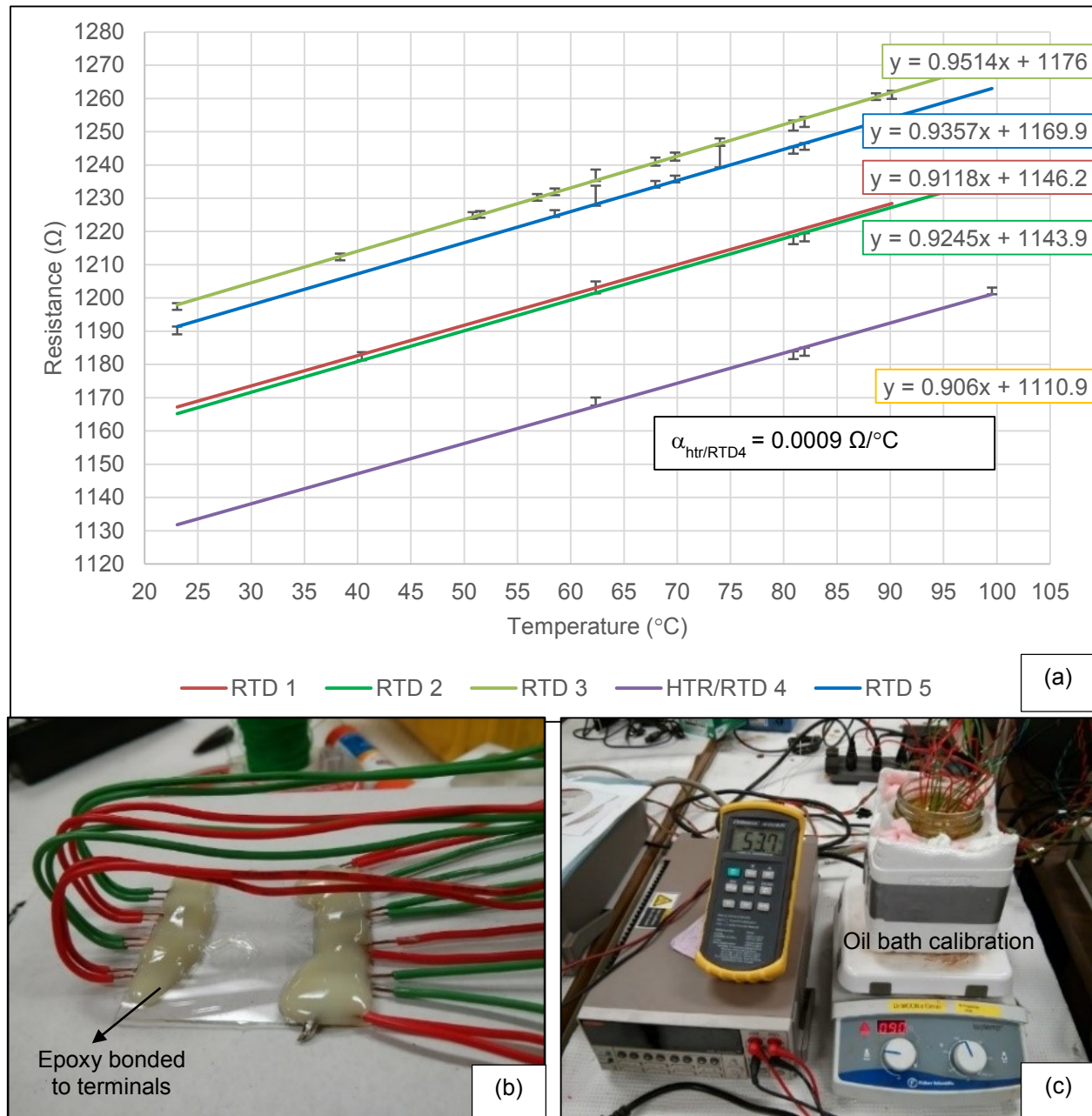
Figure 4-4 Calibration data for revised ITO RTD design (a) with epoxy bonded terminals (b) for better accuracy in an oil bath setup (c) similar to the previous calibration setup.
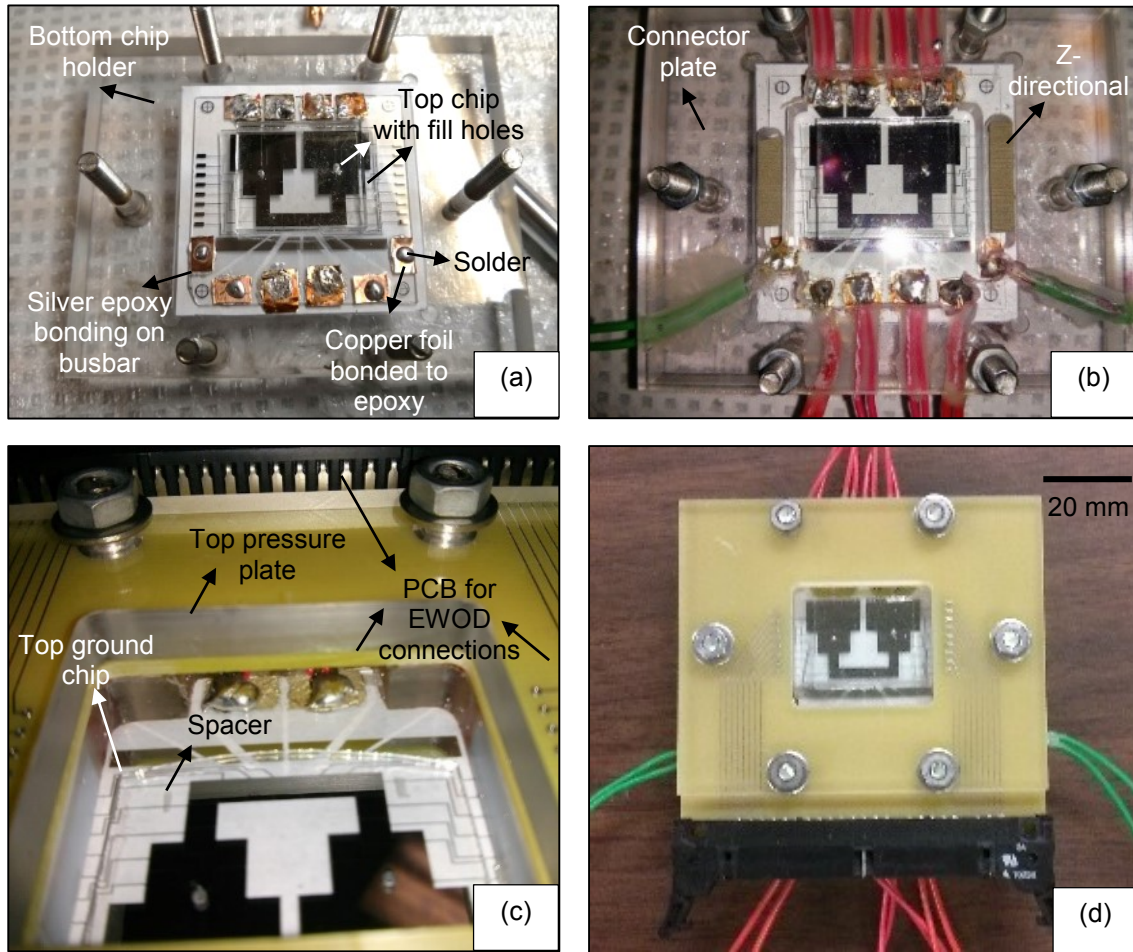
Figure 4-5 Figure showing the revised design setup.

for the device fabrication. Figure 4-5 shows the revised design setup with the bottom chip holder and connector plate (Figure 4-5 (a), Figure 4-5 (b)). The connections to the busbars were provided by the silver epoxy/copper foil combination. The revised setup showing top and bottom chip after assembly with the PCB interfaced with the DAQ and control PC.

4.3 H-spot Fabrication on Heater/RTD

As shown in Figure 4-6, a hydrophilic spot was fabricated on the heater using Teflon lift-off process (Figure 4-7) with help of conventional clean room semiconductor fabrication tools. In addition to the steps described in section 3.2.3, a thick layer of PR was spin coated on SU-8 followed by exposure and aligning
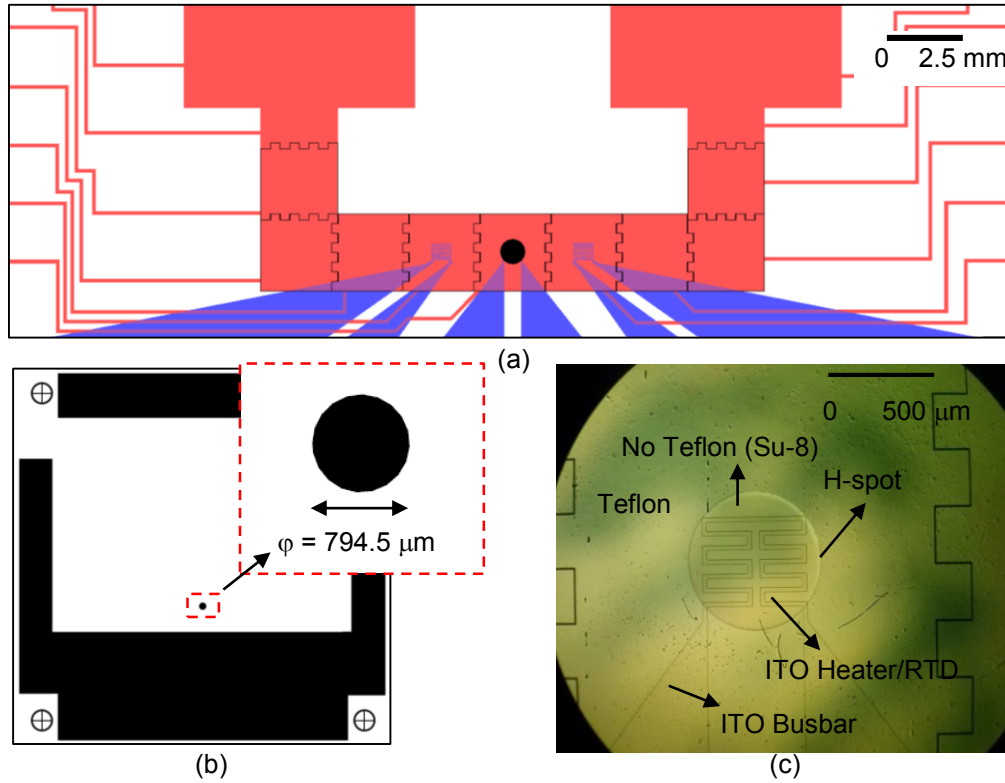
Figure 4-6 Concept of cooling study experiment using H-spot on hotspot electrode (a) of 794.5 µm

diameter (b). Final bottom chip with H-spot fabricated on heater (c).

step using the mask in Figure 4-6 (b). After developing, a PR pillar of 794.5 µm diameter was checked for

its accuracy in position directly above the ITO heater/RTD. The hard bake step was skipped and a flood

exposure was performed to weaken the pillar. The next step involved spinning Teflon solution followed by

hard bake to evaporate the solvent. Lastly, the Teflon over the heater was lifted-off in Acetone solution and

the device was rinsed in DI water. The fabricated device with the H-spot is shown in Figure 4-6 (c) where

the region inside the circle represents the uncoated Teflon part in which the SU-8 was directly exposed to

DI water.

After the device (bottom chip) with the H-spot patterned on the heater area was fabricated, it was

inserted in the cooling system and connected in the same way as discussed in the experimental section of

3.2.6. The reservoir was filled with DI water and a droplet was generated and moved across the hotspot
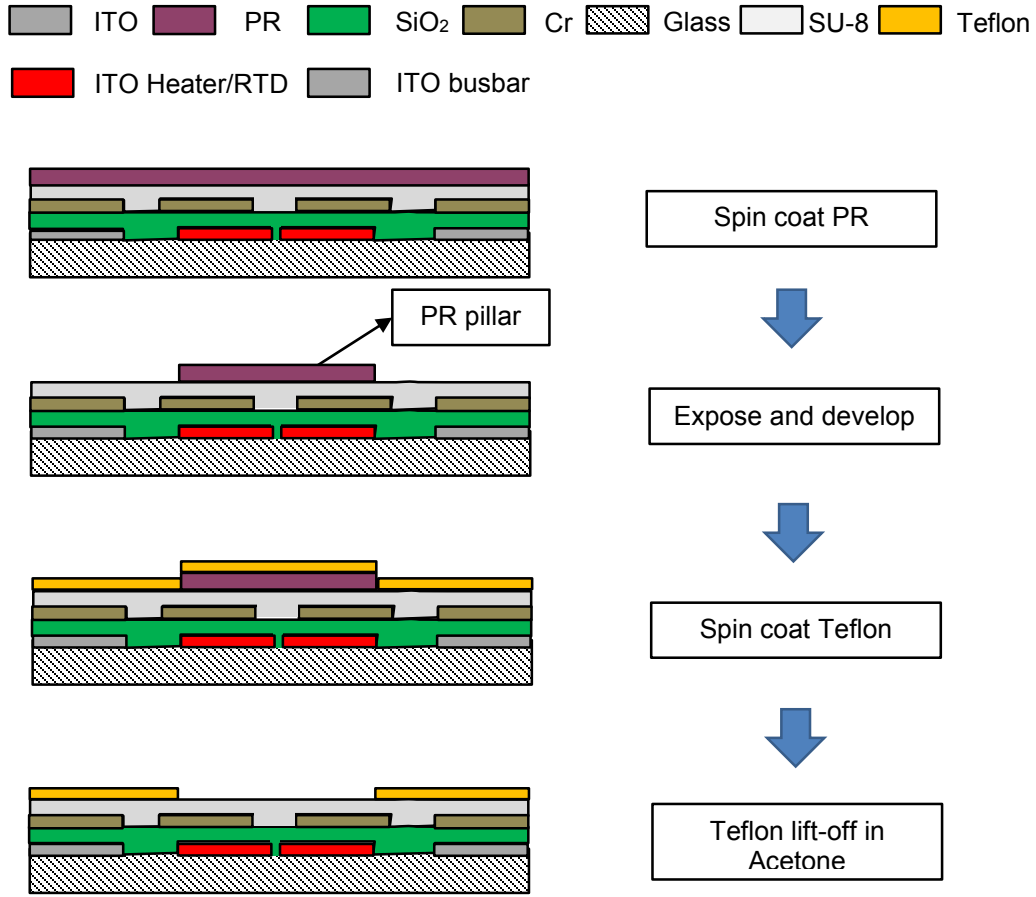
Figure 4-7 Fabrication steps involved for patterning H-spot using Teflon lift-off.

after the heater reached steady-state. Based on the observation of the motion under the high speed camera

of the droplet across the H-spot, the phases of drop motion were studied in detail.

4.4 Results – Droplet Motion Analysis

Upon close inspection and correlating the high-speed camera images with the RTD data, the

various phases of droplet motion over the hotspot were identified. As shown in Figure 4-8, the entry phase

of the droplet is characterized by the drop in T_{htr} represented by the black arrow (Entry_EWOD-ON). As

the electrode was directly over the RTD (separated by passivation), the high EWOD voltage induced noise

in the RTD reading. The next phase (Dwell_EWOD-OFF) is shown by the blue arrow which involved the

droplet staying on the hotspot electrode while the EWOD voltage was turned OFF.
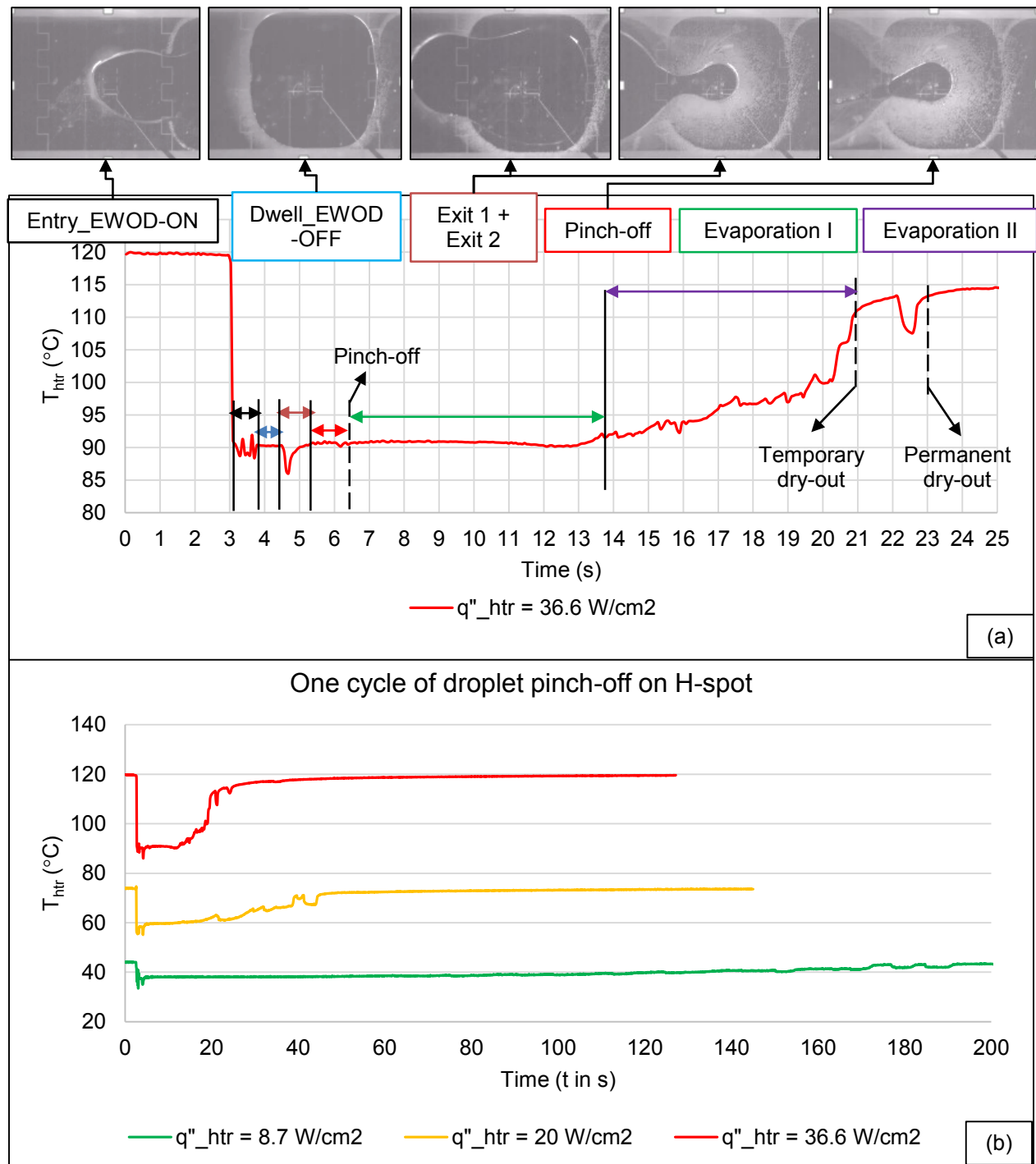
Figure 4-8 Droplet motion analysis over H-spot with various phases for 36.6 W/cm² (a). The same phases were observed for other heat flux levels as well (b).

Following the dwell phase, the droplet starts to exit from the hotspot electrode (maroon arrow) onto the next electrode. Exit 1 was characterized by a drop in T_{htr} momentarily after which Exit 2 involved T_{htr} to rise back to the dwell phase value. At the end of Exit 2, a receding tail meniscus was formed around the H-spot. When the droplet starts to move away onto the next electrode, a small droplet stays back on the H-spot after pinching off from the main droplet. Following droplet pinch-off, evaporation phases kick-in until a temporary and a permanent dry-out. All these phases were observed for other heat flux levels as well (Figure 4-8 (b)) but analysis was done only for 36.6 W/cm² in detail using high-speed video and RTD data in the following sections.
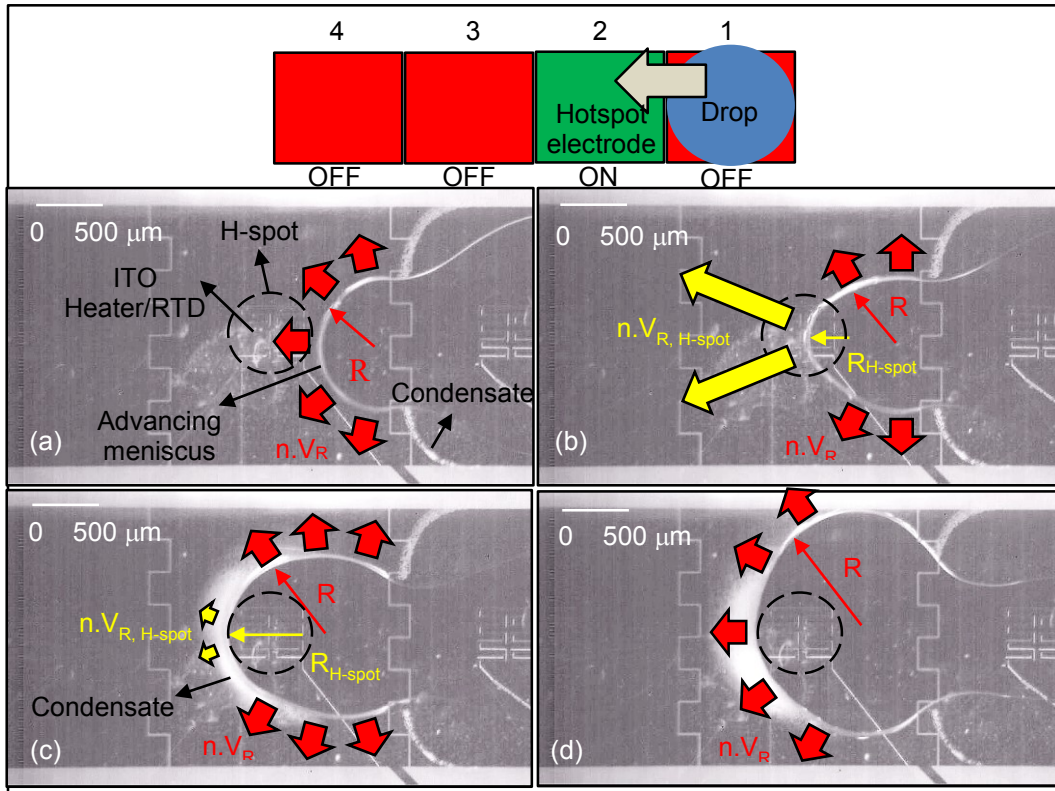
Figure 4-9 Analysis of droplet entry phase for 36.6 W/cm². The observations made were same for all heat flux except that the amount of evaporation varied.

4.4.1 Entry Phase

When the droplet began to move into the hotspot electrode, the entire advancing meniscus attained a radius of curvature R and entered the hotspot with a normal velocity $n.V_R$ as shown in Figure 4-9 (a). As

soon as the tip of the advancing meniscus entered the H-spot in Figure 4-9 (b), the portion of the meniscus only on the H-spot attained a curvature R_{H-spot} and spread with a faster velocity $n.V_{R,H-spot}$ due to enhanced wetting provided by the H-spot. As the meniscus approached the end of the H-spot's circumference in Figure 4-9 (c), the value of $n.V_R$ decreased and the radius R_{H-spot} also approached the rest of the meniscus' radius R. The last step of the entry phase ended in the entire meniscus spreading at the same velocity $n.V_R$ until the droplet filled the hotspot electrode in Figure 4-9 (d). The data in Figure 4-10 shows the entry phase of the drop after steady-state heating which includes the noise in the T_{htr} data while the hotspot electrode was ON.
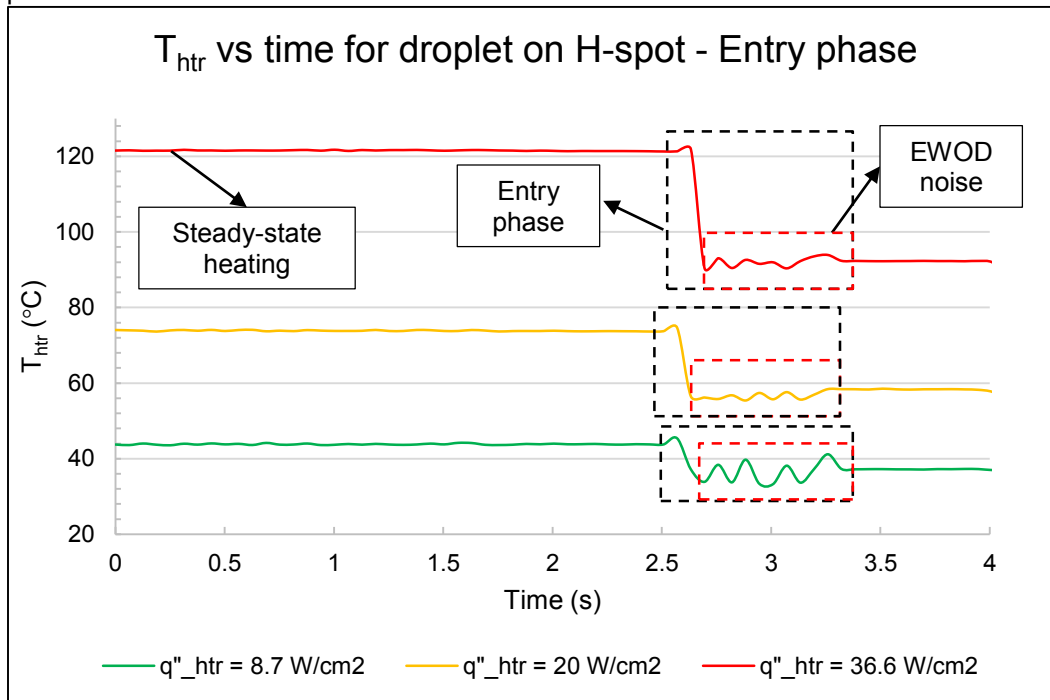
Figure 4-10 Analysis of experimental data of droplet entry phase for three heat flux levels.

Even with the H-spot in this case and the above observations made, the drop in temperature was similar to the results with DI water in section 3.3.1. Moreover, the dips at the entry phase were not discernable from the EWOD noise so it could not be inferred if the H-spot played any role in enhancing heat transfer during entry of droplet. This could be due to steady-state heating playing a role in minimizing sensitivity of droplet entry effects when compared to transient heating for the results in section 3.3.1.

q"_htr = 36.6 W/cm^2

q"_htr = 20 W/cm^2

q"_htr = 8.7 W/cm^2
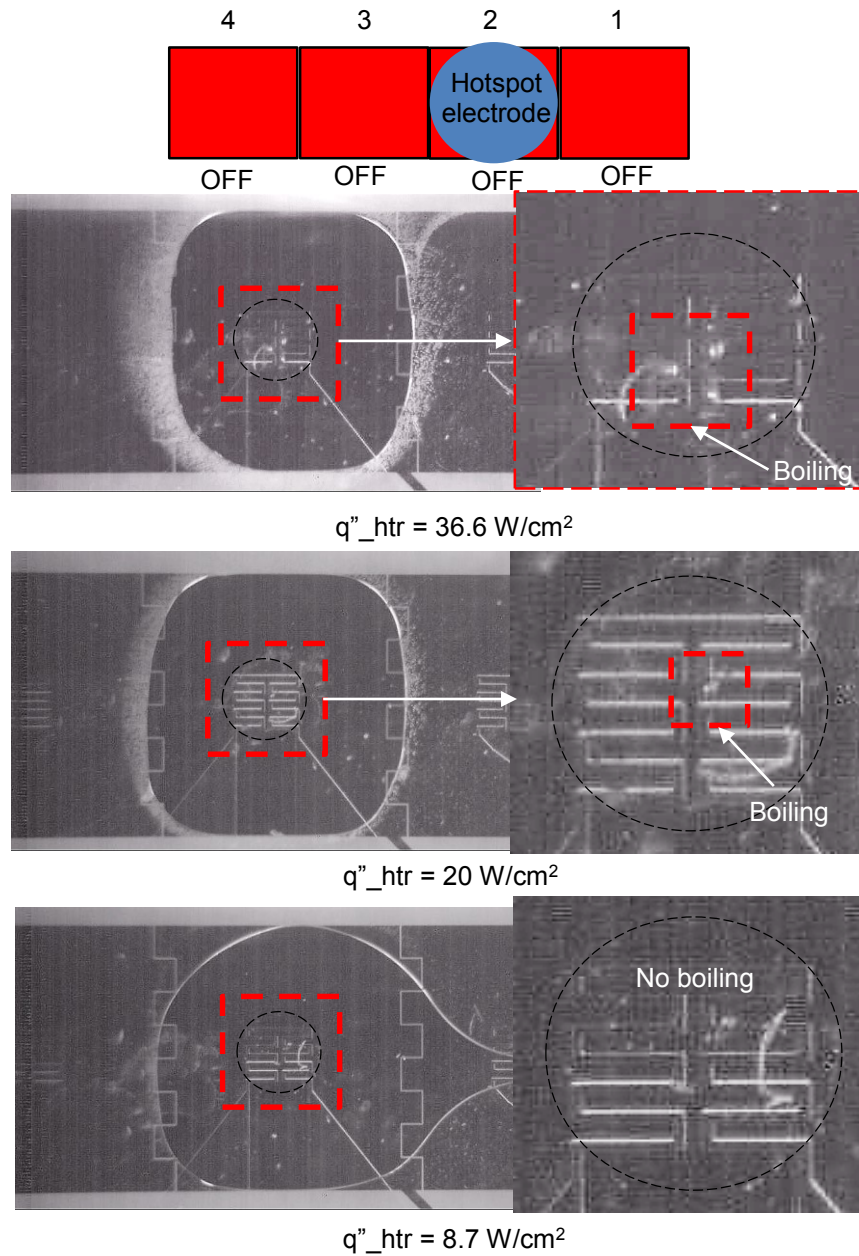
Figure 4-11 Analysis of droplet dwell phase for three heat flux levels (snapshot at end of dwell phase).

Onset of meniscus evaporation is different for all heat flux cases.

4.4.2 Dwell Phase

During the dwell phase of the drop, the heat was transferred from the hotspot initially through conduction. Depending on the input heat flux level, the temperature of the meniscus rose soon and then
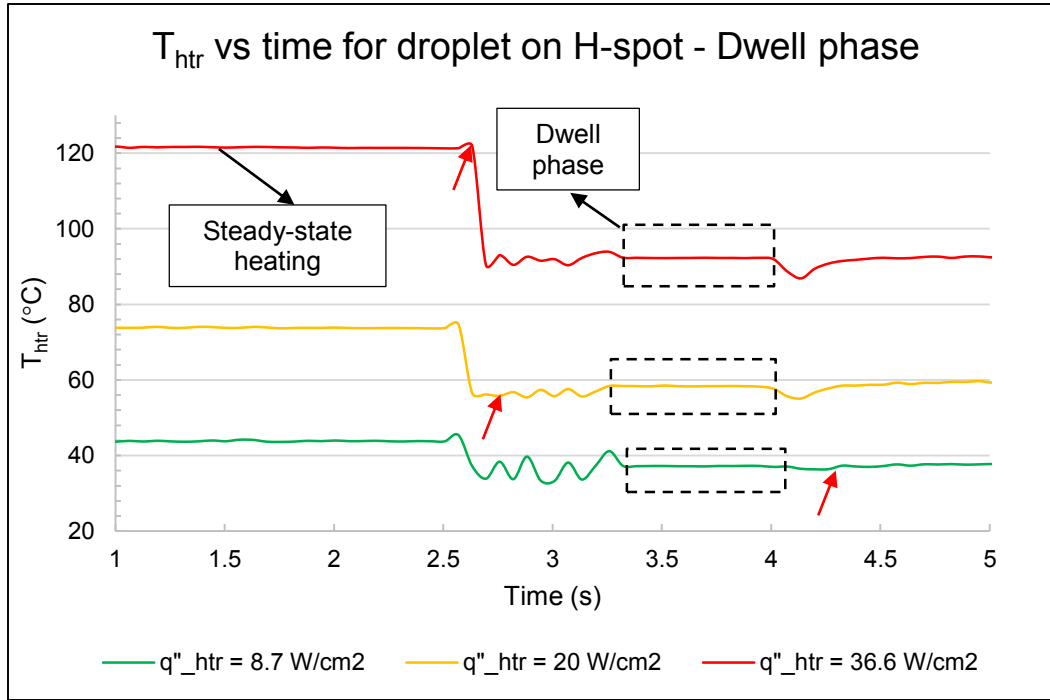
Figure 4-12 Analysis of experimental data of droplet dwell phase for three heat flux levels. Red arrow represents start of condensation around meniscus.

phase-change took place uniformly around the meniscus for the rest of the dwell phase. Figure 4-11 shows the final stage of the dwell phase. Upon closer inspection, boiling phenomena was observed clearly on the H-spot only for 36.6 W/cm^2 heat flux. From the RTD data as shown in Figure 4-12, the dashed box represents the dwell phase. As the droplet entered this phase, the heat transfer from the hotspot to the liquid was primarily by conduction and some amount of buoyancy driven convection within the liquid. The red arrow indicates the point in the T_{htr} trend that condensation was seen around the meniscus of the droplet from the high-speed video analysis which indicated that the convection and conduction modes have reached maximum rate and droplet temperatures reach saturation value for phase-change heat transfer to take over the hotspot cooling process. Note that for 36.6 W/cm^2 heat flux, the phase-change was seen as the droplet entered the hotspot electrode while the 8.7 W/cm^2 case showed delayed onset of phase-change after the dwell phase.

4.4.3 Exit Phase

The exit phase was divided into two sub-phases namely exit (phase) 1 and 2. Exit 1 was a temporary phase which pertained to enhanced cooling due to recirculation of fluid over hotspot and exit 2
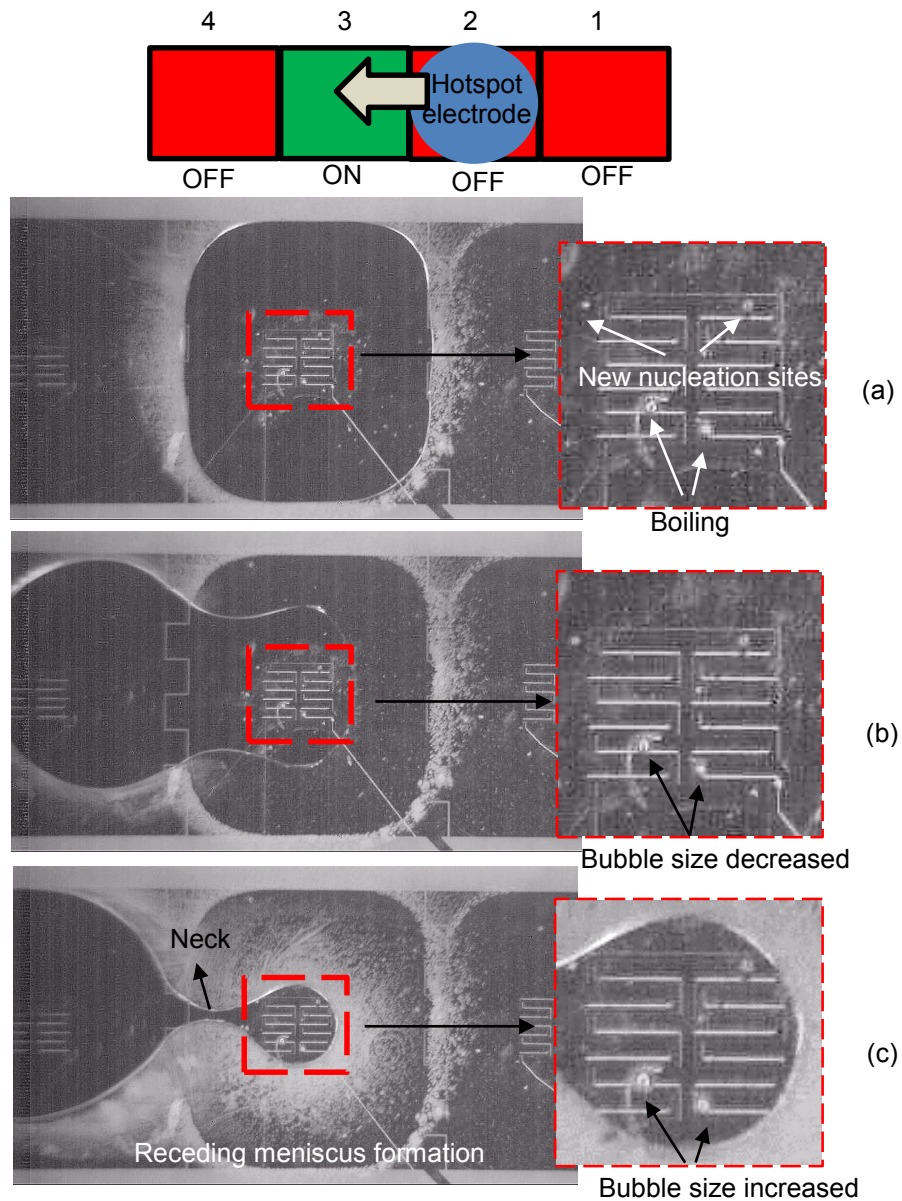
Figure 4-13 Analysis of droplet exit phase for 36.6 W/cm^2 heat flux. Exit 1 phase began (a) with nucleation sites around H-spot and ended (b) with a decrease in bubble size. Exit 2 began after exit 1 and ended (c) with an increase in bubble size.

ended in a receding meniscus tail formation. The exit phase began as soon as the electrode 3 was actuated in Figure 4-13 (a). When the drop began to exit and as it moved around the H-spot, the fluid began to recirculate due to EWOD rolling motion [28] bringing in the cooler fluid away from the H-spot to replace the heated fluid close to it. This reduced the T_{htr} temporarily (Figure 4-14) and was designated as the end of exit phase 1 region in the RTD data as shown in Figure 4-13 (b). This effect was also confirmed by the reduction in bubble size in the high-speed video.
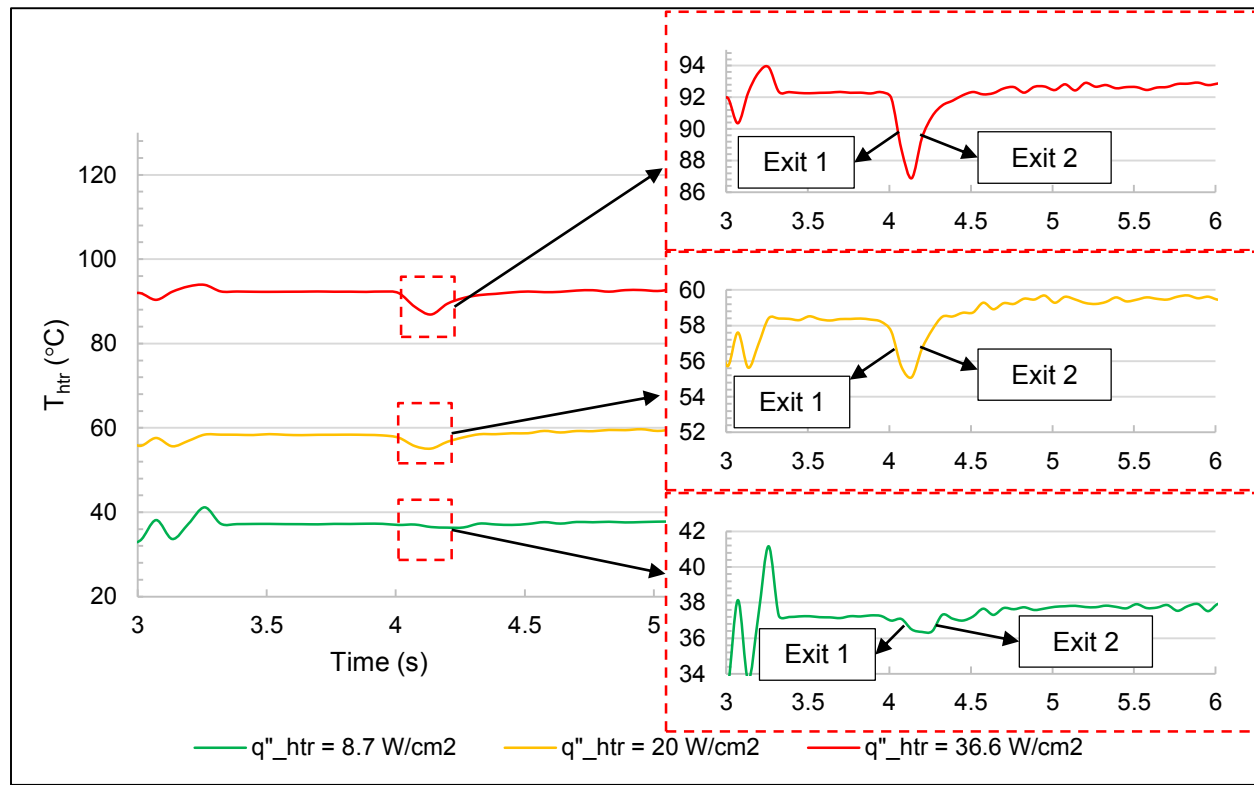
Figure 4-14 Analysis of experimental data of droplet exit phases.

The initial reduction in bubble size followed an increase in the size in exit 2 (Figure 4-13 (c)) in which the value of T_{htr} also rose and went back to the one before the start of exit 1. At the end of this phase (exit 2), the droplet formed a receding meniscus and was held in place by the H-spot and the bubble size had also increased further. Moreover, the droplet showed more signs of boiling on the surface as new nucleation sites emerged. Evaporation was also strong around the receding meniscus and it was also

observed that the drop in T_{htr} was the maximum for 36.6 W/cm^2 as the spatial temperature gradient in the main droplet was higher.

4.4.4 Marangoni Convection Effects at Entry/Dwell Phase

At the entry and exit regions of the meniscus, apart from phase-change, the dips in the temperature was also credited to Marangoni convection. The enhanced convection effects at the meniscus region of a liquid due to temperature differences was first identified by Pearson [29] in 1958. The thermocapillary [30] effect introduced also changes the surface tension of the meniscus which is characterized by the Marangoni number (M_a) introduced by Pearson as

$$M_a = \frac{d\gamma}{dT} \frac{L\Delta T}{\eta \propto}$$

(4-1)

where,

γ is the s

L is the characteristic length

ΔT is the temperature difference

η is the dynamic viscosity

$\propto$ is the thermal diffusivity

In our case, the temperature variation along an interface was the result of local heating which induced non-uniformities in evaporation. When Alumina (Al_2O_3) particles (average particle size of 4.5 – 7 µm) were added in the liquid and the droplet was sandwiched between the top and bottom devices, the convective patterns in the bulk liquid around the heater were observed. As shown in Figure 4-15, the droplet was placed in such a way that the advancing meniscus was directly over the heater. The particle motion was observed for three levels of heat flux and the results were presented in this analysis. Two symmetrical vortices along a horizontal centerline through the droplet was observed with the particles headed towards

the advancing meniscus. Although the flow profile looks complex, an attempt was made to understand the convection patterns using high-speed camera snapshots with arrows overlaid to denote flow profile.
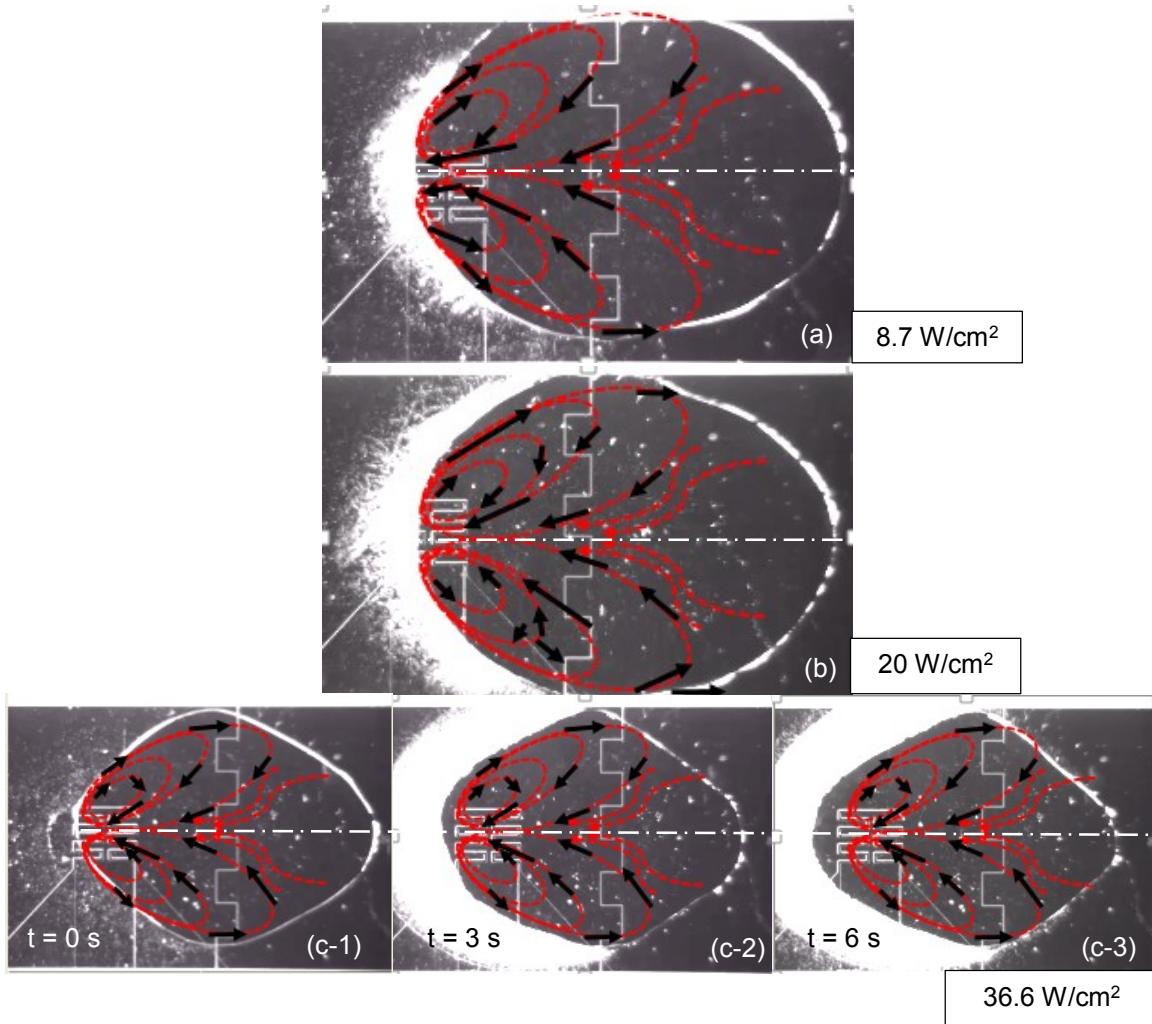
Figure 4-15 Alumina (Al_2O_3) particles suspended in a DI water droplet showing vortex formations at the advancing meniscus region due to thermocapillary induced Marangoni convection. Thermocapillary pumping was observed for 36.6 W/cm^2 case ((c-1) to (c-3)).

The temperature gradient produced due to the non-uniform heating of the meniscus by the heater was found to be the cause for the flow pattern. When the heater was turned ON, the particles near the heater moved in a circulatory motion from the receding meniscus bulk fluid along the centerline towards the

advancing meniscus and formed two counter-rotating symmetric vortices. A similar vortex was reported for a convex (similar to hydrophobic) meniscus in [31]. Due to this, there was an intensive evaporation effect at the meniscus film over the heater as seen from the above figure. Upon closer inspection of the convection patterns, it was observed that as soon as the heater was turned ON, the particles closer to the center of each vortex point towards the highest surface tension region in the advancing meniscus (near the top-chip and around the meniscus line surrounding the advancing meniscus) and the ones further away detach from the vortex and join in the rear fluid (bulk) motion towards the heater to replace the hot fluid. In other words, the convective pattern was a net result of the particles in the vortices due to thermocapillary effect and the advection of the heat by the motion of the heated fluid away from the heater to circulate the colder fluid towards it. It was also noticed that the vortices seemed to diminish as the surface tension gradient decreased (entire droplet was reaching equilibrium temperature) and at a certain instant, no more flow patterns were observed. At this point, it was concluded that $\frac{d\gamma}{dT}$ goes to zero and M_a equals zero.

4.4.5 Droplet on H-spot – Pinch-off

When the electrode 4 was actuated, the droplet pinched-off at the neck region (Figure 4-16 (a), (b)) forming a small droplet on the H-spot and few trace droplets along the meniscus neck area. This was referred to Rayleigh instability [32] which governs droplet breakup patterns based on small perturbation of a wavelength that can amplify the disturbance exponentially over time and sinusoidal with space. A thorough experimental and numerical explanation can be found in [33]. The pinched-off drop on the H-spot showed new nucleation sites emerging on the surface. As the temperature of the fluid around the heater area continued to rise from the beginning of the dwell phase, the nucleation sites continued to grow and the bubbles got larger over time. Figure 4-18 shows the results for T_{htr} when the droplet moved over hotspot and pinched-off a small droplet on the H-spot. The dark arrows represents the point in time when the droplet on the H-spot evaporated completely and dry-out was reached. After dry-out, T_{htr} went back to its initial steady-state value prior to droplet cooling.
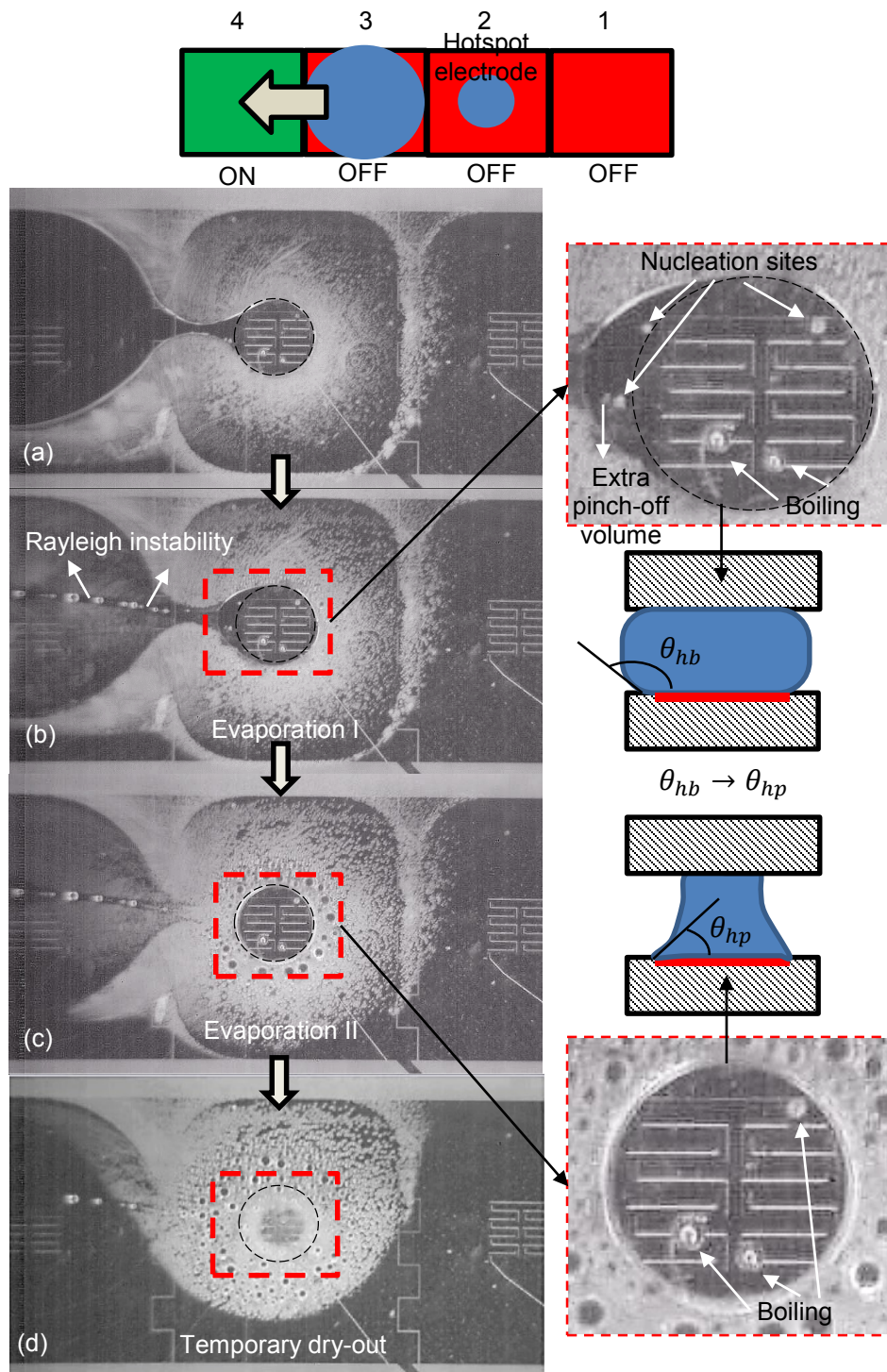
Figure 4-16 Analysis of droplet after pinch-off showing different stages of evaporation.
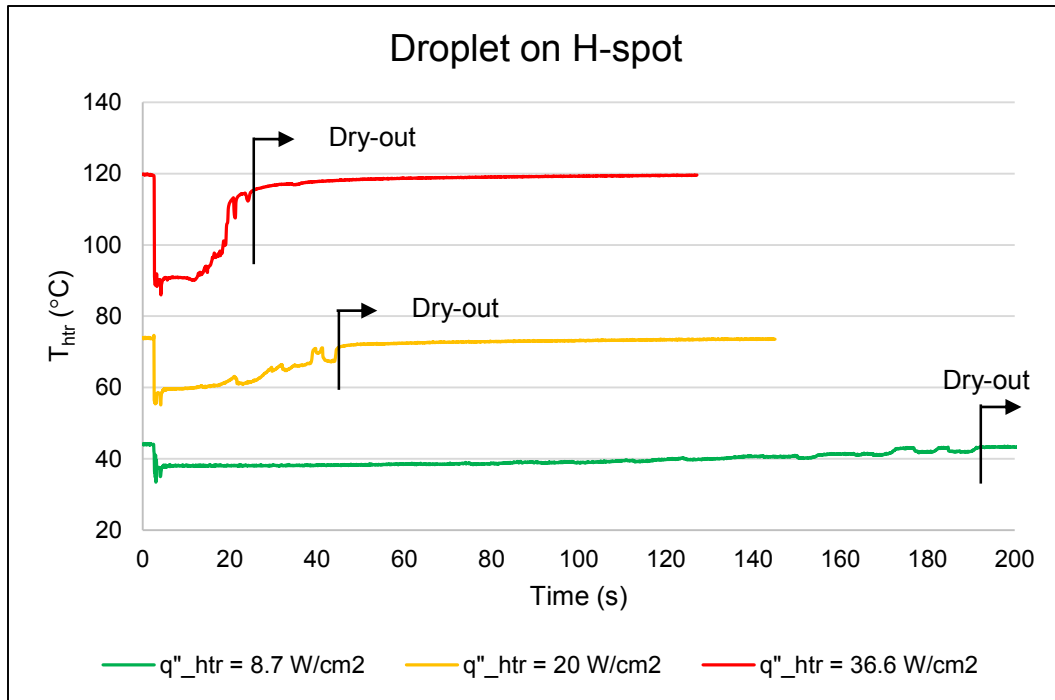
Figure 4-17 RTD data of hotspot with droplet on H-spot.
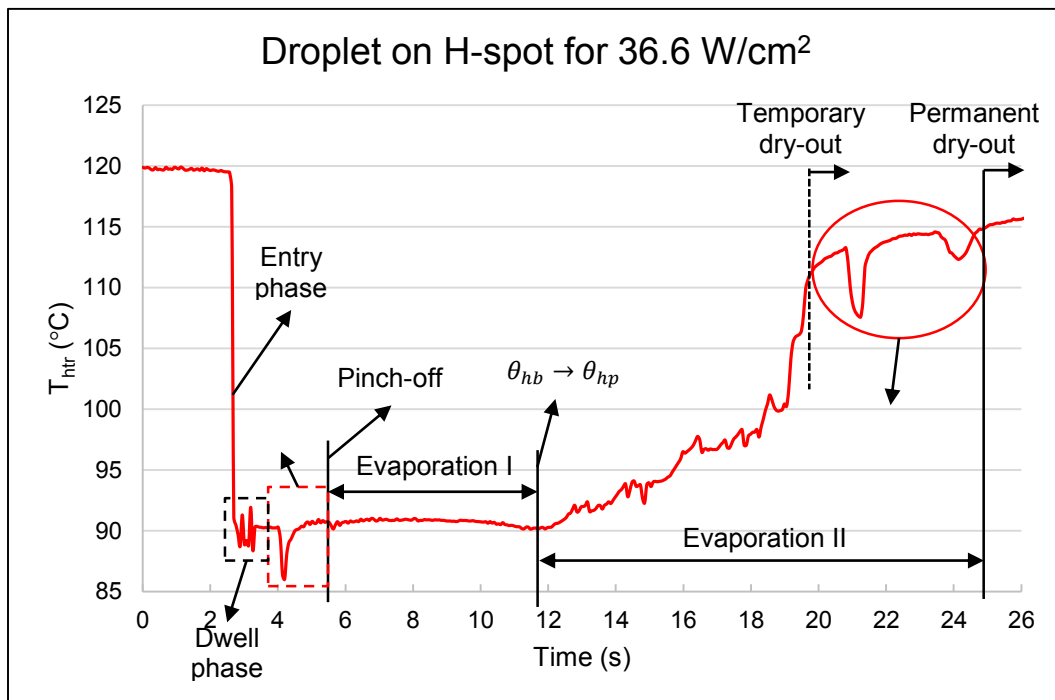
Figure 4-18 RTD data showing evaporation zones after pinch-off for 36.6 W/cm^2.

4.4.6 Droplet on H-spot – Evaporation I Zone

As shown in Figure 4-17, the time for the onset of dry-out depended on the volume of droplet pinched-off on the H-spot and the input heat flux level. Upon closer examination of the temperature data and the high-speed video after pinch-off, the trend of T_{htr} was divided into various evaporation zones post pinch-off. The evaporation I zone started from the point where the pinch-off occurred on the H-spot as shown in Figure 4-16 (b) and was only observed for the case when the pinched-off volume was slightly larger than the H-spot size. The contact area of the droplet covered the entire heating element area and the excess volume pinched-off on the H-spot continued to evaporate with one half of the droplet meniscus pinned to the H-spot. A detailed look at Figure 4-18 for the 36.6 W/cm² case showed that the T_{htr} value remained almost constant in this zone until the contact area of the droplet equaled that of the H-spot.

According to a paper by Ahmadi et al., [34] which talks about droplet evaporation on hydrophobic and hydrophilic surfaces in an enclosed microchannel, it was experimentally demonstrated that the contact angle during droplet evaporation remained constant over time irrespective of the surface. Based on this result, ignoring surface tension gradient around the H-spot droplet meniscus, it was considered that the angle remained constant in evaporation zone I. When the droplet's contact area equaled that of the H-spot, the angle changed from hydrophobic to hydrophilic and the meniscus thickened as shown in Figure 4-16 (c), signifying the start of evaporation zone II.

4.4.7 Droplet on H-spot – Evaporation II Zone

This zone comprised a steady rise in T_{htr} until the temporary dry-out stage. The rate of T_{htr} rise was steeper as heat flux increased and was based on the fact that the hydrophilic meniscus contact area on the H-spot started diminishing as evaporation continued. With more area of the heater without coolant, T_{htr} started increasing rapidly towards the end of this zone until the temporary dry-out stage. Beyond this stage, we still noticed dips in the T_{htr} due to the fact that the condensate on the underside of the top chip would sometimes re-emerge on the H-spot bringing down the temperature until it evaporated again as shown in Figure 4-19. The red arrows indicate the re-emergence of a droplet on the H-spot which takes
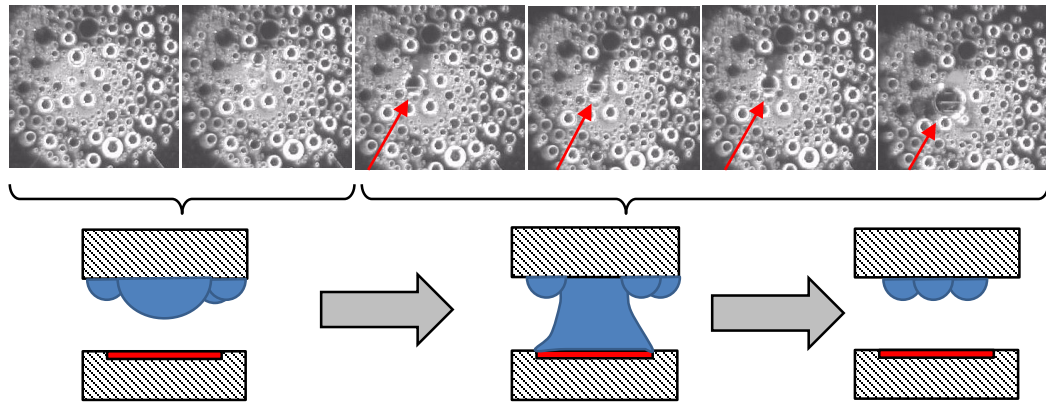
Figure 4-19 Analysis of droplet on H-spot showing condensate re-emergence for evaporation II zone.

place when the condensate coalesce under the top chip and are large enough to fill the gap between the top and bottom chip with liquid. This process occurred two or three times at all heat flux levels until a permanent dry-out stage was reached where this re-emergence of droplet stopped and the T_{htr} went back to its steady-state value.
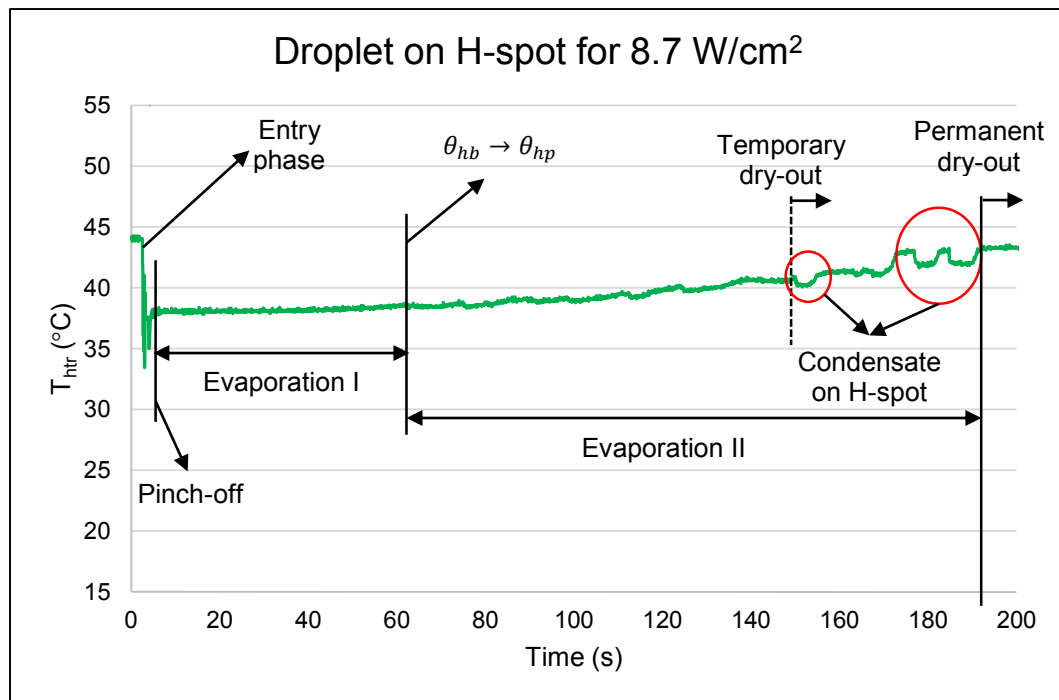
Figure 4-20 RTD data showing evaporation zones after pinch-off for 8.7 W/cm².
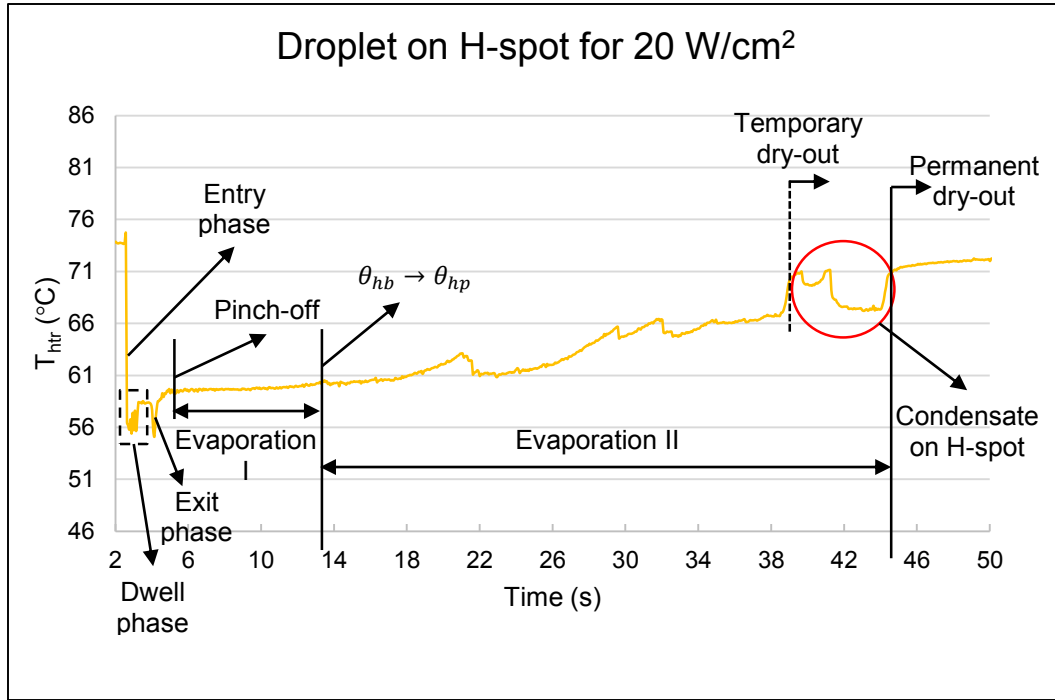
Figure 4-21 RTD data showing evaporation zones after pinch-off for 20 W/cm².

Figure 4-20, Figure 4-21 shows the evaporation phases for the 8.7 W/cm² and 20 W/cm² which showed effects similar to that of 36.6 W/cm² heat flux with stable temperature in evaporation I zone while temperature was rising unsteadily in evaporation II. The length of this evaporation zones depended on the excess volume pinched-off which was different in each of the three trials performed for each heat flux (only results with one trial were shown in this section). Between the two zones, the contact angle changed from hydrophobic to hydrophilic as explained earlier.

4.4.8 Extended Receding Meniscus on H-spot

Another interesting result observed was that when the receding meniscus was maintained on the hotspot for extended duration of time (no pinch-off), T_{htr} was regulated until dry-out of the main droplet (Figure 4-22 (a)). In order to observe effect of main droplet evaporation and boiling, the extended receding meniscus formation was shown at three instants for 36.6 W/cm² in Figure 4-22.
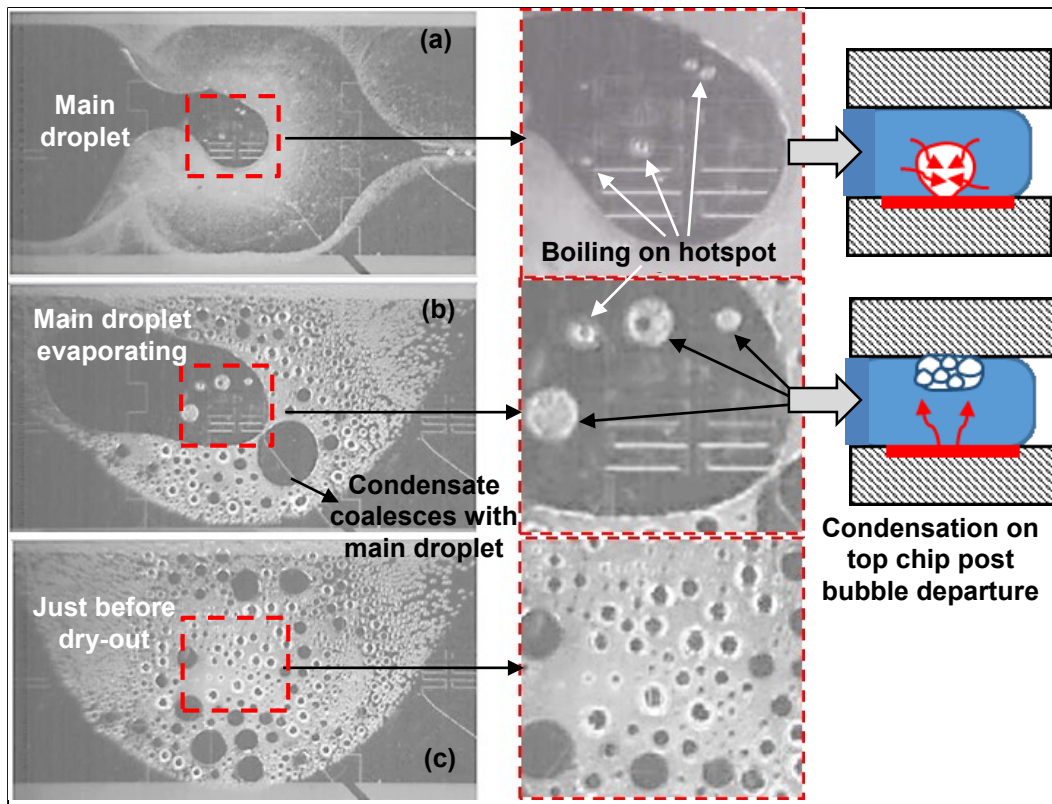
Figure 4-22 Results with extended meniscus on H-spot showing condensate coalescence.
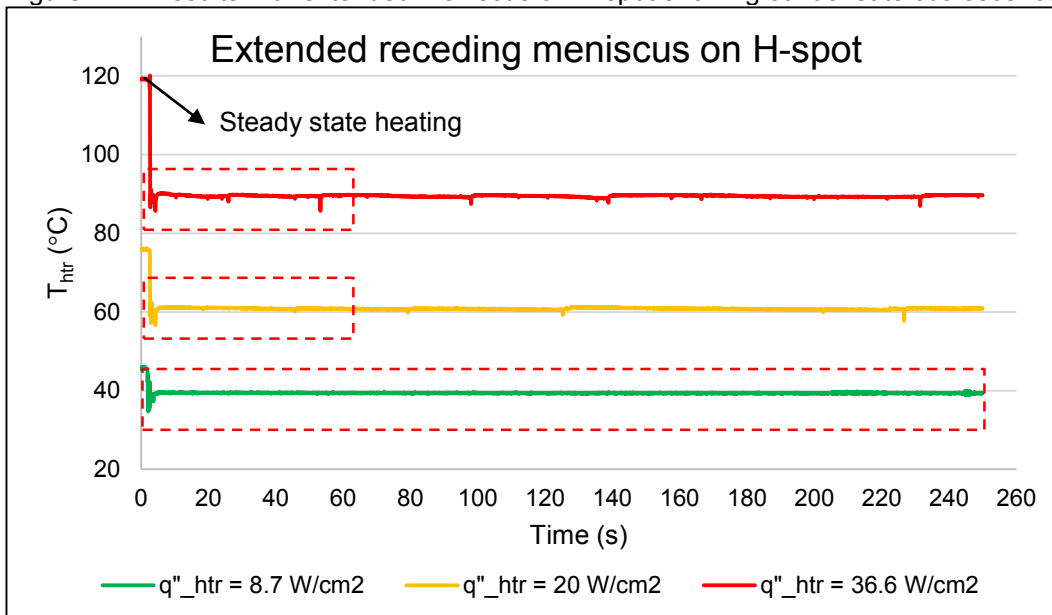
Figure 4-23 RTD data for extended meniscus on H-spot for three heat flux levels.
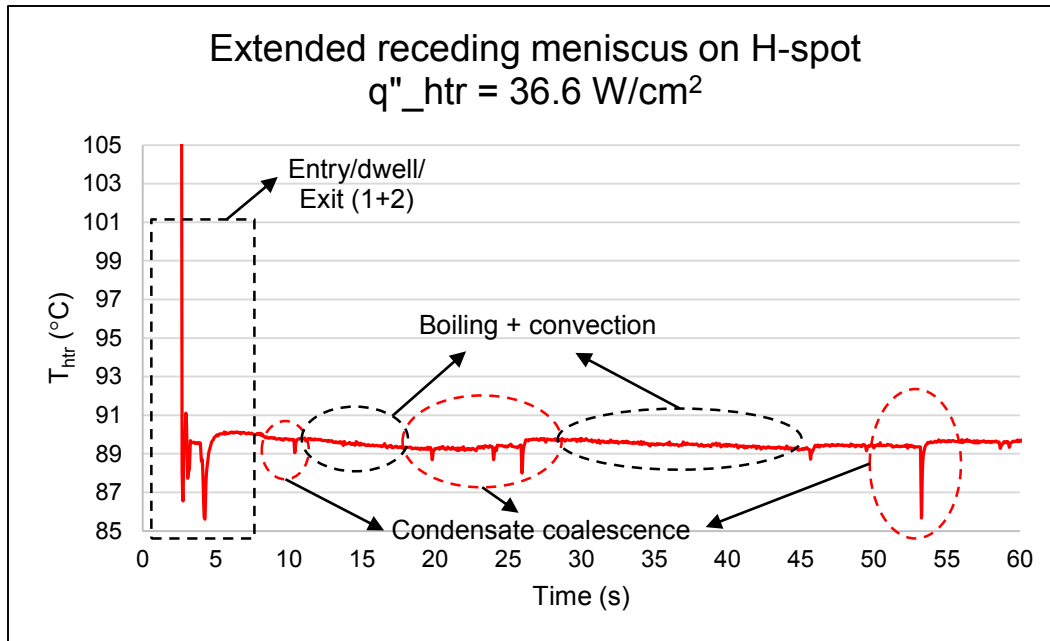
Figure 4-24 RTD data for 36.6 W/cm² showing predominant effects of receding meniscus on H-spot.
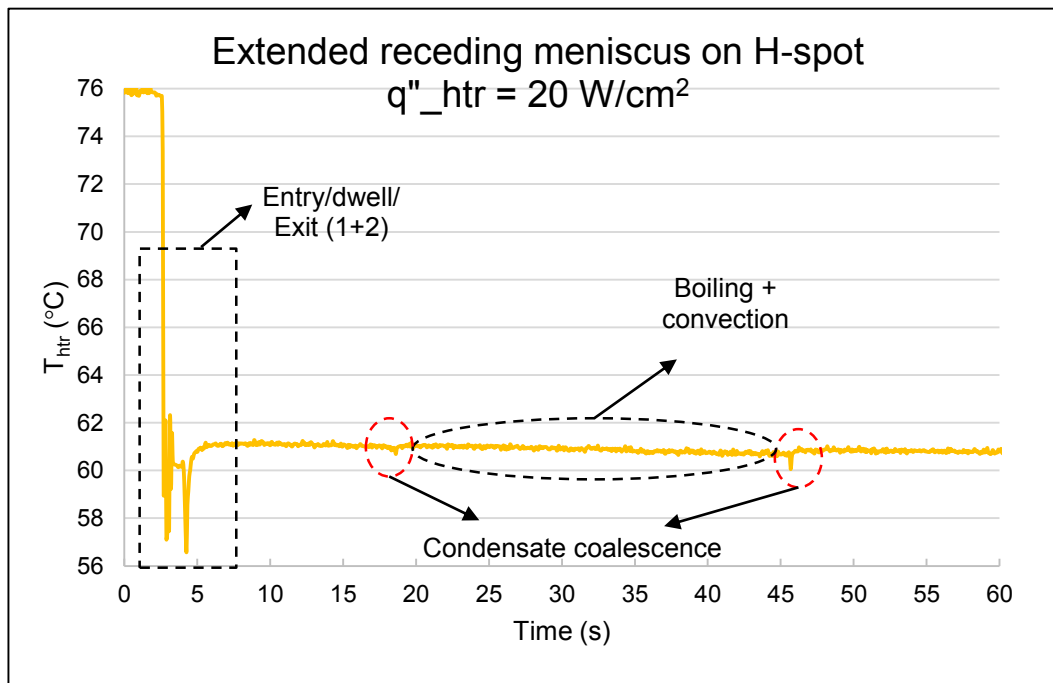
Figure 4-25 RTD data for 20 W/cm² showing considerable effects of receding meniscus on H-spot.
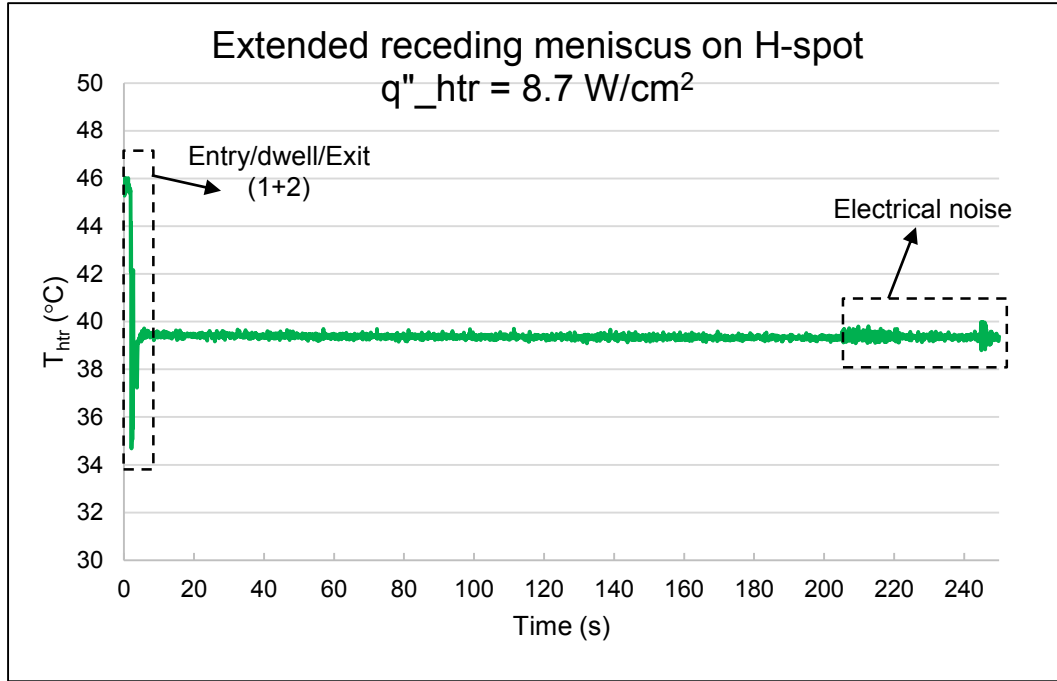
Figure 4-26 RTD data for 8.7 W/cm² showing minimal effects of receding meniscus on H-spot.

For lower heat flux levels, the boiling phenomena was very subdued (Figure 4-26). Referring back to Figure 4-22 (b), soon after the receding meniscus was formed, bubbles began to grow from the surface of the hotspot and after a certain time, the bubbles departed from the surface of hotspot and start condensing on the under-side of top chip. This appeared as vigorous evaporation and condensation within the initial bubble which had started to form from the surface. Apparently, the bubble departure seemed to have little to no effect in reducing T_{htr} but it seemed like the combined effect of Marangoni convection and boiling was responsible for the trend. The dips in T_{htr} was related to the constant coalescence of condensed droplets around the receding meniscus with the evaporating droplet on the H-spot. This trend continued until the entire droplet evaporated just before dry-out (Figure 4-22 (c)). The T_{htr} data was compared with the high-speed camera as done in the previous sections and key physics were identified during the main droplet evaporation with the receding meniscus pinned to the H-spot. The dotted region in Figure 4-23 represents the area considered for analysis in Figure 4-24, Figure 4-25 and Figure 4-26. For the low heat

flux levels, the above effects were not seen as most of the fluctuations was due to EWOD electrical noise (low heat flux in heater induces low signal-to-noise ratio (SNR) for the 8.7 W/cm^2 case).

4.5 Observations

4.5.1 Measurement of Average Overall Heat Transfer Coefficient in Evaporation I Zone

The overall heat transfer coefficient, $h_{ov,meas}$ was defined as the coefficient considering the conduction, convection and the phase-change thermal resistance from the heater to the ambient air surrounding the droplet on the H-spot in the evaporation I zone. In our case, as the T_{htr} and the surrounding conditions that affect h had a transient behavior, we referred to a paper by Lee et al. [35] which estimated the heat transfer coefficient as a function of time for a sessile refrigerant drop impinging on a heated surface. In the paper, the equation used for calculating the heat transfer coefficient depended on the experimental value, which was given in terms of the heater power and the ratio of the diameter after impact to the original one. Here, the transient heat transfer coefficient was re-written in terms of experimental parameters with regards to results obtained in section 4.4 to measure the overall heat transfer coefficient, $h_{ov,meas}$, and its average, $\overline{h_{ov,meas}}$ as

$$h_{ov,meas} = \frac{1}{(T_{htr}(t) - T_{amb}(t))} \cdot \frac{q(t)}{\pi a(t)^2} \qquad (4\text{-}2)$$

$$\overline{h_{ov,meas}} = \frac{\sum_t \frac{1}{(T_{htr}(t) - T_{amb}(t))} \cdot \frac{q(t)}{\pi a(t)^2}}{N} \qquad (4\text{-}3)$$

where

$T_{htr}(t)$ is the heater/RTD temperature at time t

$T_{amb}(t)$ is the ambient temperature as average of top chip and bottom RTD 3/RTD 5 (Figure 4-3)

$q(t) = I^2 * R(t)$ is the input power at time t for a current, I and heater/RTD resistance, $R(t)$

$a(t)$ is the contact radius of the droplet as measured from high-speed video analysis using results in section 4.4.5 using Cine Viewer 2.6 software from Vision Research, Inc.

N is the number of data points considered for measurements.
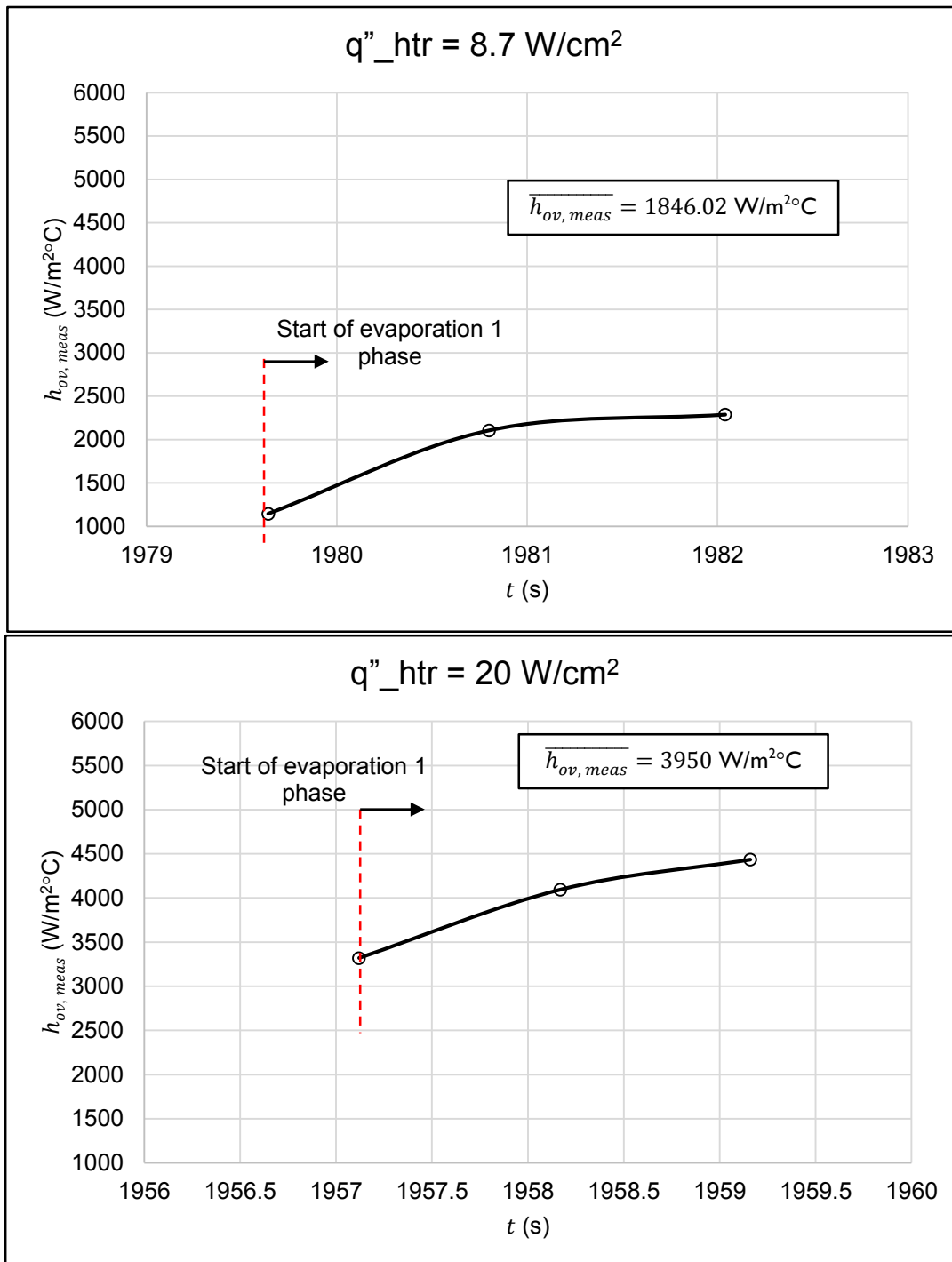
Figure 4-27 $\overline{h_{ov,meas}}$ measurement for 8.7 and 20 W/cm².
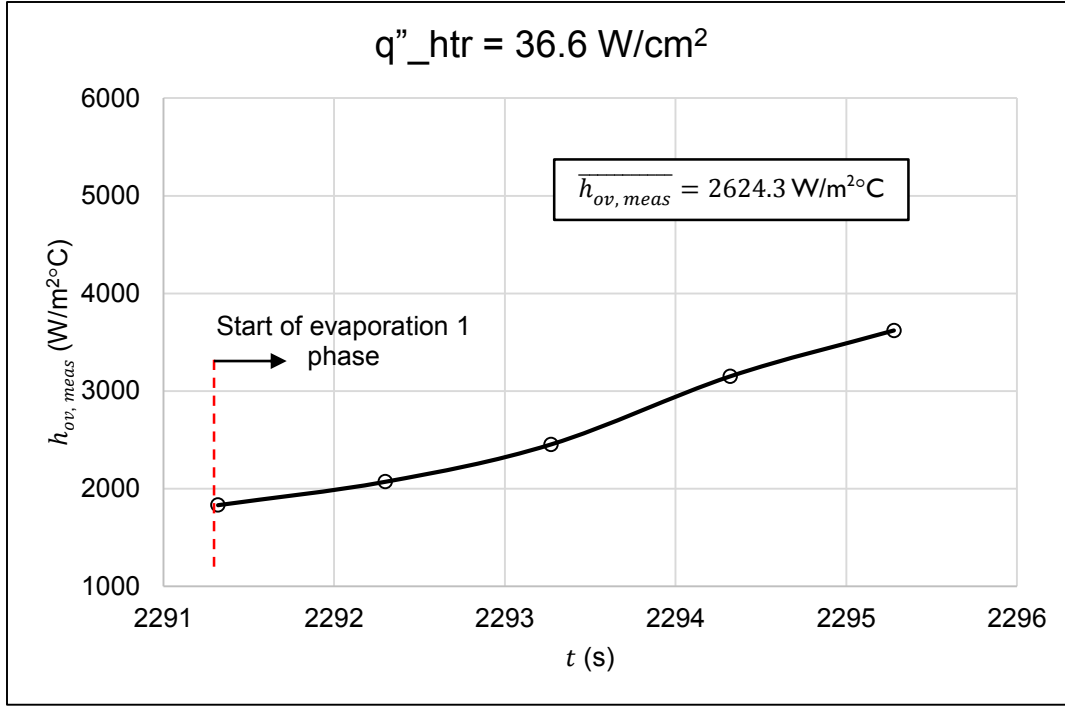
Figure 4-28 $\overline{h_{ov,\,meas}}$ measurement for 36.6 W/cm².

Figure 4-27, Figure 4-28 shows the plot of the $\overline{h_{ov,\,meas}}$ for three levels of heat flux tested. In Figure 4-27, as the high-speed camera had a limitation of only 8 seconds of total video shooting capability from droplet entry to dry-out, the contact radius could not be measured for more than three data points. Figure 4-28 shows the results with 36.6 W/cm² heat flux. An increasing trend was observed in the $h_{ov,\,meas}$ measurements with time due to the fact that the contact radius, a in equation 4-2 was decreasing at a second order rate with time, t. The decrease in the input power, $q(t)$ and change in $T_{htr}(t)$ (from evaporation zone results in sections 4.4.6 and 4.4.7) did not offset the change in $h_{ov,\,meas}$ at the rate at which a was changing.

4.5.2 Parametric analysis of thermal diffusivity of fluid, α_{fluid}

In CHAPTER 2, numerical results of single drop for two coolants, namely Ionic Liquid and DI water were presented. DI water offered better cooling performance due to three times higher thermal conductivity and four times higher heat capacity than that of IL. Based on this result, we wanted to extend the choice of

77

the coolant beyond these two liquids in order to get a sense of how fluid properties like k_{fluid}, ρ_{fluid}, $C_{p,fluid}$

and how they affect T_{htr}.
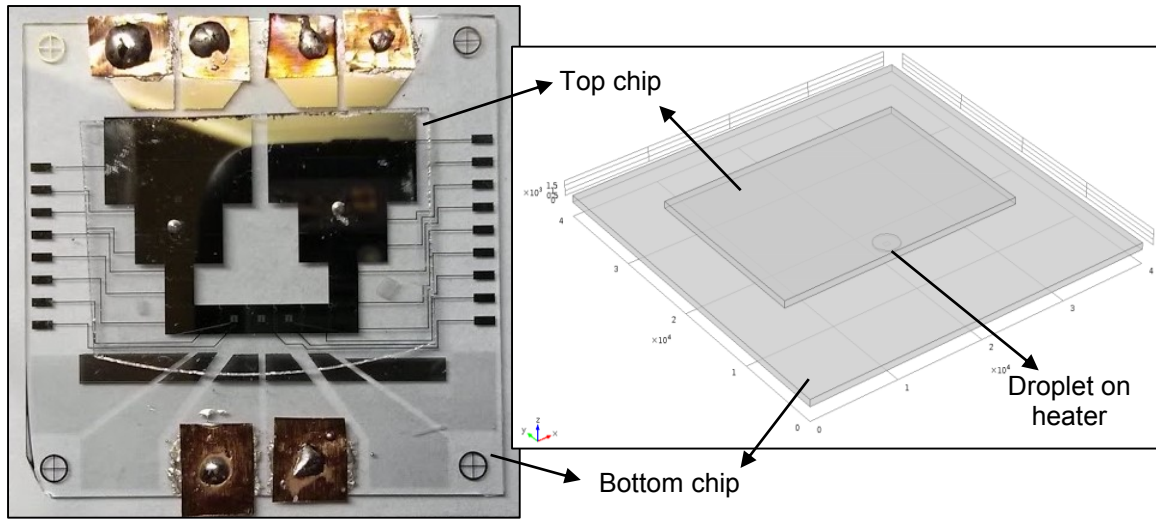
Figure 4-29 Model for parametric analysis with only the top and bottom chip setup modeled.
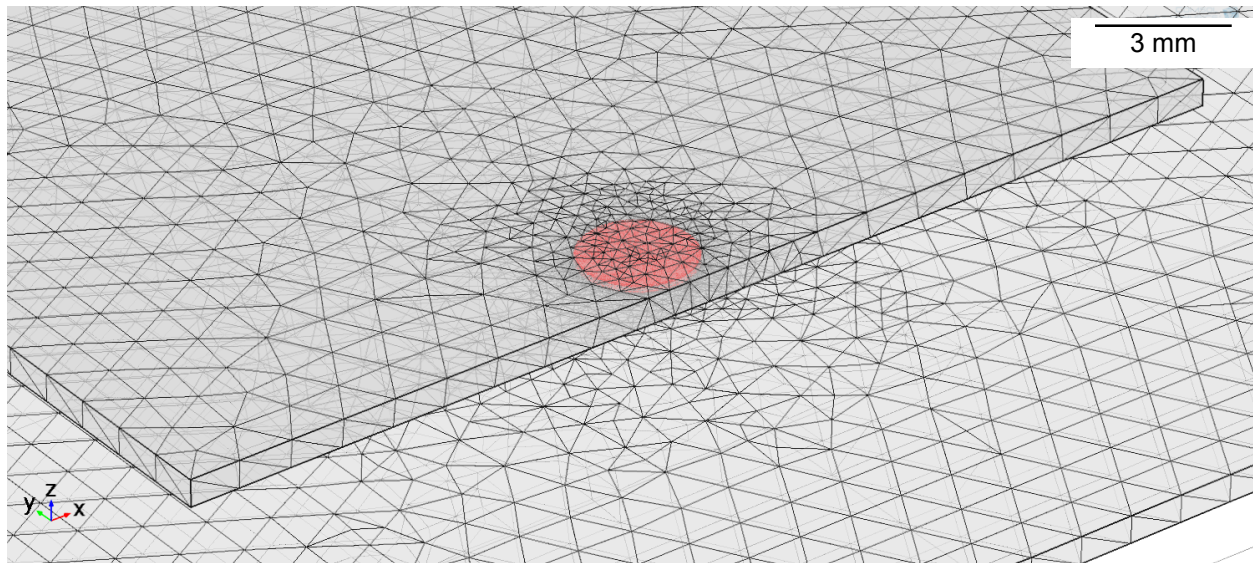
Figure 4-30 Figure showing mesh refinement at droplet and surrounding domains.

We were also interested in comparing the droplet temperature distribution and observe heat transfer in droplet and surrounding domains. Therefore, we chose Mercury (Hg) and Gallium (Ga) as our fluid properties of interest and compared maximum T_{htr} with simulations using a simplified RTD hotspot

cooling setup as shown in Figure 4-29. It was determined that removing the PDMS gasket and the PG holders did not affect T_{htr} so in order to reduce the simulation time, the drop and EWOD devices were separated from the other parts in the model. The mesh procedure as shown in Figure 4-30 involved sub-modeling techniques at the drop and its surrounding domains as our area of focus was solving for the temperature solution for various values of fluid parameters. Multiple solver configurations were used and a parametric analysis was performed for combinations as shown in Table 4-1.

Table 4-1 Table with properties for droplet and values used for parameters.

Parametric variables	$q"_{htr}$ (W/cm^2)		q'_m (W/cm)			Property combinations			$\propto_{fluid} = \dfrac{k_{fluid}}{\rho_{fluid} \cdot Cp_{fluid}}$
	Low	High				k_{fluid} (W/m.K)	ρ_{fluid} (kg/m^3)	Cp_{fluid} (J/kg.K)	(m^2/s)
Values	36.6	88.2	0	10 x10^{-2}	20 x10^{-2}	$k_{IL} = 0.19$	$\rho_{IL} = 1100$	$Cp_{IL} = 1571$	1.099 x 10^{-7}
						$k_{DI} = 0.56$	$\rho_{DI} = 1000$	$Cp_{DI} = 4000$	1.4 x 10^{-7}
						$k_{Hg} = 8.9$	$\rho_{Hg} = 13579$	$Cp_{Hg} = 139$	4.71 x 10^{-6}
						$k_{Ga} = 40.6$	$\rho_{Ga} = 5910$	$Cp_{Ga} = 370$	1.85 x 10^{-5}

The B.C.'s used for the model are summarized in Figure 4-31 (a) which included insulation B.C. for the top side of the top chip and sides, bottom of the bottom chip. A natural convection B.C. was provided to top side of bottom chip and bottom side, sides of bottom chip including the drop meniscus surface in Figure 4-31 (b). The meniscus evaporation, q'_m for the edge B.C. was also provided along with the heat

$$-n.(-k\nabla T_{dom}) = 0 \qquad -n.(-k\nabla T_{dom}) = h_{amb}.(T_{dom} - T_{amb}) \qquad \begin{array}{l} -n.(-k\nabla T_{dom}) = q"_{htr} \\ -n.(-k\nabla T_{dom}) = -q'_m \end{array}$$
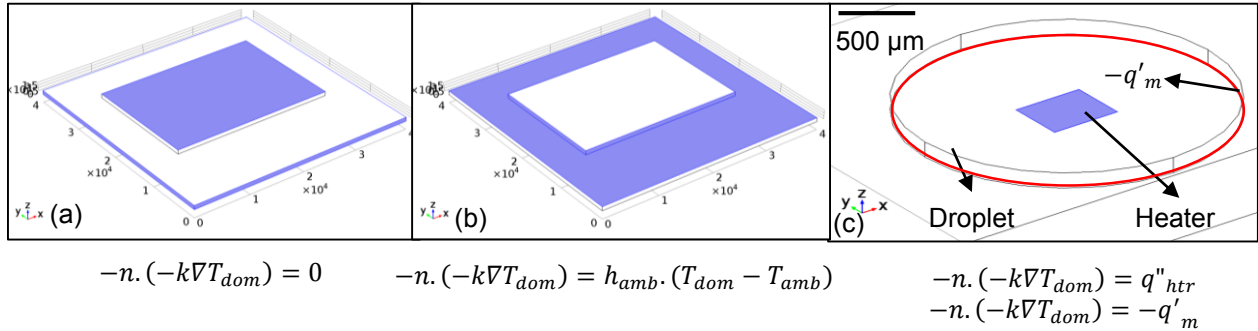
Figure 4-31 Figure showing B.C.s used in the parametric model.

flux B.C. to the heater surface, $q"_{htr}$ in Figure 4-31 (c). The final temperature of the domain, T_{dom} was the solution for the cases as outlined in Table 4-1.
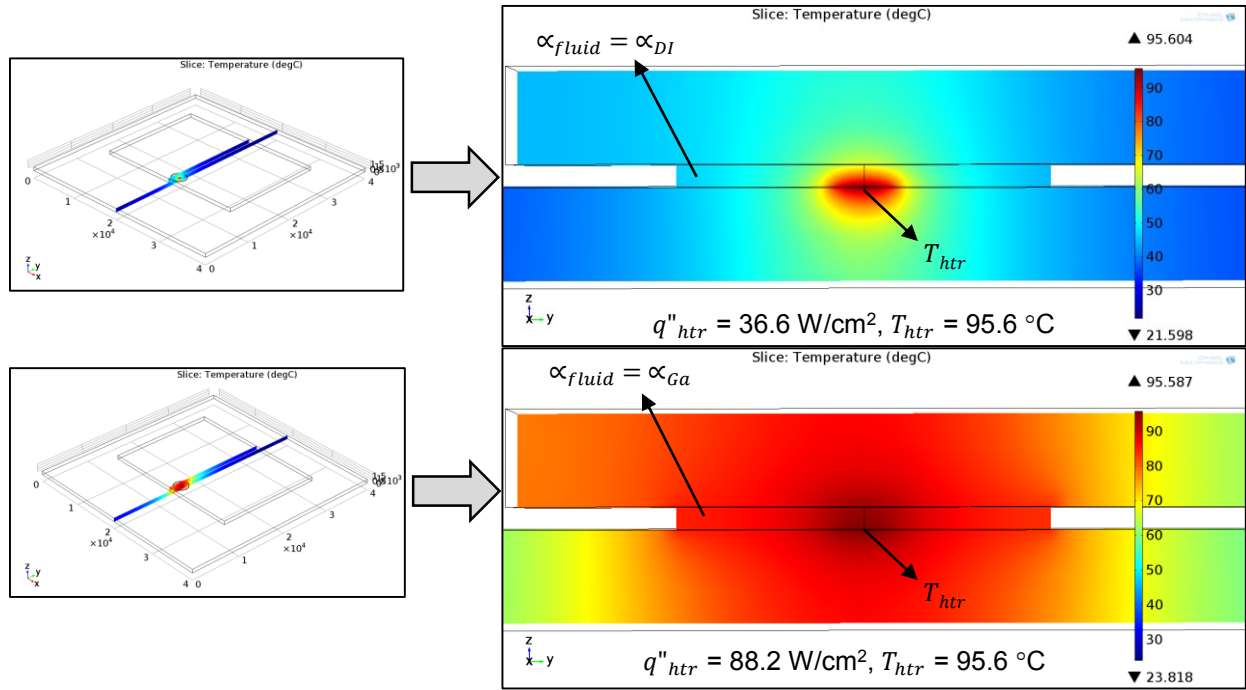
Figure 4-32 Step 1 results showing results for $\propto_{DI}$ and $\propto_{Ga}$ giving same T_{htr} for low and high $q"_{htr}$.

The modeling procedure involved three steps:

STEP 1: Reaching steady-state conditions of system

- DI water was used as the fluid domain to attain steady-state temperature of the domains for low (experimental) $q"_{htr} = 36.6$ W/cm².

- Ga liquid was set as the fluid domain to attain steady-state temperature of the domains for high $q"_{htr} = 88.2$ W/cm².

The slice view (cross-section) results for step 1 are shown in Figure 4-32. The end result of step 1 was that the steady-state results for the experimental $q"_{htr}$ of 36.6 W/cm² and theoretical $q"_{htr}$ of 88.2 W/cm² was the same. This was to show that we could achieve high heat flux cooling using a better coolant like Gallium.

STEP 2: Cooling the fluid domain temporarily (pre-cool)

- Initial condition for step 2 was set as steady-state result in step 1.

- Fluid temperature was brought close to room temperature by running step 2 for 2 ms time duration with 0.1 ms step.

- This simulation step emulates fresh droplet coming in while remaining domains are at elevated temperatures.
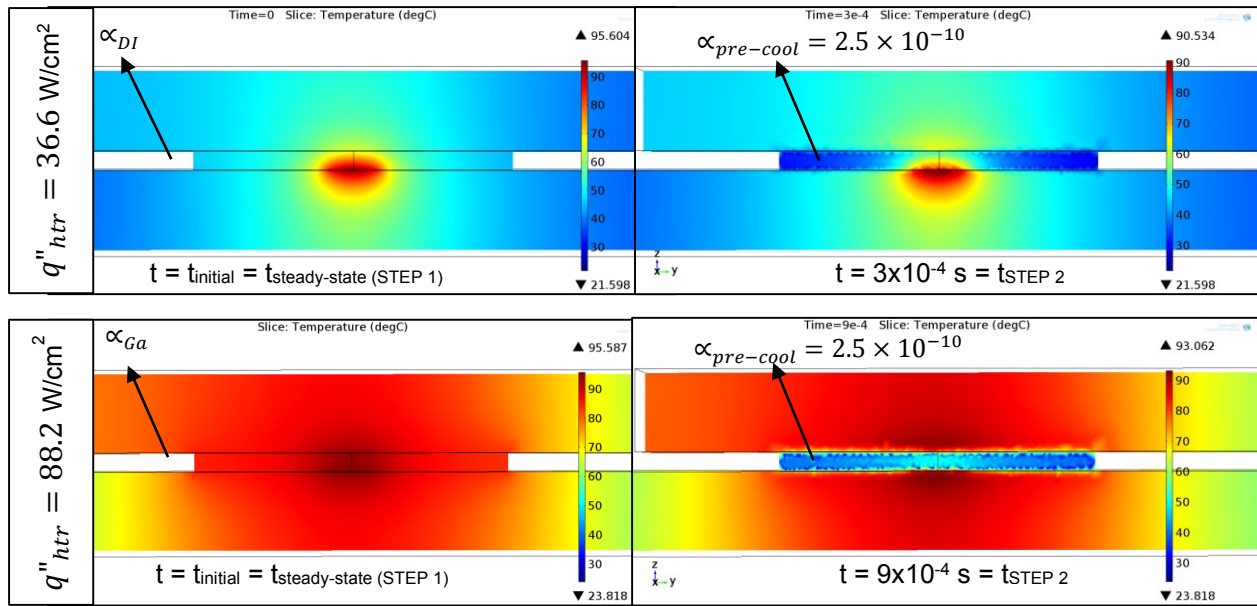
Figure 4-33 Pre-cool results for 36.6 and 88.2 W/cm^2 showing reduced temperatures of fluid domain.

As shown in Figure 4-33, the pre-cool step was performed by choosing a material with a very low thermal diffusivity, $\propto_{pre-cool}$. When transient simulation was performed for 2 ms time duration, the temperature of the fluid domain was still at room temperature without affecting T_{htr} substantially.

STEP 3: This step involved running transient simulation for dwell phase time (1.5 s) for varying $\propto_{fluid}$

- The initial condition was set at final result of step 2 ($t_{step\,2}$).

- Temperature distribution of domains, T_{dom} was observed at end of dwell.

- T_{htr} variation with dwell phase time (t) observed.

- Meniscus evaporation for all coolants (except IL) varied.

81

Figure 4-34 Grid showing variation of $\propto_{fluid}$ with meniscus evaporation, q'_m for 36.6 W/cm².
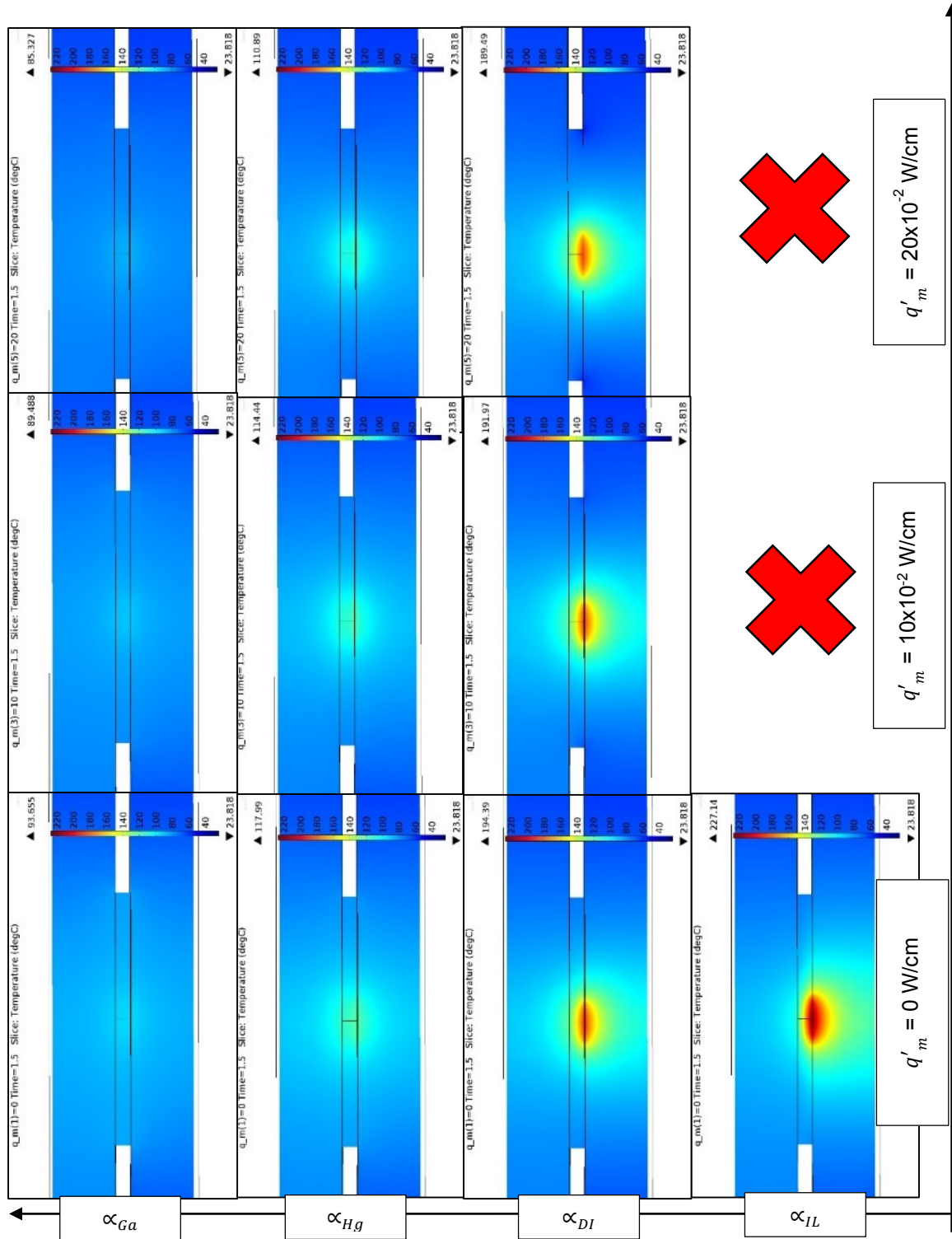
Figure 4-35 Grid showing variation of α_{fluid} with meniscus evaporation, q'_m for 88.2 W/cm^2.

Figure 4-34 shows the results for varying the coolant and the corresponding meniscus evaporation values from Table 4-1 for 36.6 W/cm^2 case. As stated earlier, evaporation condition was not emulated for IL as it does not exhibit phase-change. From the results, the lowest T_{htr} = 43.253 °C was observed for $\propto_{Ga}$ with an evaporation rate of 20x10^{-2} W/cm. Similarly, Figure 4-35 shows the results for 88.2 W/cm^2 with the
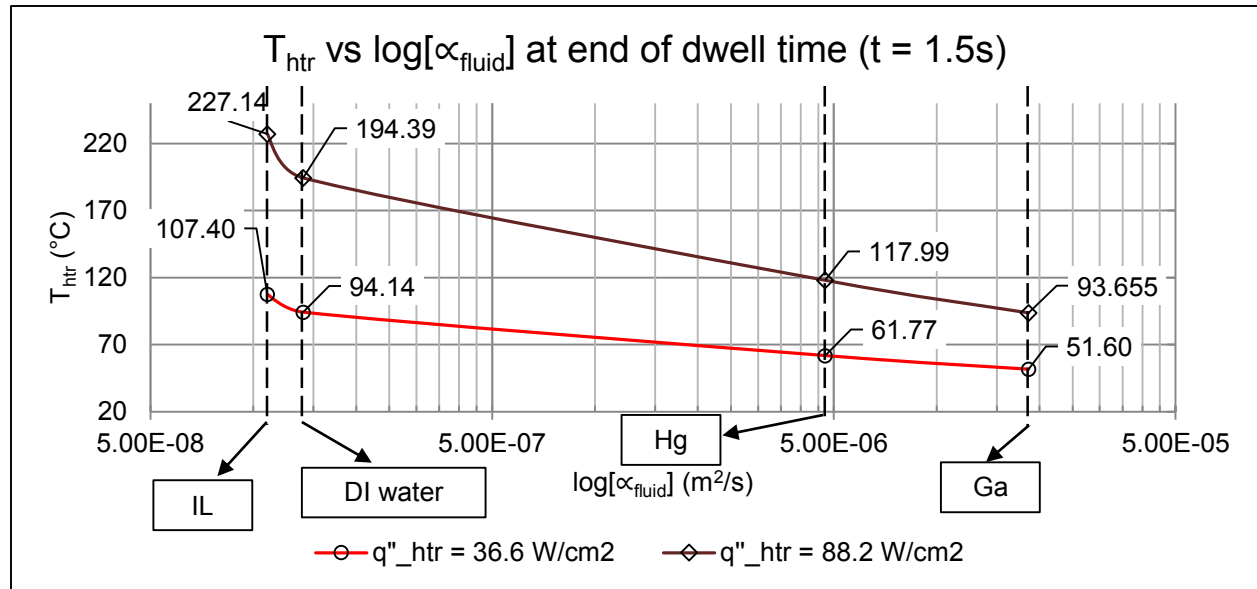
Figure 4-36 Effect of $\propto_{fluid}$ on T_{htr} for two heat flux cases excluding evaporation.
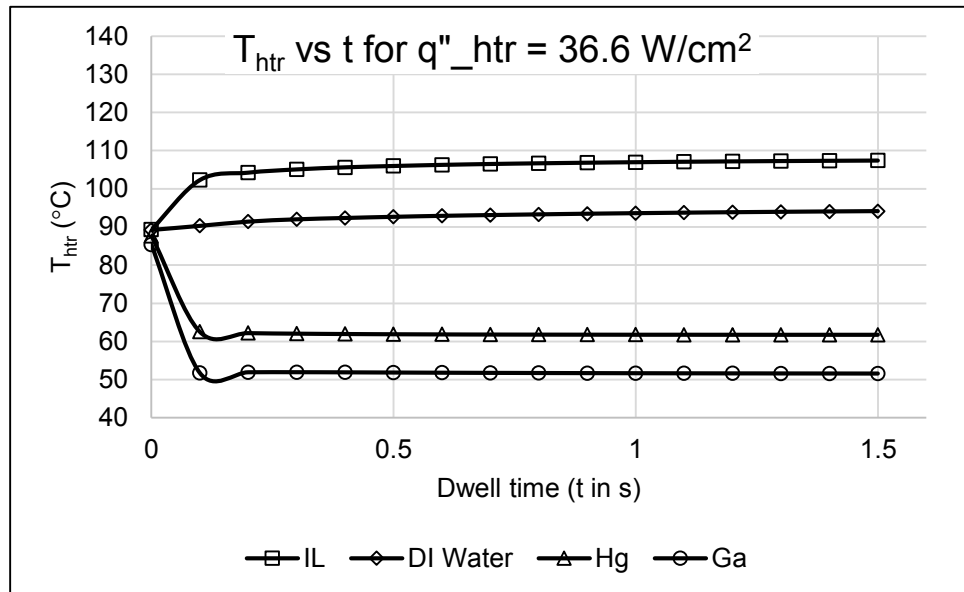
Figure 4-37 Transient result of the T_{htr} variation with dwell time for 36.6 W/cm^2.

lowest T_{htr} = 85.327 °C observed for $\propto_{Ga}$ with an evaporation rate of 20x10⁻² W/cm. In order to visualize

the effect of changing the coolants for q'_m = 0, the thermal diffusivity parameter values at the end of dwell

phase (step 3 simulation) were used and its logarithmic values were plotted with T_{htr} for the two q''_{htr} cases

in Figure 4-36. A transient analysis of T_{htr} with dwell time t was also shown to get a sense of how the

coolants affect the T_{htr} during the dwell phase at the two heat flux levels in Figure 4-37, Figure 4-38.
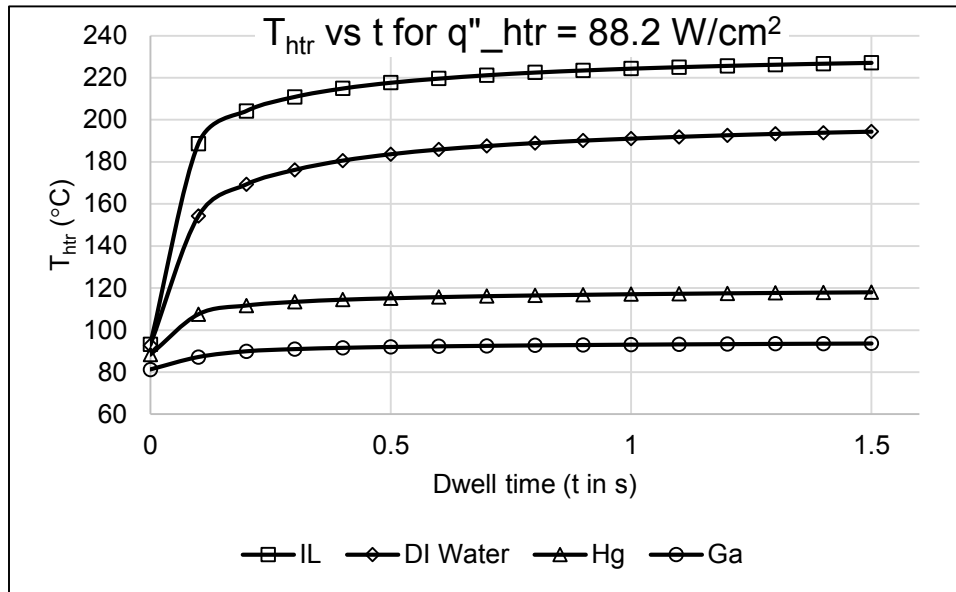
Figure 4-38 Transient result of the T_{htr} variation with dwell time for 88.2 W/cm².

Table 4-2 Maximum temperature of T_{htr} for varying q'_m and $\propto_{fluid}$.

q''_{htr} (W/cm²)	T_{htr} (max.) for q'_m (°C)			ΔT_{htr} with evaporation	$\propto_{fluid}$
	0 W/cm	10x10⁻² W/cm	20x10⁻² W/cm	0 - 20x10⁻² W/cm	
36.6	107.4	-	-	-	$\propto_{IL}$
	94.136	91.718	89.307	4.829	$\propto_{DI}$
	61.774	58.214	54.644	7.13	$\propto_{Hg}$
	51.6	47.421	43.253	8.347	$\propto_{Ga}$
88.2	227.14	-	-	-	$\propto_{IL}$
	194.39	191.97	189.49	4.9	$\propto_{DI}$
	117.99	114.44	110.89	7.1	$\propto_{Hg}$
	93.655	89.488	85.327	8.328	$\propto_{Ga}$

The maximum temperature values based on the above results are summarized in Table 4-2 for varying meniscus evaporation, q'_m and $\propto_{fluid}$. The maximum drop in T_{htr} between no evaporation to highest evaporation value was for $\propto_{Ga}$ across the two heat flux levels.

4.5.3 Comparison of evaporation rates in experiments to COMSOL simulations based on ideal q'_m

The evaporation rate was calculated for the experimental $q"_{htr}$ based on the overall heat transfer coefficient estimation, $h_{ov,meas}$ at the beginning of the evaporation I zone in section 4.5.1 and compared with ideal values within the range used in the simulations in Table 4-3. The evaporation rate compared this way was a crude estimation based on the initial volume of the droplet as the COMSOL simulation in section 4.5.2 did not account for mass transfer. The measured evaporation rate, $Q_{evp,meas}$ was estimated as

$$Q_{evp,meas} = h_{ov,meas}.A_m.(T_{htr} - T_{amb}) \tag{4-4}$$

where, meniscus surface area, $A_m = 2\pi a H$ with a being the radius of the droplet at the beginning of the evaporation I zone and H being the spacer gap height. The values of T_{htr} and T_{amb} were also measured at the $h_{ov,meas}$ value corresponding to beginning of evaporation I zone. For ideal values of q'_m in section 4.5.2, the evaporation rate in simulations, $Q_{evp,sim}$ was estimated as

$$Q_{evp,sim} = 2\pi a q'_m \tag{4-5}$$

Table 4-3 Comparison of $Q_{evp,meas}$ to $Q_{evp,sim}$ for experimental values of $q"_{htr}$.

$q"_{htr}$ (W/m²)	a (m)	A_m (m²)	T_{htr} (°C)	T_{amb} (°C)	$h_{ov,meas}$ (W/m².°C)	$Q_{evp,meas}$ (W)	Ideal q'_m (W/m)	$2\pi a$ (m)	$Q_{evp,sim}$ (W/m)
8.7x10⁴	7.5x10⁻²	7.77x10⁻⁷	38.09	24.55	1145.73	1.2x10⁻²	5	47.1x10⁻⁴	2.4x10⁻²
20x10⁴	4.4x10⁻²	4.58x10⁻⁷	59.35	27.83	3319.18	4.8x10⁻²	15	27.7x10⁻⁴	4.1x10⁻²
36.6x10⁴	6x10⁻²	6.21x10⁻⁷	90.75	32.46	1831.21	6.6x10⁻²	20	37.7x10⁻⁴	7.5x10⁻²

4.6 <u>Conclusions</u>

In this chapter, a detailed study of the droplet motion over the hotspot was made using high-speed camera in synchronization with the RTD data. In order to understand the heat and mass transfer physics, a hydrophilic spot on the heater was fabricated which enabled a small droplet to be pinched-off on the heater. Four phases of droplet motion were identified and the T_{htr} data was analyzed in detail. Two zones of evaporation were demarcated using the RTD data and it was inferred that evaporation II zone had rapid rise in T_{htr} until a temporary dry-out stage was reached. Beyond this stage, we also noticed droplet re-emergence on the H-spot by excess condensate accumulation on the underside of the top chip. This also had a momentary effect in reducing T_{htr} by a maximum of 6 °C. An extension of the receding meniscus on the H-spot was also studied which gave interesting droplet condensation effects within the bubble departed from the nucleation site on the H-spot. Observations of condensate coalescence with the droplet on H-spot was noticed which dropped the T_{htr} by a maximum of 5 °C for the 36.6 W/cm² case.

A simplified model was setup in COMSOL to study the effect on changing the thermal diffusivity, $\propto_{fluid}$ and its effect on the heater temperature T_{htr}. It was observed that amongst four coolants tested, Ga had the best cooling capacity as evident by its high thermal conductivity. It was also noted that for increased heat flux of 88.2 W/cm² (higher than experimental limits), Ga liquid served as an excellent coolant by regulating temperature well below the initial temperature before the dwell phase. A maximum drop in T_{htr} of 64.147 °C with respect to $\propto_{IL}$ was observed for $\propto_{Ga}$ case for the highest evaporation B.C. for 36.6 W/cm². Similarly, a drop of 141.813 °C was observed again for $\propto_{Ga}$ for 88.2 W/cm².

Finally, the evaporation rates in the experiments, $Q_{evp,meas}$ were compared to the range of values used for the simulations, $Q_{evp,sim}$ in which they were found to be in the same order and agreed well with each other.

CHAPTER 5

CONCLUSIONS

This work outlines a study of a digital microfluidics (DMF) electrowetting on dielectric (EWOD) based hotspot cooling system for IC hotspot cooling by designing and testing two proof-of-concept systems using liquid crystals and Indium Tin Oxide Resistance Temperature Detectors (ITO RTDs). Two coolant liquids were tested with LCT, namely DI water and Ionic Liquid of which DI water was selected as the coolant of choice for detailed study involving phase-change heat transfer.

1. For LCT analysis, DI water showed highest drop in LC temperature compared to IL.

2. The combined effects of phase-change and Marangoni convection flow due to thermocapillary gradient lowered the temperature of the ITO RTD by 3°C to 6°C for the highest heat flux at the entry/exit meniscus.

3. Four phases of droplet motion were identified and T_{htr} data was analyzed in detail. Two zones of evaporation were demarcated using the RTD data and it was inferred that evaporation II zone had rapid rise in T_{htr} until a temporary dry-out stage was reached. Beyond this stage, droplet re-emergence on the H-spot was noticed by excess condensate accumulation on the underside of the top chip. This also had a momentary effect in reducing T_{htr} by a maximum of 6 °C. An extension of the receding meniscus on the H-spot was also studied which gave interesting droplet condensation effects within the bubble departed from the nucleation site on the H-spot. Observations of condensate coalescence with the droplet on H-spot was noticed.

4. A simplified model was setup in COMSOL to study the effect on changing the thermal diffusivity, $\propto_{fluid}$ and its effect on the heater temperature, T_{htr}. It was observed that among four coolants tested, Ga had the best cooling capacity as evident by its high thermal conductivity. It was also noted that for increased heat flux of 88.2 W/cm^2 (higher than experimental limits), Ga liquid served as an excellent coolant by regulating temperature well below the initial temperature before the dwell phase.

CHAPTER 6

FUTURE WORK AND RECOMMENDATIONS

6.1 Multiple Droplet on H-spot

An extension of the droplet on H-spot was to achieve high heat flux cooling (> 50 W/cm^2) experimentally by pinching-off more than one droplet and having multiple droplets entering the hotspot electrode. This will not only regulate T_{htr} at high heat flux levels but also prevent dry-out stages as noticed in previous chapter. While work is in progress to generate continuous droplets in multiples of 10, we were able to successfully demonstrate two droplets pinch-off on the H-spot. As shown in Figure 6-1, the first droplet enters the H-spot in Figure 6-1 (a) and forms a receding tail meniscus in Figure 6-1 (b). As soon as
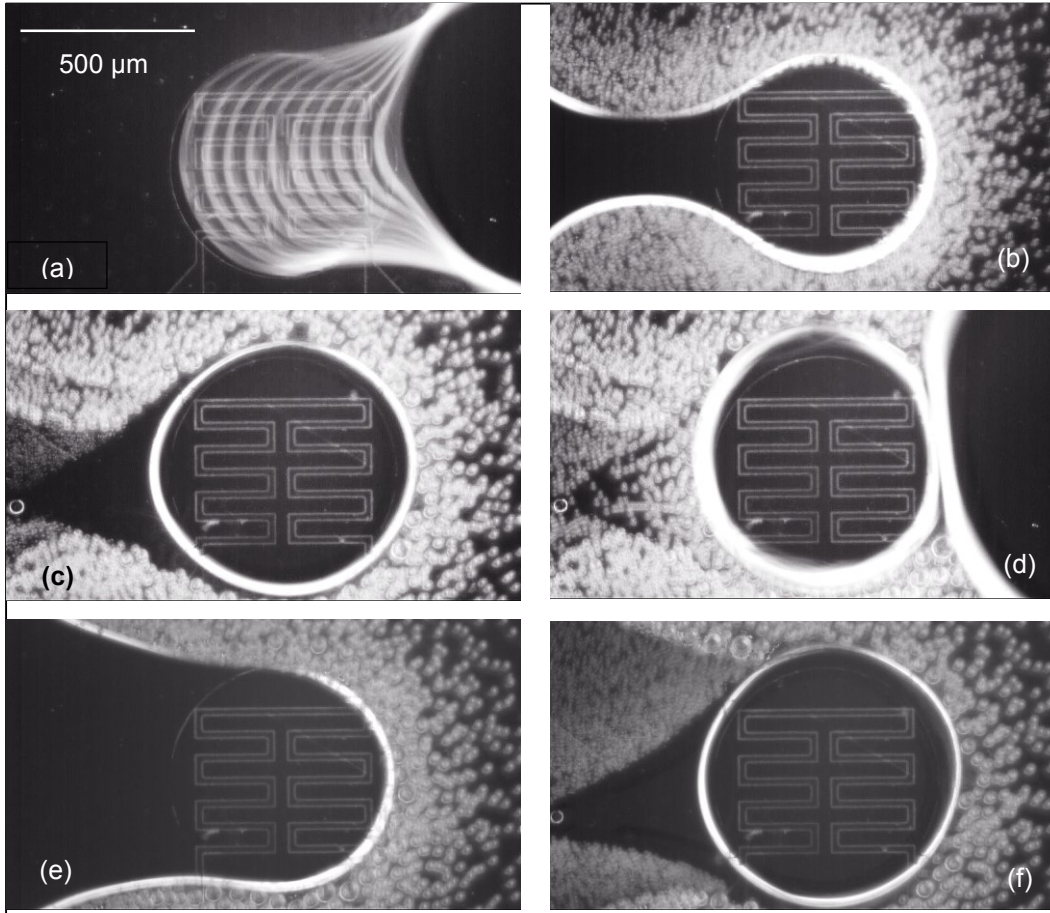
Figure 6-1 Snapshots showing multiple droplet pinch-off ((a) through (f)) on the H-spot for 50 W/cm^2.

pinch-off takes place in Figure 6-1 (c), a fresh droplet merges with the droplet on the H-spot in Figure 6-1

(d) and then forms a receding meniscus again in Figure 6-1 (e). This cycle can be repeated for multiple

droplets and the dry-out in Figure 6-1 (f) can be delayed (compared to 36.6 W/cm^2 result in Figure 4-18)

while maintaining T_{htr} as shown in Figure 6-2.
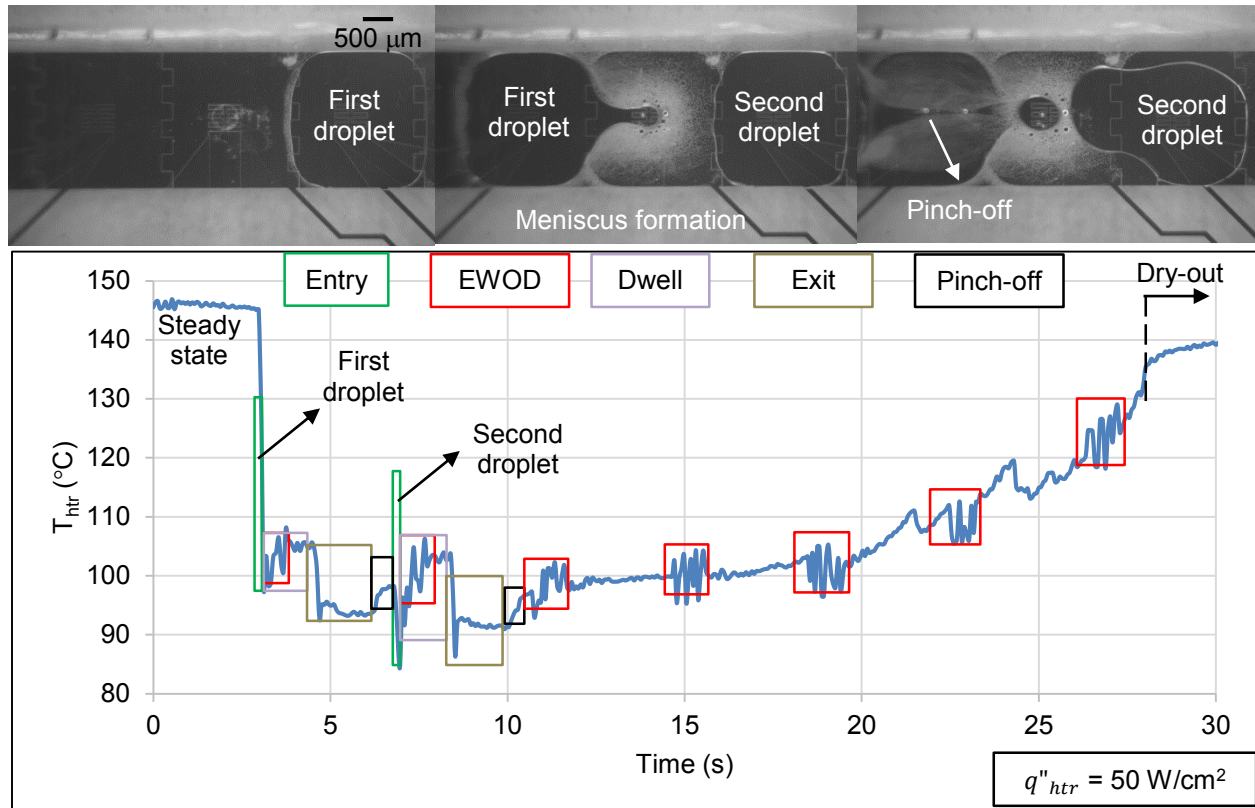
Figure 6-2 Analysis of multiple droplet pinch-off on H-spot for 50 W/cm^2 heat flux.

6.2 Recommendations

Based on the innovative demonstration and research attempted on EWOD DMF based hotspot

cooling technique for IC cooling in this dissertation, a number of prospective topics for further studies were

identified:

1. Incorporation of a closed-loop cooling system

    - A closed-loop cooling system including a heat source and a heat sink (eg. TECs) can be

        incorporated thereby completing the heat transfer system.

2. The numerical simulations performed in this research can be improved by including droplet motion physics

   - By using COMSOL Multiphysics, a more accurate model can be derived by combining Lippman-Young equations to the Navier Stokes (N-S) equations to estimate the flow field in the droplet. This solution could then be transferred to the energy equation to form a coupled multiphysics problem.

3. Better synchronization of testing setup

   - In order to synchronize the RTD data and high-speed video automatically, better integration of the experimental procedure with the DAQ hardware is recommended.

4. Testing better coolants on-chip

   - New coolants with enhanced thermal properties can be physically tested on-chip and the experimental data can be compared with numerical simulations.

   - Depending on the coolant, the B.C.s of the testing setup can be changed to meet the demands of high heat flux cooling applications.

5. Improvised setup for better control

   - Cooling performance under various parameters like pressure, humidity etc. can be studied for better understanding of EWOD DMF cooling under various real world conditions.

6. Thin-film evaporation study on hotspot

   - To utilize phase-change to the fullest advantage, hydrophilic thin films which enhance phase-change heat transfer can be coated on chip and the cooling performance can be studied in detail.

REFERENCES

[1] K. Seshan, Handbook of Thin Film Deposition, 3rd Edition, Elsevier, 2012.

[2] H. Xie, M. Aghazadeh, W. Lui and K. Haley, "Thermal Solutions to Pentium Processors in TCP in Notebooks and Sub-notebooks", IEEE Transactions on Components, Packaging and Manufacturing Technology. Part A, Vol. 19, No. 1, pp54-65, March, 1996.

[3] H. Xie, M. Aghazadeh and J. Toth, "The Use of Heat Pipes for the Cooling of Portables with High Power Packages--A Case Study with the Pentium® Processor Based Notebooks and Sub-notebooks", pp.906-913, 45th ECTC, Las Vegas, Nevada, 1995

[4] "Advances in heat pipe science and technology", Proceedings of the IX international heat pipe conference, May 1-5, 1995, Albuquerque, New Mexico.

[5] S. V. Garimella, "Advances in Mesoscale Thermal Management Technologies for Microelectronics", Microelectronics Journal, Vol. 37, pp. 1165–1185, 2006.

[6] Kercher, D. S. et al., "Microjet Cooling Devices for Thermal Management of Electronics", IEEE Transactions on Components and Packaging Technologies, Vol. 26, No. 2, June 2003.

[7] S. H. Moon and G. Hwang, "Development of the micro capillary pumped loop for electronic cooling", THERMINIC 2007, September 2007, ISBN: 978-2-35500-002-7.

[8] E. G. Colgan et al., "A practical implementation of silicon microchannel coolers for high power chips", IEEE Transactions on Components and Packaging Technologies, June 2007, Vol. 30, No. 2, pp. 218-225

[9] Redmond et al., "Optimization of Thermoelectric Coolers for Hotspot Cooling in Three-Dimensional Stacked Chips", Journal of Electronic Packaging, pp. 011006-1 to 011006-6, March 2015.

[10] Jiang, L. et. al., "Closed-loop Electroosmotic Microchannel Cooling System for VLSI Circuits", Proceeding of SEMI-THERM, Vol. 17, pp. 153 – 157, 2001.

[11] Heffington, S.N., and A. Glezer, "Two-Phase Thermal Management using a Small-Scale, Heat Transfer Cell Based on Vibration-Induced Droplet Atomization," Ninth Intersociety Conference on

Thermal and Thermomechanical Phenomena in Electronic Systems (ITherm 2004), Las Vegas, NV, 2004.

[12] J. Schutze, H. Ilgen, W.R. Fahrner, "An Integrated Micro Cooling System for Electronic Circuits", IEEE Trans. on Industrial Electronics, vol. 48, no. 2, pp. 281-285, April 2001.

[13] Maltezos, A. Rajagopal, A. Scherer, "Evaporative Cooling in Microfluidic Channels", Appl. Phys. Lett. 2006, 89, 074107:1–074107:3.

[14] H. Moon et al., "Low Voltage Electrowetting-on-dielectric", Journal of Applied Physics, October 2002, Vol. 92, No. 7, pp. 4080-4087.

[15] F. Mugele et al., "Electrowetting: From Basics to Applications", Journal of Physics: Codensed Matter, 2005, pp. 705-742.

[16] C. Quilliet and B. Berge, "Electrowetting: A Recent Outbreak", Current Opinion in Colloid and Interface Science, Elsevier, 2001, Vol. 6, pp. 34-39.

[17] J. Lee et al., "Electrowetting and Electrowetting-on-dielectric for Microscale Liquid Handling", Sensors and Actuators A 95, Elsevier, 2002, pp. 259-268.

[18] B. Berge, "Electrocapillarity and Wetting of Insulator Films by Water", Comptes Rendus de l'Academie des Sciences Serie II, 1993.

[19] Paik, P., Pamula, V. K., Chakrabarty, K., "Droplet-based Hot Spot Cooling using Topless Digital Microfluidics on a Printed Circuit Board", THERMINIC 2005, pp.278-283.

[20] H. Oprins et al., "On-Chip Liquid Cooling with Integrated Pump Technology", 21st IEEE SEMI-THERM Symposium, 2007.

[21] Baird, E., Mohseni, K., "Digitized Heat Transfer: A New Paradigm for Thermal Management of Compact Micro Systems", IEEE Transactions on Components, and Packaging Technologies, Vol. 31, No. 1, March 2008, pp.143-151.

[22] Nanayakkara et al., "The Effect of AC Frequency on the Electrowetting Behavior of Ionic Liquids", Analytical Chemistry, 2010, 82, pp.3146-3154.

[23] Bindiganavale, G. S.,"Electrowetting on Dielectric (EWOD) Digital Microfluidics for Electronic Hotspot Cooling", ProQuest, 2010.

[24] "TLC products for use and testing in research applications", LCR Hallcrest Research and Testing Products,

http://www.hallcrest.com/downloads/RT001%20R&T%20Prods%20Info%20Package.pdf.

[25] H. Oprins et al., "Convection Heat Transfer in Electrostatic Actuated Liquid Droplets for Electronics Cooling", Microelectronics Journal, 39, 2008, pp.966-974.

[26] Nanayakkara et al., "A Fundamental Study on Electrowetting by Traditional and Multifunctional Ionic Liquids: Possible Use in Electrowetting on Dielectric-based Microfluidic Applications", Analytical Chemistry, 2008, 80, pp.7690-7698.

[27] Govindraj, B., You, S. M., Moon, H., "Study of Hotspot Cooling using Electrowetting on Dielectric Digital Microfluidic System", MEMS 2014, San Francisco, CA, USA, January 26-30, 2014, pp.1039-1042.

[28] Oprins et al., "Convection Heat Transfer in Electrostatic Actuated Liquid Droplets for Electronics Cooling", Microelectronics Journal, 2008, 39, pp.966-974.

[29] Pearson, J. R. A, "On Convection Cells Induced by Surface Tension", Journal of Fluid Mechanics, 1958, vol. 4, pp.489-500.

[30] Levich, V. G., Physicochemical Hydrodynamics. Englewood Cliffs, N.J : Prentice-Hall, 1962.

[31] Buffone C. et al., "Marangoni Convection in Evaporating Meniscus with Changing Contact Angle", Exp. Fluids, 2014, vol. 55:1833.

[32] Rayleigh, L., "On The Instability of Jets," Proceedings of the London Mathematical Society, vol. s1-10, 1878, pp.4-13.

[33] Eggers, J., "Nonlinear Dynamics and Breakup of Free-Surface Flows", Reviews of Modern Physics, vol. 69, no. 3, 1997, pp.865-929.

[34] Ahmadi et al., "Microdroplet Evaporation in Closed Digital Microfluidic Biochips", Journal of Micromechanics and Microengineering, vol. 23, 2013, 045001 (8pp.).

[35] Lee, J., Kim, J., Kiger, K.T., "Time- and Space-resolved Heat Transfer Characteristics of Single Droplet Cooling using Microscale Heater Arrays.", International Journal of Heat and Fluid Flow, vol. 22, 2001, pp.188-200.

BIOGRAPHICAL INFORMATION

Govindraj Shreyas Bindiganavale earned his Bachelor's degree from Osmania University, Hyderabad, India in 2007, his Master's degree from The University of Texas, Arlington (UTA) in 2009 and a Doctoral degree from UTA in 2015, all in Mechanical Engineering. His research interests lie primarily in innovative techniques to meet Integrated Circuit (IC) hotspot cooling for the next generation 3D ICs in portable electronics. His mixed bag of skills sets include heat transfer, microfluidics, MEMS fabrication, CAD/CAM/CAE, laboratory based experimentation and delivering effective presentations in conferences. He has also published many papers in reputed journals and conferences alike.

Shreyas plans to continue his profession as an electronics thermal management researcher in an industrial R&D setting.